

NORTHWESTERN UNIVERSITY

Fabrication and Optical Properties of Three-Dimensional
Zinc Oxide Photonic Crystals

A DISSERTATION

SUBMITTED TO THE GRADUATE SCHOOL
IN PARTIAL FULFILLMENT OF THE REQUIREMENTS

for the degree

DOCTOR OF PHILOSOPHY

Field of Materials Science and Engineering

By

Michael Scharrer

EVANSTON, ILLINOIS

June 2007

© Copyright by Michael Scharrer 2007
All Rights Reserved

ABSTRACT

Fabrication and Optical Properties of Three-Dimensional Zinc Oxide Photonic Crystals

Michael Scharrer

Over the past two decades photonic crystals (PhCs) have emerged as a promising new class of materials which offers unprecedented control of light in materials. Recently, atomic layer deposition (ALD) has been shown to be a powerful tool for the infiltration of 3D templates with dielectric or semiconducting materials, which has opened new possibilities for PhC fabrication. Here we report on the development and optical characterization of optically active ZnO PhCs for the ultraviolet (UV) to visible spectrum. We have fabricated ZnO inverse opal structures by infiltrating polystyrene opal templates using a low-temperature ALD process. The resulting structures have high filling fractions, possess photonic band gaps in the near-UV to visible spectrum, and exhibit efficient photoluminescence.

We demonstrate room temperature UV lasing in the ZnO photonic crystals, which can simultaneously confine light and provide optical gain. For small lattice constants, we observe random lasing due to disorder in the structures when the photonic pseudogaps are located away from the ZnO gain spectrum. Tuning the primary photonic band gap to the ZnO gain peak leads to a five-fold reduction in lasing threshold due to the enhanced confinement of light. In contrast, highly directional photonic crystal lasing with tunable wavelength is achieved in bands with

abnormally low group velocity in the high-order band structure. This demonstrates that the high-order band structure of three-dimensional photonic crystals can be used to effectively confine light and enhance emission.

Finally we have measured angle- and polarization-resolved reflection and emission properties of ZnO inverse opals. The reflection spectra are explained in terms of multiple Bragg diffraction and the resulting coupling of modes, and the polarization-dependence of reflection features is discussed. We also observe strongly modified spontaneous emission from the PhCs, with suppression due to the primary PBG and strong angular and spectral redistribution of emission in the higher-order band structure. This suggests that in high-quality 3D PhCs significant changes in the radiation pattern can be achieved, which offers possible applications for the tailoring of highly efficient light sources.

To Carrie und Luka

Acknowledgements

The work presented here would not have been possible without the help of many talented and supportive people I have had the pleasure to meet here at Northwestern University. First and foremost, I want to thank my advisor, Prof. R. P. H. Chang, for the intellectual guidance, strong support, and trust he offered throughout my time here. I have learned a great deal from him, not just about science.

I thank all members of Prof. Chang's group over the years who have helped make my time here both enjoyable and productive. I am especially grateful to Bruce Buchholz, Quanchang Li, Eric Seelig, Larry Aagesen, and Anne Muller for the many times they have helped me out.

Special thanks go to Prof. Hui Cao for her enthusiasm and support and the use of her facilities, and to the members of her team, from whom I have learned more about physics than I thought I could and without whose contributions this research would not have been possible – Alexey Yamilov, Xiaohua Wu, and Heeso Noh, in particular.

I thank my parents, my family, and my friends, here and elsewhere, for helping me get this far, offering their support whenever needed, and cheering me up when necessary. Most of all, I am deeply grateful to (and for) my wonderful wife, Carrie, and our awesome daughter, Luka. Thanks for all your love and support, and for your patience through years of graduate school.

Table of Contents

| | |
|---|-----------|
| Abstract | 3 |
| Acknowledgements | 4 |
| List of Figures | 9 |
| List of Tables | 13 |
| 1. Introduction | 14 |
| 2. Photonic Crystals | 19 |
| 2.1 Introduction | 19 |
| 2.2 Diffraction in Photonic Crystals | 20 |
| 2.2.1 Bragg Diffraction | 20 |
| 2.2.2 Diffraction in Periodic Dielectric Media | 23 |
| 2.3 Band Structure of Photonic Crystals | 24 |
| 2.3.1 Maxwell's Equations in Photonic Crystals | 24 |
| 2.3.2 Numeric Methods for Solving the Electromagnetic Wave Equation | 27 |
| 2.4 Dispersion and Refraction in Photonic Crystals | 29 |
| 2.4.1 Band Structure Diagram and Dispersion Surface | 29 |
| 2.5 Emission from Photonic Crystals | 35 |
| 2.5.1 Density of States and Spontaneous Emission | 35 |
| 2.5.2 Localization of Light and Lasing | 37 |
| 2.6 Fabrication of Three-Dimensional Photonic Crystals | 40 |
| 2.6.1 Fabrication Methods | 40 |
| 2.6.2 Fabrication of 3-D Photonic Crystals Based on Colloidal Self-Assembly | 44 |
| 2.6.2.1 Fabrication of Artificial Opals | 44 |
| 2.6.2.2 Infiltration of Opal Templates and Materials Selection | 45 |
| 3. Fabrication of ZnO Inverse Opals by Atomic Layer Deposition | 48 |
| 3.1 Introduction | 48 |
| 3.2 Previous Research on ZnO Photonic Crystals | 49 |
| 3.3 Atomic Layer Deposition of ZnO | 51 |
| 3.3.1 Principles of Atomic Layer Deposition | 51 |
| 3.3.2 Advantages of ALD for Photonic Crystal Infiltration | 53 |
| 3.3.3 ALD Growth Mechanism of ZnO | 55 |
| 3.4 Experimental Methods | 58 |
| 3.4.1 Fabrication of Polystyrene Opal Templates | 58 |
| 3.4.1.1 The Vertical Self-Assembly Method | 58 |
| 3.4.1.2 Choice of Opal Template Material | 62 |
| 3.4.2 ALD Apparatus and Growth Conditions for Opal Infiltration | 65 |
| 3.4.2.1 ALD Reactor | 65 |
| 3.4.2.2 Optimization of ALD Parameters | 67 |

| | | |
|-----------|--|------------|
| 3.4.3 | Inversion of PS Template..... | 68 |
| 3.4.4 | Structural Characterization of ZnO Inverse Opals..... | 70 |
| 3.4.5 | Optical Characterization of ZnO PhCs | 71 |
| 3.5 | Results of ALD Infiltration Studies | 72 |
| 4. | UV Lasing with Reduced Threshold near the First ΓL-Pseudogap..... | 78 |
| 4.1 | Introduction..... | 78 |
| 4.2 | Lasing in Disordered Photonic Crystals | 80 |
| 4.3 | Experimental Procedures | 81 |
| 4.3.1 | Reflection, Transmission and the Photonic Band Structure | 81 |
| 4.3.2 | Emission Measurements | 82 |
| 4.4 | Results and Discussion | 83 |
| 4.5 | Summary | 91 |
| 5. | Lasing in High-Order Bands of 3D ZnO Photonic Crystals..... | 92 |
| 5.1 | Introduction..... | 92 |
| 5.2 | Experimental Procedures | 94 |
| 5.3 | Optical Properties in the High-Order Band Structure..... | 95 |
| 5.3.1 | Reflection Spectroscopy | 95 |
| 5.3.2 | Results of Emission Measurements | 97 |
| 5.3.3 | Comparison to Band Structure Calculations..... | 100 |
| 5.3.4 | Lasing Mode Imaging..... | 103 |
| 5.4 | Conclusion | 105 |
| 6. | Angle- and Polarization-Dependent Reflection and Spontaneous Emission Properties..... | 106 |
| 6.1 | Introduction..... | 106 |
| 6.2 | Emission Modification in Photonic Crystals | 107 |
| 6.3 | Experimental Procedures | 108 |
| 6.3.1 | ZnO PhCs Samples | 108 |
| 6.3.2 | Optical Measurements | 110 |
| 6.3.3 | Band Structure Calculations | 112 |
| 6.4 | Results..... | 115 |
| 6.4.1 | Reflection Data | 115 |
| 6.4.2 | Photoluminescence Measurements | 116 |
| 6.5 | Discussion..... | 117 |
| 6.6 | Conclusions..... | 124 |
| 7. | Conclusions and Future Studies | 125 |
| 8. | References | 126 |

List of Figures

| | |
|---|----|
| Figure 2.1: (a) Constructive interference of a wave scattered by a family of planes with lattice spacing d occurs at angle θ when the difference of path lengths $2d \cos \theta$ of successive reflections is equal to an integer number of wavelengths λ . (b) Dispersion relation for a wave propagating normal to the lattice planes in (a). At $k = \pi/d$ the Bragg condition is fulfilled and a stop gap forms. | 21 |
| Figure 2.2: (a) 2-D square lattice and (b) the corresponding schematic band structure. Band X corresponds to wave vectors k' being folded back into the first BZ by subtracting G_2 , i.e. by diffraction from (01) planes. | 22 |
| Figure 2.3: (a) First Brillouin zone of a FCC lattice, with high symmetry points labeled. (b) Band structure of a fcc PhC of close-packed polystyrene spheres..... | 30 |
| Figure 2.4: Refraction of light in a 2D PhC. For clarity, only the transmitted beams are shown. The dispersion in air and the incident wave vector are shown on top. The dashed green line shows the condition of conservation of k_{\parallel} . (a) At a frequency below the PBG, the dispersion surface is only slightly deformed, k_t and v_g are almost collinear. (b) In this case a stop band has opened at the M point. Waves propagating with k_{i1} cannot propagate in the periodic structure. For waves with k_{i2} , the direction of energy flux is different from the transmitted wave vector k_{t2} | 33 |
| Figure 2.5: (a) Calculated dispersion surface of an inverse opal PhC with $n=3$. for a frequency just above the primary ΓL gap. Only bands 1 and 3 are shown. (b) Dispersion surface just above the complete PBG of a Si inverse opal. The only allowed modes are located in ellipsoid lobes close to the X point. [16] | 34 |
| Figure 2.6: Random lasing by feedback loops in a disordered medium. | 37 |
| Figure 2.7: (a) Cavity design and electric field distribution for a 2-D microcavity laser. (b) SEM image of fabricated cavity. [21] | 38 |
| Figure 2.8: Silicon yablonovite fabricated by FIB drilling. [24] | 41 |
| Figure 2.9: Si woodpile structure. [26] | 42 |
| Figure 2.10: 3-D PhC fabricated by direct writing. [29]..... | 43 |
| Figure 2.11: (a) Beam diagram for 3D holographic lithography using a coupling prism. (b) Example of FCC structure fabricated in photoresist. [32] | 43 |
| Figure 2.12: Example of thin film opal of silica spheres..... | 45 |
| Figure 2.13: Schematic of opal infiltration and inversion process. | 46 |
| Figure 3.1: ZnO opal fabricated by self-assembly by of monodispersed ZnO particles. | 50 |
| Figure 3.2: TEM images of $Hf_xAl_yO_2$ composite structure. Right image is detail of bottom corner. [87]..... | 53 |

- Figure 3.3: (a) The narrowest channel for precursor diffusion into the opal structure is defined by 3 close-packed spheres in the (111) surface. (b) Illustration of pore geometry determining the maximum film thickness..... 54
- Figure 3.4: Typical pulse sequence for one ALD reaction cycle..... 56
- Figure 3.5: ALD growth of ZnO from $\text{Zn}(\text{C}_2\text{H}_5)_2$ and H_2O 57
- Figure 3.6: Vertical convective self-assembly method: A flat substrate is placed into the colloidal suspension and the solvent is evaporated, causing the particles to self-assemble in the meniscus. 60
- Figure 3.7: Photographs of PS opal sample ($d=256\text{nm}$) under two different illumination conditions, showing transmitted (left) and reflected (right) color. The sample size is $\sim 10 \times 12\text{mm}$ 61
- Figure 3.8: Cross-sectional scanning electron micrograph of ZnO inverse opal fabricated by infiltration of a template of plain polystyrene spheres. The image shows the corner of a crystal domain of the inverse opal, with a ZnO film grown conformally around each sphere and inside the structure. 62
- Figure 3.9: (a) ZnO inverse opal, fabricated using a plain PS template, $d=250\text{nm}$. (b) ZnO inverse opal based on CM-PS, $d=256\text{nm}$. Both structures were fired in air at 450°C for 3 hours. The plain PS results in low-density films and low filling fraction..... 64
- Figure 3.10: Schematic view of the ALD apparatus showing the direction of gas flow (indicated by arrows) during a water exposure. 66
- Figure 3.11: Cross-section of fired ZnO opal, $d=170\text{nm}$, at (a) low and (b) higher magnification. Insufficient pulse time led to incomplete infiltration. 69
- Figure 3.12: ZnO inverse opal with $d=256\text{nm}$ and a thickness >100 layers. 72
- Figure 3.13: (111) planes of ZnO PhCs exposed by RIE, (a) $d=256\text{nm}$ (b) $d=362\text{nm}$. The yellow square marks exposed interstitial pore. 74
- Figure 3.14: XRD scan for $d=256\text{nm}$ ZnO inv. opal fired at 550°C in air for 30min. The calculated background (yellow) and fitted peak profiles (red) are shown. 75
- Figure 3.15: Transmission spectra of ZnO PhCs measured in the [111] direction. As the band gap shifts towards the absorption edge with decreasing sphere size, the band gap position becomes obscured. (The relatively low transmission of the 356 nm sample outside the band gap is due to its larger thickness.) Insert: Reflection peaks of the 170 nm and 202 nm structures at normal light incidence clearly show the existence of stop bands in the (111) direction near the absorption edge. 76
- Figure 3.16: PL spectrum of ZnO inverse opal. This sample has no band gaps overlapping the emission spectrum. 77
- Figure 4.1: SEM image of exposed (111) surface of a ZnO inverse opal with $d=171\text{nm}$ 81

- Figure 4.2: Schematic of the optical set-up used to measure lasing and photoluminescence from the ZnO inverse opal structures. The white light and pump beam are incident normal to the sample surface along the [111] direction, and the emission is collected in the same direction. BS stands for UV beam splitters, L1 is a 20X UV objective lens, M is a flip mirror to select the pump beams..... 83
- Figure 4.3: (a) Calculated photonic band structures of the ZnO inverse opals in the vicinity of the first Γ L pseudogap. The dashed line marks the approximate position of the ZnO absorption edge. With decreasing sphere size the fundamental PBG shifts closer to the absorption edge and the 160nm sample has no PBG due to absorption. (b) Specular reflection spectra of ZnO inverse opal PhCs with varying sphere diameters. 85
- Figure 4.4: Photoluminescence and lasing spectra of the ZnO inverse opals with varying sphere diameters. The random lasing modes in the $d=160\text{nm}$, 202nm and 256nm samples overlap with the peak in PL spectrum. In the $d=171\text{nm}$ sample the PL is suppressed and blue-shifted by the PPBG (indicated by the reflection spectrum, dashed line). The main lasing modes are red-shifted into the PBG and do not overlap with the PL maximum. 86
- Figure 4.5: Lasing threshold versus sphere diameter for the ZnO inverse opals. The lasing threshold is strongly reduced when the PBG overlaps the emission spectrum of ZnO. 88
- Figure 4.6: Lasing spectra for increasing pump intensities (in MW/mm^2) for $d=171\text{nm}$ and $d=202\text{nm}$ samples. (Inset: L-L curve for $d=171\text{nm}$). Inset: L-L curve for the 171nm spectra. 90
- Figure 5.1: Schematic of the modified optical set-up used to obtain mode images. 94
- Figure 5.2: Reflection spectra of ZnO PhCs for four different sphere diameters. Light is incident along the [111] direction normal to the PhC surface. The first-order Bragg peak (peak R1) and two main reflection peaks at shorter wavelengths (R2 and R3) are detected. 96
- Figure 5.3: Position of the reflection peaks versus sphere diameter d . As the wavelength approaches the absorption edge of ZnO (at $\lambda \approx 380\text{ nm}$), the refractive index increases sharply and slows down the blue-shift of the peaks..... 96
- Figure 5.4: Lasing peaks (L) plotted along with reflection spectra (same as Figure 5.2). Lasing occurs at the high-frequency shoulder of the third main reflection peak (R3) in all samples. 97
- Figure 5.5: (a) Emission spectra of ZnO PhCs with $d = 330\text{nm}$ and 362nm for increasing pump intensity. Inset: L-L curve for the 362nm sample (with a clear threshold at $\sim 5.9\text{ MW}/\text{mm}^2$). (b) Angular distribution of lasing emission. (Squares represent measured data, the line is a guide for the eye.) (c) Lasing threshold and wavelength versus sphere diameter. 99

- Figure 5.6: (a) Reflection (black), photoluminescence (blue) and lasing (violet) spectra of a PhC with $d=362$ nm. Lasing occurs at the high-frequency shoulder of the reflection peak at 407 nm. The photoluminescence exhibits a minimum in this region, confirming the existence of a stop band. (b) Calculated band structure of ZnO inverse opals with $d=355$ nm in the Γ -L direction. The lasing peak coincides with the isolated flat band (red) at the high-frequency edge of the third gap. The shaded yellow areas indicate the calculated band gaps. (c) Calculated group velocities. Light in the weakly dispersive band (red) has a very low v_g over the whole Γ -L range..... 102
- Figure 5.7: Mode Imaging. (a) White-light image of the ZnO inverse opal cross-section (cleaved edge). Scale bar represents 10 μm . The circle indicates the approximate size and position of the pump spot. (b) Lasing mode image (inverted contrast) and the corresponding lasing spectrum (inset, x-axis shows wavelength, y-axis shows emission intensity in a.u.). 104
- Figure 6.1: Specular reflection of $d=400$ nm ZnO inv. opal along $[111]$ direction..... 109
- Figure 6.2: (a) Optical set-up for θ - 2θ reflection scans. (b) Set-up for PL measurements..... 110
- Figure 6.3: (a) Orientation of the samples during optical measurements. The growth direction is indicated by the black arrow. N (red) is the surface normal. The samples were aligned using the diffraction pattern on the surface. (b) The FCC BZ showing the Γ -L-U-X diffraction plane. 112
- Figure 6.4: Band structure of a ZnO inverse opal with $d=400$ nm, calculated for $n(\omega)$. S-polarized bands are shown in red, p-polarized bands in blue. Polarization states were obtained from coupling coefficients calculated by the layer KKR method. 114
- Figure 6.5: Reflection spectra from $\theta=5^\circ$ to 55° for p - and s -polarization..... 115
- Figure 6.6: PL spectra for a random reference sample and a $d=400$ nm inv. opal. Spectra are normalized to overlap at $\lambda=880$ nm. 117
- Figure 6.7: Emission ratio spectra, normalized by the respective reference spectra. 118
- Figure 6.8: Reduced band structures, reflectance, and emission ratios for s - (blue) and p -polarization, for angles of (a) $\theta=20^\circ$, (b) $\theta=30^\circ$, and (c) $\theta=40^\circ$ 119
- Figure 6.9: Section of the dispersion surface in the Γ -L-U-X plane at reduced frequency $a/\lambda=0.85$. The red circle gives the dispersion in air; the black dotted lines represent the bands inside the PhC. (a) Dispersion diagram for incident k vector at $\theta=20^\circ$. (b) At larger angle ($\theta=40^\circ$) bands are almost perpendicular to the BZ. The detection cone is shown in green; the range of k -vectors is shaded red..... 121
- Figure 6.10: Comparison of (a) PL emission ratio, (b) measured, and (c) calculated reflectance versus angle θ , plotted as gray scale maps. The experimental reflection data are in good agreement with the results of the KKR calculations. The PWE band structures are overlaid in red..... 123

List of Tables

| | |
|---|----|
| Table 3.1: Typical operating parameters for ALD infiltration of polystyrene opals. | 68 |
|---|----|

1. Introduction

Over the past century, science and technology have been revolutionized by the discovery of quantum physics and the ensuing development of electronic technology, which relies on the electronic band gap in semiconductors to manipulate the flow of electrons. The past two decades have seen rapid progress in the development of a new class of materials, known as photonic crystals (PhCs) [1, 2], which offer unprecedented control over light and have the potential to bring about a similar revolution in photonics, i.e. the technology of photons. PhCs are materials with a periodic modulation of the dielectric constant in 1, 2, or 3 dimensions, on a scale of the wavelengths of electromagnetic (EM) radiation. This modulation leads to a modification of the dispersion characteristics from the normal $\omega = (c/n)\mathbf{k}$ relation and the formation of a photonic band structure. Frequency ranges can exist where the propagation of EM waves is prohibited, i.e. photonic band gaps (PBGs), and or where light propagates with strongly reduced group velocity. The band structure leads to a variety of interesting phenomena, such as suppression and modification of spontaneous emission, anomalous refraction, and low-threshold lasing due to confinement of light. It further opens up the possibility of “band structure engineering” using designed defects and heterostructures, in analogy to the electronic technology.

PBG technology can be applied in a large variety of new photonic devices, with potential applications in many areas such as sensors, light emitters, optical and quantum computing. One-dimensional (1D) PhCs have been known for well over a century (e.g. in the form of Bragg

reflectors), and the technology of 2D PhCs, e.g. thin films with patterned arrays of holes, has seen great advances toward application as waveguides or microcavities, profiting from the fabrication methods developed for the semiconductor technology. Photonic crystal fibers (PCFs) [3], which represent a special case of 2D PhCs, have already found commercial applications.

However, while the physical concepts are well known, many predictions remain untested and many problems unsolved. This is especially the case for 3D PhCs, which offer both the most interesting physics and the greatest challenges in fabrication and materials science [4]. Early realizations of 3D PBG structures were working in the microwave spectrum [5]. Since the required periodicity of the dielectric function scales with the EM wavelengths which are targeted, applications in the visible to UV range call for photonic crystals with lattice constants in the submicron range, and the minimum feature sizes are often below the resolution limits of standard microfabrication techniques. While steady progress is being made in developing new methods for 3D patterning, self-assembly of monodispersed colloidal spheres into so-called “artificial opals” has been the most common approach for the fabrication of 3-D PhCs and is suitable for creating UV band gap materials [6]. The flexibility of this method can be increased by infiltrating the opal templates with higher-index dielectric materials. The work described in the following demonstrates the potential of combining self-assembly with atomic layer deposition (ALD) for the fabrication of high-quality 3-D PhCs. ALD is a modified CVD growth method which allows highly conformal film growth, making it an ideal tool for the infiltration of complex 3D templates. Removal of the sphere template after infiltration leaves an “inverse opal” structure of the desired dielectric material.

Much of the PhC research so far has concentrated on achieving the high dielectric contrast needed for a complete (i.e. omnidirectional) PBG, using passive dielectric materials such as Si or TiO₂. Interesting optoelectronic materials remain untested for PhC applications, many of which do not rely on a complete gap but rather on the modified dispersion relation in the vicinity of directional gaps. The research described in this thesis concentrated on PhCs made from ZnO. ZnO is a semiconductor with a wide ($\sim 3.2\text{eV}$) and direct electronic band gap and a high exciton binding energy ($\sim 60\text{meV}$) and has been the focus of intense research due to its potential for optoelectronic applications, especially for UV emission [7]. Ultraviolet (UV) lasers and light emitting diodes (LEDs) are of great interest for many applications, such as high-density optical storage, high-resolution laser printing, solid-state lighting, or display technology. PhCs can be used to increase the efficiency of LEDs by modifying or redistributing spontaneous emission and can reduce the lasing threshold by confining light in the gain material. Thus the research described herein was aimed at developing optically active ZnO PhCs and studying their emission and lasing properties.

The effect of the primary PBG on the lasing threshold was studied and a reduction of lasing threshold was demonstrated by carefully tuning the band structure of the inverse opals to the gain spectrum of ZnO. It was also shown that the high-order band structure could be utilized to achieve directional photonic crystal lasing due to the “group velocity anomaly” in weakly dispersive bands.

The physics of photon propagation and emission in the high-energy band structure of 3D PhCs have only begun to be studied because most research has focused on the primary PBG, and the demonstration of PhC lasing motivated a study of the angle- and polarization-resolved

emission properties to further understand the physical processes involved. In PhCs with strong refractive index contrast, multiple diffraction at high frequencies or angles leads to a complex coupling of many Bloch waves. This can cause singularities in the photonic density of states (DOS) and modification the directionality and polarization of spontaneous emission. This effect is demonstrated in the ZnO inverse opals, where the broad photoluminescence peak from electronic defect states in ZnO makes it possible to follow the dispersion of band structure features over a wide frequency range.

This thesis is outlined as follows:

- Chapter 2 serves to establish the theoretical framework for a description of light propagation in PhCs. Basic physical concepts such as Bragg diffraction, band structure, and the dispersion surface are discussed in the context of PhCs, and the numerical methods used to calculate optical properties of PhCs by solving Maxwell's equations are described briefly. Also, general fabrication and materials issues relating to 3-D PhCs are reviewed.
- Chapter 3 discusses the fabrication of ZnO inverse opals. Self-assembly of the polystyrene opal templates and the development of a low-temperature ALD process for infiltration are described. Results of basic optical measurements (reflection and transmission spectroscopy) are shown establishing the photonic nature of the ZnO structures.
- Chapter 4 briefly reviews possible lasing mechanisms in disordered structures (random lasing) and in ordered PhC structures, and presents the results of lasing experiments in the vicinity of the first-order stop gap of the inverse opals. Tuning the PBG to the

emission spectrum of ZnO (by changing the sphere diameters of the templates) leads to a significant reduction of lasing thresholds and a shift of the lasing frequency into the PBG. Considering the degree of disorder in the samples and the directionality of emission we propose a mechanism of PBG-enhanced random lasing for the observed effect.

- In Chapter 5 photonic crystal lasing in high-order bands of the ZnO PhCs is demonstrated. The lasing mechanism is based on the so-called “group velocity anomaly” of weakly dispersive high-energy bands, which leads to low-threshold lasing of slowly propagating EM modes. The detrimental influence of disorder is reduced due to the larger periodicity allowed by using the high-order band structure.
- Chapter 6 describes the results of angle- and polarization-resolved measurements of reflection, transmission, and spontaneous emission. Multiple Bragg diffraction in higher photonic bands is shown to modify the directional photonic density of states and cause significant angular and spectral redistribution of spontaneous emission.

2. Photonic Crystals

2.1 Introduction

Although the PBG effect in 1D periodic dielectric structures has been known since the 19th century and has been widely used in the form of Bragg reflectors, it wasn't until 1987 that this concept was expanded to two and three dimensions, when Eli Yablonovich first suggested the possibility of suppression of spontaneous emission in photonic band gaps of 3-D periodic dielectric materials [8]. At the same time Sajeev John proposed the "Strong Localization of Photons in Certain Disordered Dielectric Superlattices" [9], suggesting that such materials could be used to confine light. The combination of well-known concepts developed in solid state physics for describing electronic properties of materials and diffraction of X-rays by atomic crystals with Maxwell's equations governing the propagation of EM waves has led to tremendous progress in the field and an exponential growth in the number of publications on PhCs and PBG effects. Beside the originally envisioned applications based on quantum electrodynamics, active areas research now include optically active and tunable PhCs, nonlinear and magneto-optic effects, quantum information and computing, and more. It has to be conceded, however, that the realization of many predicted effects is hampered by the fabrication and materials challenges involved. At the same time, due to the vector nature of photons numerical calculations are far more complex than in the electronic case, which often makes it

difficult to predict the properties of real systems. As a consequence, there is a strong need for experimental studies to both test and improve the predictions of the theoretical models.

2.2 Diffraction in Photonic Crystals

2.2.1 Bragg Diffraction

Bragg diffraction describes the effects of interference of waves propagating through a periodic material and is the underlying process determining the behavior of light waves in photonic crystals. Bragg diffraction was first used to study the scattering of X-rays in atomic crystals and later for optical waves in 1D layered dielectrics. The Bragg equation gives the conditions for constructive interference of waves (Figure 2.1a):

$$m \lambda = 2d n \cos \theta \quad (2.1)$$

Constructive interference occurs when the path difference of two waves reflected from successive layers of the crystal lattice is equal to an integer multiple m of the wavelength. (The wavelength- and angle-dependence described by Bragg's law is the basis of many structural color effects in nature, such as in butterfly wings or peacock feathers [10], and the "opalescence" effect in the visual appearance of photonic crystals known from gemstone opals.) When the structure is sufficiently thick and ordered, the Bragg reflections of many successive layers overlap and give rise to a directional gap (also called a stop gap or pseudogap), i.e. the

diffraction efficiency reaches 100% and light cannot propagate in the specific direction of the crystal. This is seen e.g. in the X-ray diffraction peaks from an atomic crystal.

Figure 2.1b shows the (1D) dispersion relation between the photon wave vector k and frequency ω for a wave propagating normal to the lattice planes. The Bragg condition is fulfilled when $k=\pi/d$, and a gap in the dispersion curve forms. In other words, diffraction occurs at the edge of the Brillouin zone (BZ), and bands are folded back into the first BZ by the diffracting lattice vectors (reduced band scheme).

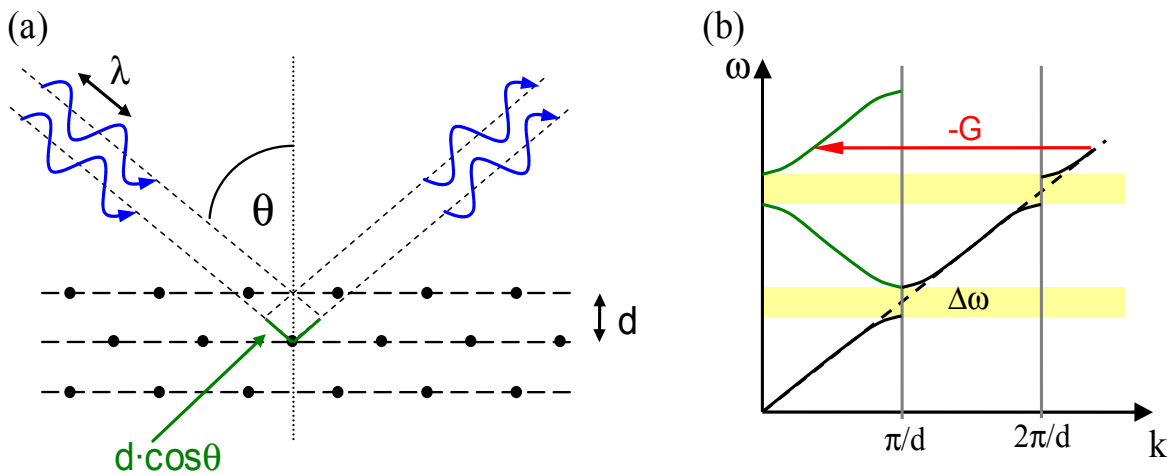


Figure 2.1: (a) Constructive interference of a wave scattered by a family of planes with lattice spacing d occurs at angle θ when the difference of path lengths $2d \cos \theta$ of successive reflections is equal to an integer number of wavelengths λ . (b) Dispersion relation for a wave propagating normal to the lattice planes in (a). At $k = \pi/d$ the Bragg condition is fulfilled and a stop gap forms.

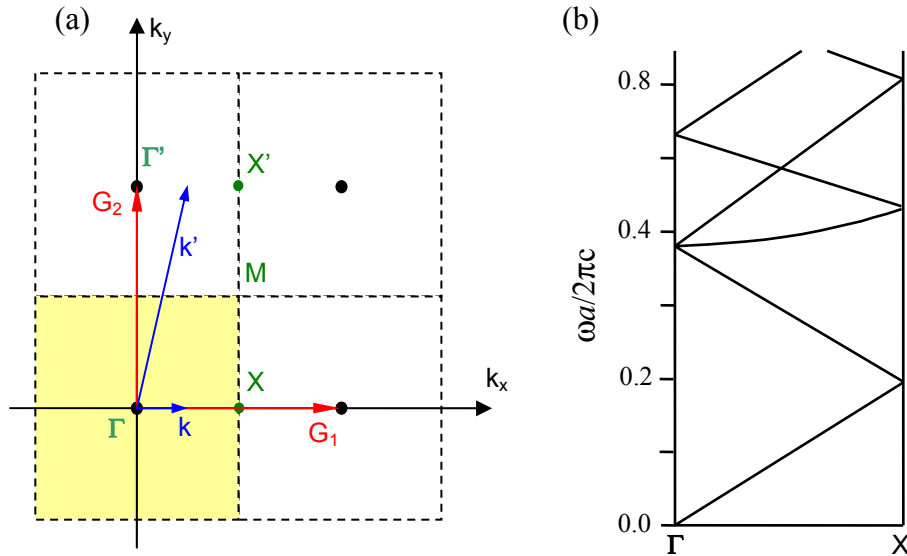


Figure 2.2: (a) 2-D square lattice and (b) the corresponding schematic band structure. Band X corresponds to wave vectors \mathbf{k}' being folded back into the first BZ by subtracting \mathbf{G}_2 , i.e. by diffraction from (01) planes.

In 2D or 3D lattices at higher frequencies, bands corresponding to wave vectors which are originally outside the first BZ can be folded back into the BZ by lattice vectors not parallel to the given lattice direction. This situation is depicted in Figure 2.2 for a 2D square lattice. The third band in the ΓX direction corresponds to wave vectors \mathbf{k}' outside the first BZ which are folded back by the lattice vector \mathbf{G}_2 not parallel to ΓX . These bands are described by the dispersion equation

$$\omega = ck' = c \left[\left(\frac{2\pi}{a} \right)^2 + k^2 \right]^{1/2} \quad (2.2).$$

This means they are less dispersive and light propagates with reduced group velocity $v_g = \delta\omega/\delta k$ in these bands. They are sometimes referred to as “flat bands” or “heavy photon bands”, in analogy to heavy electron bands in electronic band structures. The modified dispersion behavior of photons in these bands can have a dramatic impact on the optical properties of PhCs, as will be discussed in Chapters 5 and 6.

2.2.2 Diffraction in Periodic Dielectric Media

In a 1D PhC, i.e. a simple multilayer dielectric film, the dispersion of light is given by $\omega=(c/n)k$, and now the Bragg condition can be approximated as

$$m \lambda = 2d n_{\text{eff}} \cos \theta \quad (2.3)$$

where the effective refractive index n_{eff} can be estimated as $n_{\text{eff}}=f_1 n_1 + f_2 n_2$ (with f_1 and f_2 being the respective filling fractions of the two dielectric materials) as long as the index contrast is small. The approximate center frequency ω_c of the PBG will be determined by the average refractive index, while the width of the gap $\Delta\omega$ is determined by the index contrast. The ratio $\Delta\omega/\omega_c$ gives a measure of the photonic strength of the system.

Compared to X-ray diffraction, the interaction of optical waves with matter is a factor of $\sim 10^5$ stronger, which leads to much stronger scattering and wider gaps in photonic crystals. In 3D PhCs this opens up the possibility of a complete PBG: The stop gaps for different directions in the crystal can overlap and result in a range of frequencies where photons cannot propagate in

any direction. Because the gaps open up at the edges of the BZ with a corresponding frequency $c\mathbf{k}/n$, the optimal PhC structure will have a BZ which is as close to spherical as possible, suggesting a face centered cubic (FCC) lattice. (In the diamond lattice, which has a fcc lattice with a basis of two “atoms,” symmetry restrictions lift band degeneracies at the BZ edge to increase the gap. However, diamond structures are far more difficult to fabricate.) Since $\Delta\omega/\omega_c \sim \Delta n/n_{\text{eff}}$, it also becomes apparent that to maximize the photonic strength of a PhC we need to achieve a high dielectric contrast along with a low filling fraction of the high index material.

2.3 Band Structure of Photonic Crystals

2.3.1 Maxwell’s Equations in Photonic Crystals

While Bragg diffraction serves as a conceptual framework for understanding the behavior of light in PhCs, the previous discussion assumes that the refractive index contrast does not differ significantly from unity. For strongly photonic structures, an accurate description of the band structure demands that we solve Maxwell’s equation for EM waves propagating in the periodic dielectric structure. For an inhomogeneous dielectric medium without charges or currents we have

$$\nabla \times \mathbf{E}(\mathbf{r}, t) = -\frac{\partial \mathbf{B}(\mathbf{r}, t)}{\partial t}, \quad \nabla \cdot \mathbf{D}(\mathbf{r}, t) = 0, \quad (2.4)$$

$$\nabla \times \mathbf{H}(\mathbf{r}, t) = \frac{\partial \mathbf{D}(\mathbf{r}, t)}{\partial t}, \quad \nabla \cdot \mathbf{B}(\mathbf{r}, t) = 0.$$

In addition, we need the constitutive equations which relate \mathbf{D} to \mathbf{E} and \mathbf{B} to \mathbf{H} :

$$\mathbf{B}(\mathbf{r}, t) = \mu_0 \mathbf{H}(\mathbf{r}, t) \quad \text{and} \quad \mathbf{D}(\mathbf{r}, t) = \epsilon_0 \epsilon(\mathbf{r}) \mathbf{E}(\mathbf{r}, t), \quad (2.5)$$

where we have assumed that the material is non-magnetic and that the dielectric function ϵ is isotropic, periodic with respect to position \mathbf{r} , real, and not a function of frequency ω . (Obviously, the later two assumptions will not be valid in the vicinity of the absorption edge of the ZnO PhCs, and we will have to take into account the effect of absorption and the frequency dispersion of the dielectric function $\epsilon(\mathbf{r}, \omega)$ for band structure calculation). The periodicity of $\epsilon(\mathbf{r})$ allows expansion of $\epsilon^{-1}(\mathbf{r})$ into a Fourier series in reciprocal space:

$$\epsilon^{-1}(\mathbf{r}) = \sum_{\mathbf{G}} \kappa(\mathbf{G}) \exp(i\mathbf{G} \cdot \mathbf{r}) \quad (2.6).$$

Here \mathbf{G} is an arbitrary lattice vector and $\kappa(\mathbf{G})$ are the Fourier coefficients. Assuming a time dependence of the form $\exp(-i\omega t)$ we can obtain the equation:

$$\nabla \times \frac{1}{\epsilon(\mathbf{r})} \nabla \times \mathbf{H}(\mathbf{r}) = \left(\frac{\omega}{c} \right)^2 \mathbf{H}(\mathbf{r}) \quad (2.7)$$

where $c = (\epsilon_0 \mu_0)^{-1/2}$ is the speed of light in vacuum. This is an eigenvalue equation for the eigenfunction $\mathbf{H}(\mathbf{r})$ and it can be shown that the operator “ $\nabla \times 1/\epsilon(\mathbf{r}) \nabla \times$ ” acting on the magnetic field vector is Hermitian. Therefore its eigenvalues $(\omega/c)^2$ are also real and its non-degenerate eigenmodes are orthogonal. (An equation equivalent to (2.7) can also be written for the electric field, of course. However, its operator is not Hermitian, and its treatment therefore less straightforward.)

Equation (2.7) is analogous to Schrödinger’s equation in quantum mechanics, with $1/\epsilon(\mathbf{r})$ acting as the “potential”, and we can use the same linear algebra theorems to solve this EM wave equation. In contrast to the Schrödinger equation the wave equation also produces some unphysical solutions of zero frequency; physical solutions require the fields to be transverse,

$$\nabla \times \mathbf{H}(\mathbf{r}) = 0. \quad (2.8)$$

Most importantly, because ϵ is periodic in \mathbf{r} , Bloch’s theorem applies and we can express the solutions as:

$$\mathbf{H}(\mathbf{r}) = \mathbf{H}_{\mathbf{k},n}(\mathbf{r}) = e^{i\mathbf{k} \cdot \mathbf{r}} \mathbf{u}_{\mathbf{k},n}(\mathbf{r}) \quad (2.9)$$

where \mathbf{k} is in the first BZ and $\mathbf{u}_{\mathbf{k}}(\mathbf{r})$ is an envelope function periodic in the lattice. This representation means that the eigenmodes fold back into the first BZ of the PhC and can be classified by a Bloch wave vector \mathbf{k} and a band number n , i.e. the band structure is given by a succession of pairs of $(\omega, \mathbf{k})_n$ labeled by the band number n . The Bloch modes can also be classified according to their symmetry using group theory, which yields information about their coupling amongst each other and across the crystal surface [2, 11].

Two differences to the case of electrons in solids should be noted, both of which stem from the vector nature of light: The conditions of gap formation are much more restrictive than in the electronic case, and for photons there is no absolute length scale analogous to the Bohr radius. As a consequence of the latter point, the physics of photonic crystals are scalable with the lattice constant (as long as ϵ is constant), and the frequency can be expressed in units of $\omega/(2\pi c/a) = a/\lambda$.

2.3.2 Numeric Methods for Solving the Electromagnetic Wave Equation

The periodicity of the envelope functions (2.9) allows them to be expanded into a Fourier series of the form

$$\mathbf{H}_{\mathbf{k},n}(\mathbf{r}) = \sum_{\mathbf{G}} \mathbf{H}_{\mathbf{k},n}(\mathbf{G}) \exp[i(\mathbf{k} + \mathbf{G}) \cdot \mathbf{r}] \quad (2.10),$$

and substitution of Equations (2.6) and (2.10) into (2.7) yields:

$$-\sum_{\mathbf{G}'} \kappa(\mathbf{G} - \mathbf{G}')(\mathbf{k} + \mathbf{G}) \times [(\mathbf{k} + \mathbf{G}') \times \mathbf{H}_{\mathbf{k},n}(\mathbf{G}')] = \frac{\omega_{\mathbf{k},n}^2}{c^2} \mathbf{H}_{\mathbf{k},n}(\mathbf{G}') \quad (2.11)$$

where $\omega_{\mathbf{k},n}$ denotes the angular eigenfrequency of $\mathbf{H}_{\mathbf{k},n}(\mathbf{r})$. Equation (2.11) expresses an infinite system of homogeneous equations which can be solved numerically by diagonalization of the matrix given in the left hand side for a sufficiently large set N of basis vectors \mathbf{G} . This is called the plane wave expansion method and is commonly used to calculate the band structures of infinite PhCs [12]. However, due to the vectorial nature of the equation the required calculation time is very high and the convergence is poor for high dielectric contrast. For realistic PhC structures the accuracy is often smaller than 10% even for $N > 1000$.

If the PhC is composed of spherical or cylindrical dielectric elements we can use spherical waves instead of plane waves as a basis set for the expansion, which greatly improves the convergence. This approach, referred to as the vector KKR (Korringa-Kohn-Rostoker) method, can also be used to efficiently compute scattering and transfer matrices of finite photonic structures. Matrix-based methods divide the structure into adjacent parallel layers, with the relation between the incoming and outgoing fields of each layer (in real or reciprocal space) given by a matrix. Neighboring layers can be combined by combining their matrices, and this can be repeated until a matrix obtained that relates the fields on both sides of the whole structure. In the KKR-based matrix method [13, 14], scattering from each sphere is calculated using spherical harmonics and the interactions of the waves scattered by each layer are calculated using transfer or scattering matrices. Matrix methods can be used to directly calculate the optical response of arbitrary PhC structures such as reflection and transmission coefficients, which makes them very useful in understanding the (experimentally measured) properties of PhC devices. Furthermore, the spherical expansion method provides information about the coupling of EM modes and their polarization state [11, 15].

2.4 Dispersion and Refraction in Photonic Crystals

2.4.1 Band Structure Diagram and Dispersion Surface

The band structure diagram is one way of representing the complex dispersion behavior of PhC: The eigenfrequencies $\omega_{\mathbf{k},n}$ are plotted versus the corresponding wave vectors for particular directions in the lattice. Figure 2.3b shows the band structure calculated for a polystyrene artificial opal, i.e. a close-packed FCC array of monodispersed colloidal spheres. The corresponding BZ and high symmetry points are shown in Figure 2.3a. Note that panels starting at the Γ point plot the eigenfrequencies for increasing magnitude of \mathbf{k} in the specified direction, e.g. from Γ to the L point for propagation in the close-packed [111] direction of the fcc crystal. In other panels ω is plotted versus the \mathbf{k}_{\parallel} -component as the direction of \mathbf{k} is swept from one high symmetry point to another across the BZ surface. The diagrams show both “nearly free photon” and flat bands as well as the effects of mode coupling and repulsion, such as directional gaps in the Γ -L direction and anti-crossings of symmetry-related bands.

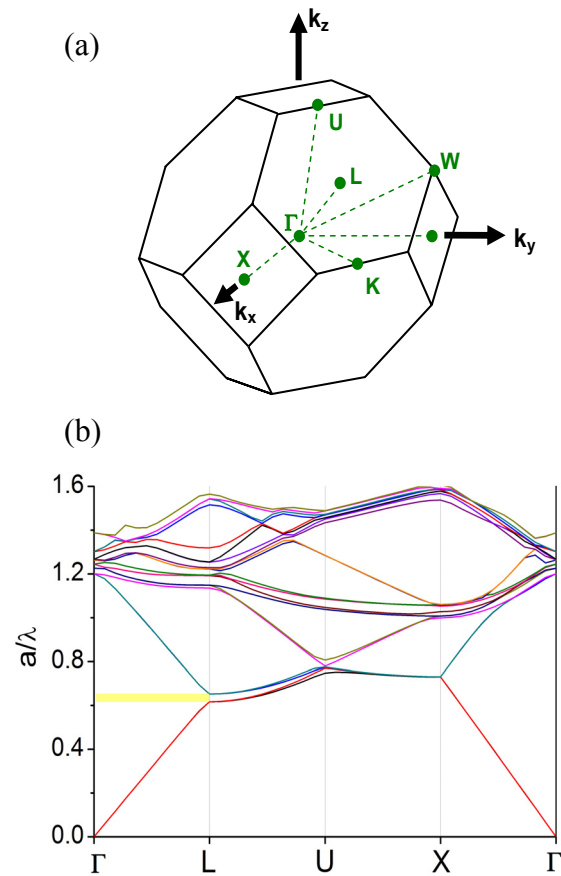


Figure 2.3: (a) First Brillouin zone of a FCC lattice, with high symmetry points labeled. (b) Band structure of a fcc PhC of close-packed polystyrene spheres.

At the BZ boundary, the dispersion curves originating from different lattice points intersect indicating that a Bragg condition is fulfilled. If a modulation of the dielectric constant is introduced, the EM modes mix and this mode mixing leads to a frequency split, i.e. the bands repel each other and a gap opens up. Modes within the BZ resemble plane waves, while the Bloch modes near the gap resemble standing waves. An EM field stores more energy if it has maxima rather than nodes in the high- ϵ regions, the splitting leads to lower “dielectric” bands

(concentrated in the high dielectric) and upper “air” bands (concentrated in the low dielectric regions), roughly equivalent to the valence/conduction bands in a semiconductor. At higher frequencies more and more Bloch modes start to mix and interact and the situation becomes increasingly more complex. In other words, the behavior becomes dominated by multiple diffractions from different lattice planes rather than the simple Bragg diffraction model outlined in section 2.2.

When one is interested in how light couples in and out of a PhC, the band structure diagram does not provide a clear picture. In this context it is often necessary to consider the angular dispersion of the eigenmodes at a given eigenfrequency. It is instructive to consider the particular case of vanishing variation of the dielectric function. It then follows from Equation (2.11) that the eigenfrequencies are given by the free space dispersion law, i.e. the solutions are obtained by a replication of the dispersion law over all points of the reciprocal lattice. This picture is equivalent to the extended zone scheme shown for a 1D structure in Figure 2.1b, where dispersion is given by the straight line $\omega=(c/n)k$. In 2D the dispersion is given by a cone, in 3D by a series of spheres with radius $\omega n/c$ (or, more accurately, two degenerate spheres with equal radius, one for each polarization). These surfaces will deform due to mode repulsion at the edge of the BZ when a modulation of the dielectric constant is introduced, and symmetry restrictions can lead to a lifting of degeneracies. The dispersion surface is obtained by plotting the endpoints of all wave vectors (in all bands) for which the eigenfrequency is equal to ω . This constant-frequency surface is therefore equivalent to the constant-energy Fermi surface of electrons in quantum mechanics.

Several important properties of PhCs can be analyzed using the dispersion surface:

First, conservation of momentum for light coupling from a homogeneous medium (e.g. air) into the PhC across a given surface dictates that $\mathbf{k}_{1\parallel} = (\mathbf{k}_2 + \mathbf{G})_{\parallel}$, where \mathbf{G} is any reciprocal lattice vector. Secondly, it is clearly possible that several Bloch modes fulfill the above condition simultaneously and therefore more than one refracted (or diffracted) wave can exist in the PhC. The third observation is that in PhC the direction of energy transfer does not generally coincide with the direction of the Bloch wave vector which specifies the mode. This simply follows from the fact that along the direction of the Bloch vector the refractive index is not constant and therefore the spatial configuration of the electric field can be very irregular. The direction of energy transport in PhCs is given by the group velocity vector

$$\mathbf{v}_g = \nabla_{\mathbf{k}} \omega(\mathbf{k}) \quad (2.12)$$

and therefore perpendicular to the dispersion surface. These properties are illustrated in Figure 2.4 for the case of an incoming beam \mathbf{k}_1 incident on a 2-D lattice. The direction of Bloch and group velocity vectors for the reflected and refracted beams are analyzed by applying the momentum conservation and causality conditions. The strongly distorted dispersion surfaces can lead to a number of interesting phenomena in PhCs, such as the superprism effect, self-collimation of beams, and negative refraction. As will be discussed in later chapters, they can also lead to angular and spectral redistribution of spontaneous emission in 3-D PhCs. Figure 2.5 shows examples of 3-D dispersion surfaces, calculated for an inverse opal near the primary Γ L partial gap (refractive contrast of $\sim 3:1$) and near the complete PBG (refractive contrast of $\sim 3.5:1$) [16].

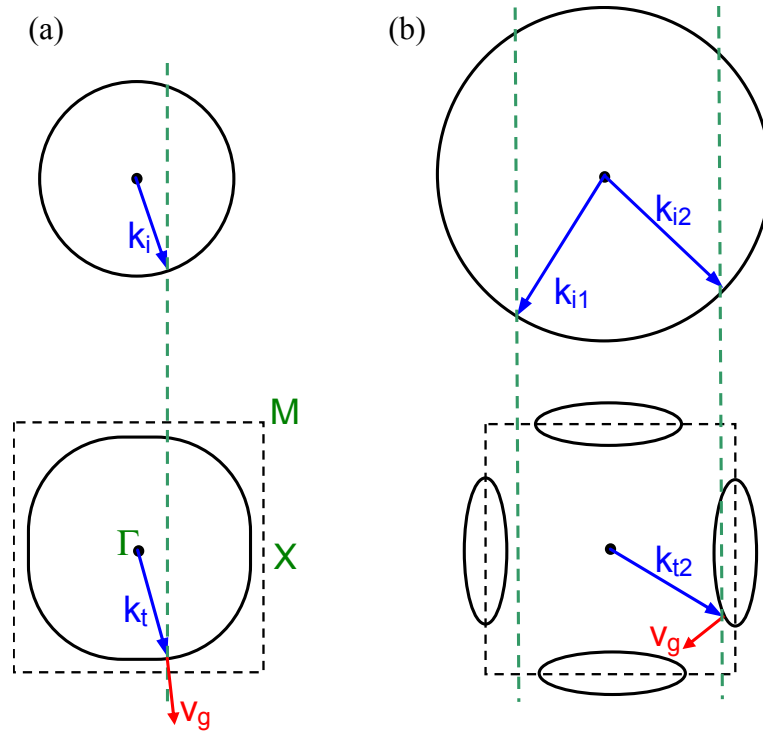


Figure 2.4: Refraction of light in a 2D PhC. For clarity, only the transmitted beams are shown.

The dispersion in air and the incident wave vector are shown on top. The dashed green line shows the condition of conservation of k_{\parallel} . (a) At a frequency below the PBG, the dispersion surface is only slightly deformed, \mathbf{k}_t and \mathbf{v}_g are almost collinear. (b) In this case a stop band has opened at the M point. Waves propagating with \mathbf{k}_{i1} cannot propagate in the periodic structure. For waves with \mathbf{k}_{i2} , the direction of energy flux is different from the transmitted wave vector \mathbf{k}_{t2} .

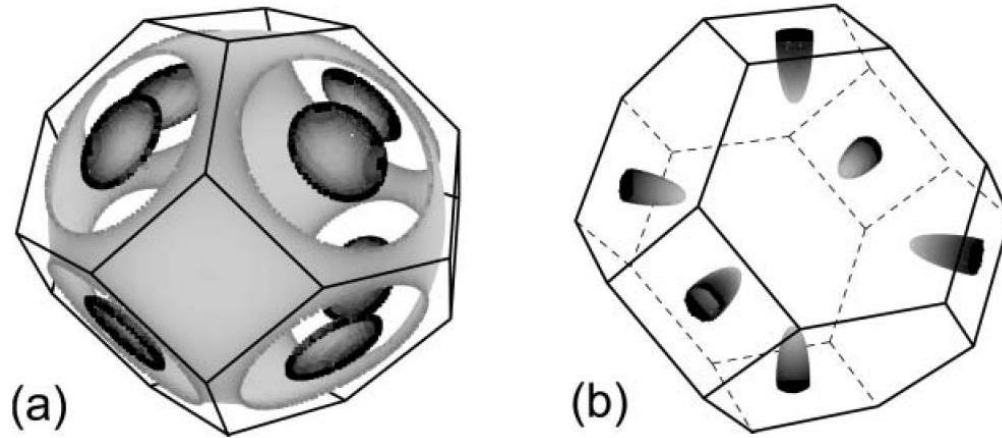


Figure 2.5: (a) Calculated dispersion surface of an inverse opal PhC with $n=3$. for a frequency just above the primary ΓL gap. Only bands 1 and 3 are shown. (b) Dispersion surface just above the complete PBG of a Si inverse opal. The only allowed modes are located in ellipsoid lobes close to the X point. [16]

2.5 Emission from Photonic Crystals

2.5.1 Density of States and Spontaneous Emission

Spontaneous emission is based on the excitation of an emitter into an energized state and subsequent decay via coupling with an available photon mode, emitting in the process a photon of the transition frequency. The total radiative rate Γ of the spontaneous transition is given by the well-known Fermi Golden Rule (within the Wigner-Weisskopf-approximation)

$$\Gamma(\omega) = \frac{2\pi}{\hbar} \rho(\omega) \quad (2.13)$$

where $\rho(\omega)$ is the density of states at the transition frequency ω , which for free space is

$$\rho(\omega) = \frac{\omega^2 V}{\pi^2 c^3} \quad (2.14).$$

It has long been recognized that the radiative decay rate might be altered by the electromagnetic field in the vicinity of the emitter. If the density of EM modes of the transition frequency is zero around the emitter, an excited atom will not be able to couple and decay, i.e. it will stay in the excited state indefinitely and spontaneous emission will be suppressed. This effect will occur for an emitter inside a PhC if the transition frequency lies within a complete PBG. However, if the

transition frequency is near a band edge where the group velocity is reduced and therefore the DOS is enhanced, an enhancement of the radiative rate can be expected (Purcell effect).

Since the density of states of states within a PhC also depends on position within a unit cell, the atomic emission rate may be a function of position. The local density of states (LDOS) $\rho(\omega, \mathbf{r})$ inside a PhC can be defined as

$$\rho(\omega, \mathbf{r}) = \frac{1}{(2\pi)^3} \sum_n \int d\mathbf{k} |\boldsymbol{\mu} \cdot \mathbf{E}_{n,\mathbf{k}}(\mathbf{r})|^2 \delta(\omega - \omega_{n,\mathbf{k}}) \quad (2.15)$$

where $\boldsymbol{\mu}$ is the dipole transition moment of the emitter. The integral runs over all wave vectors within the first BZ. There are several consequences of this definition: To observe a significant effect of the local density of states on the decay rate, the spectral width of the emission has to be narrow enough to overlap completely with the PBG. Otherwise the averaged LDOS will be probed and little effect on the emitter lifetimes can be expected. Furthermore, because total radiative rate Γ and the total LDOS are angle-integrated properties, they will not be significantly affected by directional stop gaps and they cannot explain angle-dependent changes in the emission spectra. In order to account for angular changes in the emission due to partial gaps (where the density of modes emitting in the direction of the gap is zero) or flat bands (where the directional density of states can be greatly enhanced), we will have to calculate the directional DOS, which only takes into account the fraction of modes emitting in a certain direction, as will be discussed in Chapter 6. Lastly, the position of the emitters within the photonic structure is critical to the observed optical properties. Because the LDOS differs significantly between the

air and the dielectric part of the structure, a PhC fabricated from a fluorescent or optically active material will emit differently than a passive PhC with infiltrated light sources.

2.5.2 Localization of Light and Lasing

Lasing in PhC is based on their ability to confine and localize light in a material in ways which cannot be realized in other structures. Light localization can be achieved by several mechanisms. In disordered media, interference of scattered waves can become strong enough to cause localization when the average scattering length (or the photon mean free path) approaches the wavelength. This phenomena is known as Anderson localization, first described for electron waves in solids [17, 18]. Cao et al. have shown that so-called random lasing can occur in strongly disordered media [19], a process where scattering leads to the formation of random feedback loops in the material (Figure 2.6). Some of the initial interest in PhCs was sparked by John's proposal that Anderson localization of light would be more easily achieved in certain PBG structures with controlled disorder [9].

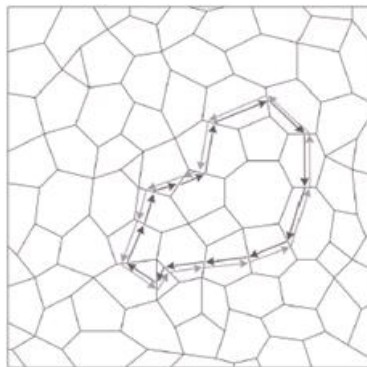


Figure 2.6: Random lasing by feedback loops in a disordered medium.

The creation of a PBG in an ordered PhC structure introduces new physical possibilities. Just as a semiconductor can be doped to introduce electronic states within the band gap, artificial defects can be introduced to the PhC structure that act as microcavities and create isolated states within the PBG. Such defect states are associated with spatially confined electromagnetic modes with frequency in the PBG which cannot leak into the surrounding PhC structure. These modes would in theory be loss-less and, since lasing occurs when gain overcomes losses, allow threshold-less lasing. This defect-mode lasing mechanism has been applied very successfully in 2-D PhCs, where it is straightforward to produce a designed 0-D or 1-D defect in the pattern. Extremely high quality factors of $\sim 10^8$ (theoretical) and $\sim 10^6$ (experimental) have been reported for such 2-D microcavities [20].

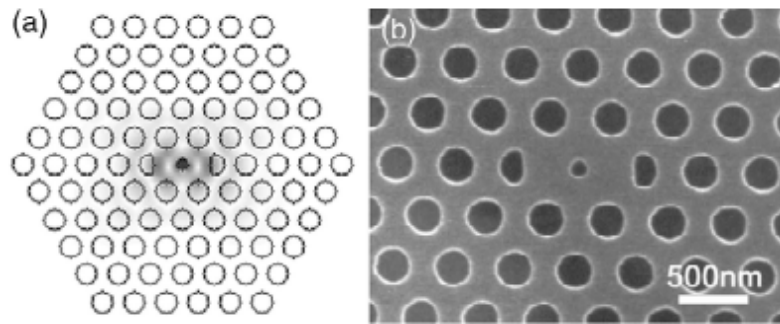


Figure 2.7: (a) Cavity design and electric field distribution for a 2-D microcavity laser. (b) SEM image of fabricated cavity. [21]

Fabricating engineered defects inside a 3-D structure is much more complicated, especially at the length scales necessary for visible to UV operation. A lot of research is targeted at solving this problem, but for now other approaches remain more feasible.

As discussed above, the group velocity of light \mathbf{v}_g in a PhC is given by the gradient of the eigenfrequency ω versus the wave vector \mathbf{k} and therefore goes to zero at the edges of a PBG (Equation (2.12)). A reduction of \mathbf{v}_g results in a longer interaction time of light with the material and leads to an enhancement of the optical response of the material. An enhancement of stimulated emission can lead to a large reduction in the lasing threshold [2]. This effect is well known as distributed-feedback lasing, which occurs in slowly propagating modes near Bragg diffraction resonance in a 1-D multilayer stack (i.e. a 1-D PhC). The unique dispersion relation of 2-D and 3-D PhC, which includes higher-order flat bands that are folded into the BZ by lattice vectors not collinear with the propagation direction, leads to the so-called *group velocity anomaly* [2, 22]. This means that \mathbf{v}_g is small over the entire frequency- and \mathbf{k} -range of these bands, leading to a large effective coupling between the EM mode and the material system. The lasing threshold of these modes has been shown to be far smaller than at the edge of the first-order PBG [22]. The effect of the group velocity anomaly on the lasing properties of ZnO inverse opal PhCs will be the subject of Chapter 5.

2.6 Fabrication of Three-Dimensional Photonic Crystals

2.6.1 Fabrication Methods

From Equation (2.3) we see that the length scale of dielectric periodicity of a PhC (i.e. its lattice constant) is determined by the wavelength of operation. If the operation in the visible spectrum is desired, this typically means a periodicity on the order of 150 to 300nm, with minimum feature sizes less than 100nm. Achieving good 3-D order at these dimensions poses a challenge to traditional microfabrication methods, which are usually targeted at the planar 2-D architectures of semiconductor technology, and several promising new methods have been developed to overcome the limitations. At the same time, much theoretical work has been aimed at finding new structures that allow PBGs to form at low (scaled) frequencies a/λ .

The earliest material reported to exhibit a complete PBG was developed by Yablonovitch and appropriately dubbed “Yablonovite.” This structure was fabricated by mechanically drilling millimeter-size holes into a dielectric block and possessed a PBG in the millimeter wave range [23]. Use of focused ion beam (FIB) drilling allowed for a PBG in the infrared region, but the resolution and laborious processing limit the applicability of this approach at shorter wavelengths.

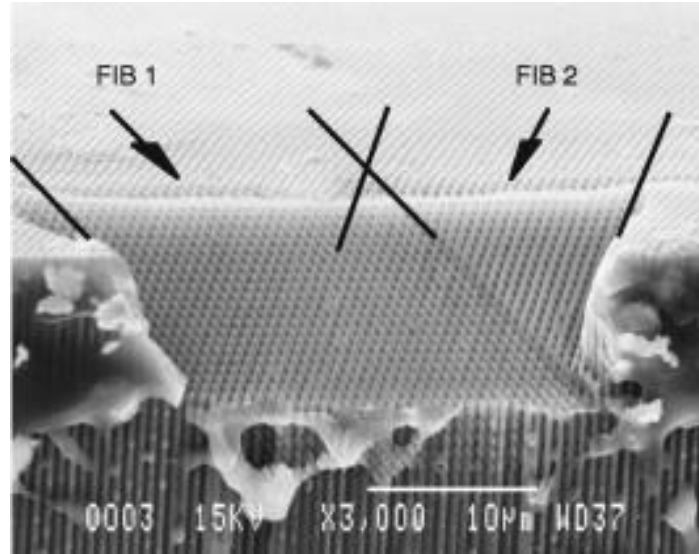


Figure 2.8: Silicon yablonovite fabricated by FIB drilling. [24]

Several methods have been developed to fabricate the so-called *woodpile* structure, which is related to the diamond structure.: Ozbay et al. have used “micromachining” of Si wafers [25], and Lin et al. [26] employed a layer-by-layer process involving multiple steps of film deposition, lithography and etching (Figure 2.9) to fabricate PhCs for the infrared (IR) regime. Woodpile structures working in the IR range have even been created by stacking pre-patterned Si building blocks by micromanipulation [27]. Another layer-by-layer process based on lithography has been developed at MIT that allows incorporation of pre-designed defects into the 3-D structure [28]. Unfortunately all these fabrication methods are extremely laborious and time and cost intensive.

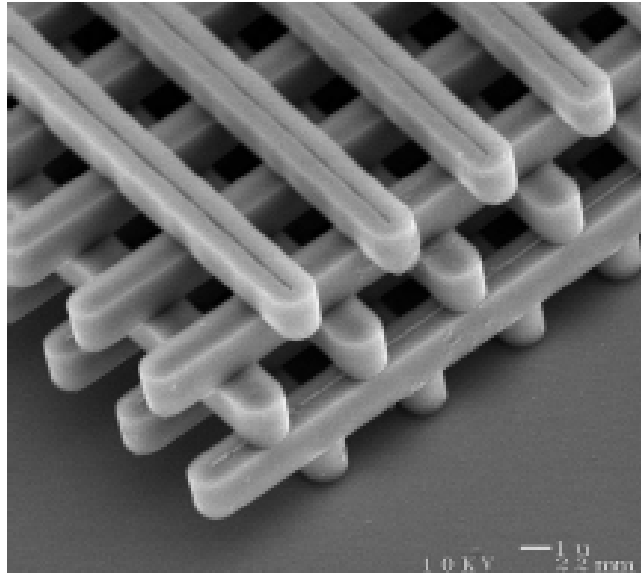


Figure 2.9: Si woodpile structure. [26]

Recent advances in “rapid prototyping” methods such as direct writing [29] and two-photon polymerization [30, 31] show the potential of such approaches for the fabrication of 3-D structures. An example is shown in Figure 2.10 where a 3-D woodpile structure is directly deposited using a colloidal gel by a process similar to ink-jet printing. Another promising approach is based on 3-D holographic lithography [32-36], in which a layer of photoresist is exposed to a 3-D interference pattern created by overlapping several laser beams (Figure 2.11). This method is fast and able to create a variety of structures by controlling the mutual alignment and phases of the laser beams, but can only fabricate structures with limited thickness due to the gradual decrease in light intensity (and therefore feature size) caused by absorption. (A related technique using an optical phase mask to create an interference pattern has also been suggested recently [37].)

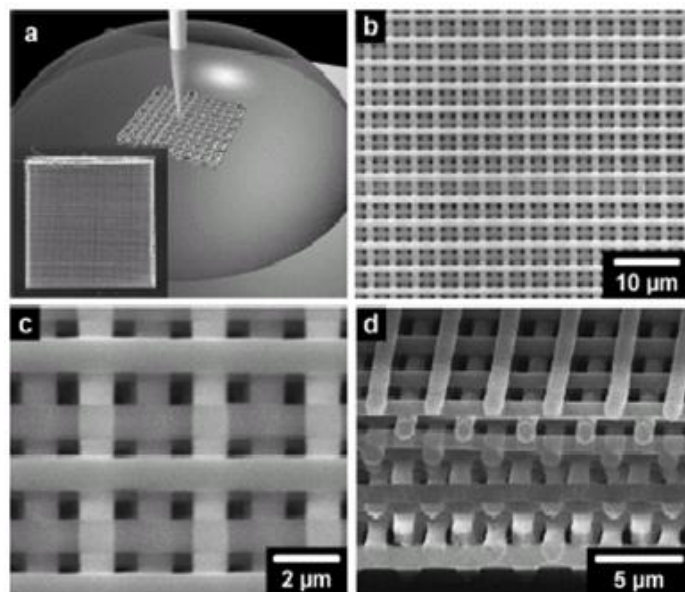


Figure 2.10: 3-D PhC fabricated by direct writing. [29]

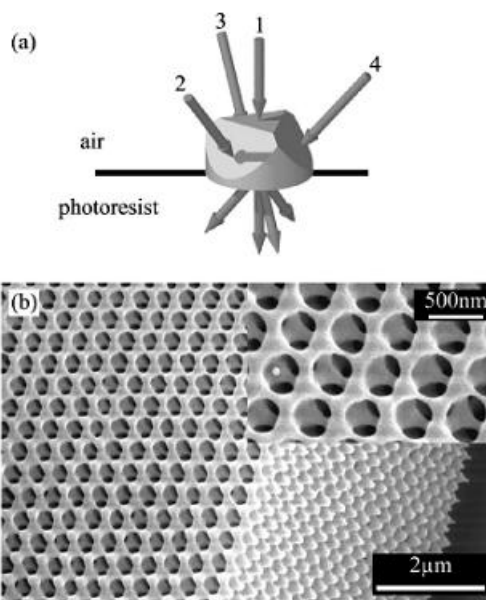


Figure 2.11: (a) Beam diagram for 3D holographic lithography using a coupling prism. (b) Example of FCC structure fabricated in photoresist. [32]

Although these direct-write and holographic methods typically generate low-refractive index polymer structures, inversion by liquid-phase infiltration, CVD [38], or ALD [36] can be used to replicate create higher contrast PhCs.

2.6.2 Fabrication of 3-D Photonic Crystals Based on Colloidal Self-Assembly

2.6.2.1 Fabrication of Artificial Opals

By far the most widely used and most extensively studied method used for fabricating 3-D PhC structures is based on self-assembly of monodispersed colloidal spheres into so-called “artificial opal” structures. The spheres are typically made of silica, PMMA or polystyrene, and can be relatively easily synthesized with a narrow size distribution. Monodispersed spheres are also available from a number of different commercial vendors.

Colloidal crystals have traditionally been assembled by simple sedimentation, but more advanced techniques are now available to grow well-aligned fcc crystals with few stacking faults: Park et al. have used lithographically defined confinement cells to grow colloidal crystals with defined thicknesses [39]. Jiang et al. have developed a vertical deposition method that relies on the spontaneous self-assembly of monodispersed particles into ordered arrays due to the capillary force in the moving meniscus of an evaporating suspension [40]. This method is widely used for the assembly of high-quality artificial opals [4, 6] and can be combined with substrate patterning [41] and templating [42, 43] to create more complex structures. Figure shows an example of thin opal film deposited in this way. Experimental details will be provided in Chapter 3. One of the main advantages of this growth method over alternatives is the well-defined orientation of the fcc crystal structure: The spheres reliably self-assemble with the (111)

crystal surface parallel to the substrate and the [110] direction oriented along the growth direction (i.e. along the direction of the moving meniscus), and the structures contain very few stacking faults. This allows one to measure direction-dependent optical properties of the PhCs and compare them to the band structure calculations.

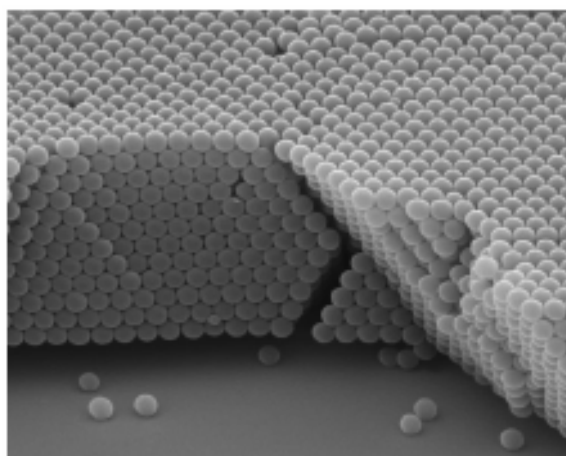


Figure 2.12: Example of thin film opal of silica spheres.

2.6.2.2 *Infiltration of Opal Templates and Materials Selection*

So far, the discussion of PhC has been mostly concerned with the general requirements of structure, independent of the specific material system. Optimization of the photonic band structure suggests the use of fcc crystal structures (the diamond structure would be ideal, but is impossible to self-assemble) and a low-filling fraction of the high- ϵ component to maximize the photonic strength. The general process of opal infiltration and inversion is shown schematically in Figure 2.13.

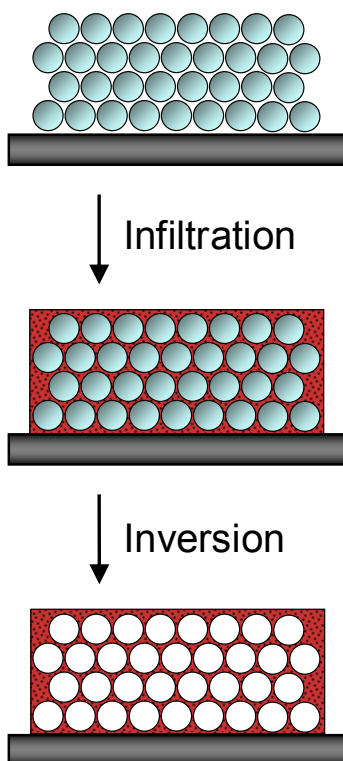


Figure 2.13: Schematic of opal infiltration and inversion process.

The material properties will determine the dielectric contrast and the optical response (e.g. emission properties). In contrast to the simple opal structure, inverse opals are able to possess a complete PBG if the refractive index is high enough (>2.8) [44, 45].

Many groups have shown that infiltration of opal templates is a successful strategy to create 3-D PhCs for a variety of materials systems. Several routes have been pursued, the most common approach being liquid phase methods such sol-gel infiltration or solution precipitation [46-48], electrodeposition [49, 50], and liquid metal infiltration [51]. However, the adopted method must be capable of filling the interconnected network of submicron pores inside the

template, and liquid phase techniques often result in low filling fractions and disorder due to randomly distributed voids. Typical filling fractions for these techniques are on the order of 10-12% [47], or ~50% of the available pore volume in a close-packed sphere lattice.

Good infiltration of opal templates is easier to achieve by vapor phase methods, such as chemical vapor deposition (CVD), which has been used for InP [52, 53], GaP [54], and TiO₂ [52], amongst others [55-57]. However, it is still difficult to avoid porosity because the film growth has a tendency to fill in the top pores and prevent full infiltration. Low pressure CVD has been used for infiltration of both silicon and germanium, with filling fractions ranging from 1-100% [58, 59]. This method produces the best filling fraction and film quality of any technique reported other than ALD and can also deposit multilayer materials [60]. The high index of these materials make them attractive for near-IR telecommunications wavelengths, but they absorb light in the visible spectrum.

In the work performed here, atomic layer deposition (ALD) was used for infiltration. Apart from the ZnO work reported here, ALD has been used to fabricate inverse opal structures of WN [61], ZnS [62], Ta₃N₅ [63], TiO₂ [64], and GaAs [65]. ALD allows for completely conformal film growth and therefore offers precise control over the infiltration, as will be discussed in more detail in the next chapter.

3. Fabrication of ZnO Inverse Opals by Atomic Layer Deposition

3.1 Introduction

Since photonic crystals (PhCs) were first proposed in 1987 by Yablonovitch [8] and John [9] they have been studied with great interest as a means of localizing light and modifying the emission properties of embedded light sources [66-68]. To study this effect, it requires efficient emission in the medium and a photonic band gap (PBG) that overlaps the emission spectrum. Material infiltration of three-dimensional (3D) colloidal crystals has been shown to be a versatile method to fabricate so-called “inverted opal” structures which have the long-range order, high filling fraction, and refractive index contrast required to exhibit a photonic band gap. Infiltration has been achieved by various methods, including chemical bath deposition [47], electro-deposition [50, 69], sol-gel methods [70], and low-pressure chemical vapor deposition (CVD) [71, 72]. (See Lopez [4] for a recent review). But achieving both high filling fractions and good luminescence properties of the material has proven difficult. Several groups have therefore studied the emission properties of lasing dyes or quantum dots infiltrated into opal or inverted opal backbones [66, 68, 73, 74].

Recently, atomic layer deposition (ALD) has been proposed as a promising route to fabricate inverted opal structures [61, 62]. ALD is a modified CVD growth method in which a

binary synthesis reaction is split into two self-limiting surface reactions by separate sequential exposures of the substrate to the chemical precursors. The resulting surface control and monolayer-by-monolayer growth sequence result in the formation of uniform and defect free films that are conformal to the substrate shape. In addition, ALD is a versatile and robust synthesis method which allows growth of a variety of materials under a wide range of conditions.

For this thesis a complete process for the fabrication of 3D ZnO PhCs was developed, starting with the synthesis of polystyrene opal templates based on a vertical self-assembly method. These templates are then infiltrated by a low-temperature ALD process using diethyl zinc (DEtZn) $[\text{Zn}(\text{C}_2\text{H}_5)_2]$ and water as precursors, and inverted by firing. The resulting structures are characterized by scanning electron microscopy (SEM) and X-ray diffraction (XRD). The optical quality is analyzed by photoluminescence, and photonic band structure of the PhCs is experimentally verified by transmission and reflection spectroscopy.

3.2 Previous Research on ZnO Photonic Crystals

The interesting material properties of ZnO have motivated several groups to try and fabricate ZnO photonic crystal structures. Sumida et al. reported the fabrication of ZnO inverse opals using electrochemical deposition [50], but the filling fraction and orderness of those macroporous films was poor and no optical properties were reported at the time. Research in our group was initially based on the synthesis and self-assembly of monodispersed ZnO colloidal spheres using the polyol synthesis method in diethylene glycol solvent, resulting in the first

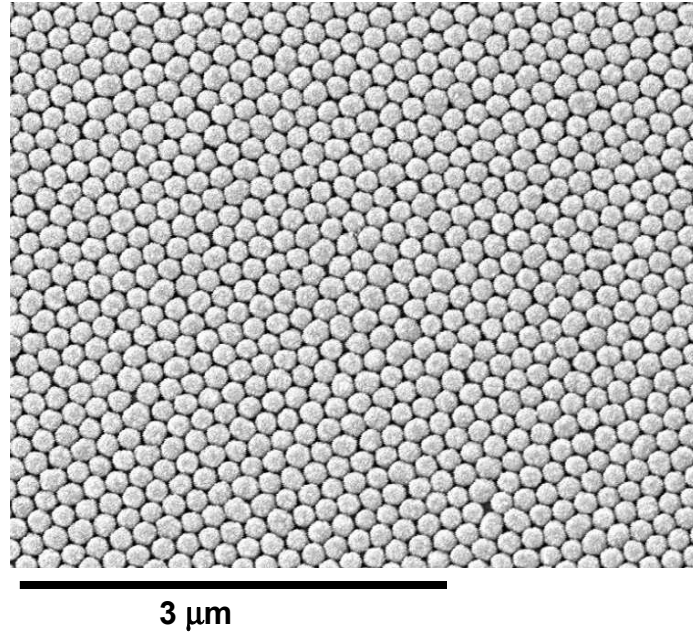


Figure 3.1: ZnO opal fabricated by self-assembly by of monodispersed ZnO particles.

published report of 3D ZnO PhCs [75]. An example of such a ZnO opal film is shown in Figure 3.1.

Because the uniformity of the ZnO spheres is far inferior to silica or polystyrene colloidal spheres and their refractive index is relatively low compared to bulk ZnO (due to the porous polycrystalline substructure), the PBG effect in these opals is weak [75]. Photonic crystal lasing was achieved in 2D ZnO PhC slabs [76], demonstrating the potential usefulness of photonic ZnO devices and motivating us pursue routes to improve the 3D structures.

Several groups have infiltrated nanocrystalline ZnO into silica opal structures and investigated the effect of the first stop gap on the UV emission [77, 78]. However, the refractive

index contrast of such composite PhCs is weak and the infiltration (by spray pyrolysis [77] or solution precipitation [78]) introduces significant disorder into the PhCs.

After our first publication of the ALD fabrication of ZnO inverse opals, Juarez et al. also reported on a similar method of infiltrating polystyrene opals using a sequential CVD method [79].

3.3 Atomic Layer Deposition of ZnO

3.3.1 Principles of Atomic Layer Deposition

Atomic layer epitaxy (ALE) was developed in the 1970s as a method to grow thin electroluminescent films on large and non-planar substrates [80]. ALE began to attract considerable attention in the following decades as a method for producing high quality films and has steadily grown in importance due to its ability of growing ultra-thin and highly conformal layers. Since the method has been extended to the growth of semiconductors, oxides, and metals [80-83] on a variety of substrates it is now more commonly referred to as ALD.

The basic advantage of ALD lies in the fact that the film growth is surface controlled, rather than source controlled as in CVD or molecular beam epitaxy (MBE). This is achieved by using sequential exposures, separating the (usually binary) reaction between the precursor compounds into two half-reactions. During each half-reaction only one monolayer of the reactant chemisorbs (or is chemically bound) on the surface. If the substrate temperature is kept sufficiently high, further layers which are only physisorbed are removed by an inert gas purge

before the other reactant is introduced. As a result, the process proceeds step-wise in self-limiting surface reactions, separated by purge steps. Each full reaction cycle leads to the formation of (ideally) one monolayer. Accordingly, the film thickness is determined by the number of reaction cycles and the growth rate mainly depends on the length of each exposure/purge cycle. The temperature must high enough to prevent condensation and to provide activation energy for any chemical reactions to occur, yet low enough to prevent decomposition of the precursors or re-evaporation of the reaction product. These requirements usually result in an allowed “processing window” of the ALD process [84]. If the precursors actually chemically react on the surface (as in the case of organometallic or halide precursors reacting on a hydroxylated oxide surface) this temperature window is not limited by the balance of chemi- and physisorption and ALD growth can occur over a wide range of temperatures.

It should be noted that true monolayer coverage of the surface is only possible in the case of elemental precursors (e.g. $\text{Zn} + \text{S} \rightarrow \text{ZnS}$). Full saturation is usually prevented by the steric hindrance of the reactant molecules and also depends on the number of active sites available for chemisorption or reaction on the substrate surface [82, 85]. The involved surface chemistry is often complex and the reaction can be complicated by secondary reactions and desorption [82].

One of the major technological limitations of ALD is slowness – typically only a fraction of a monolayer is deposited per cycle and many hundred cycles are necessary to grow layers with several tens of nanometers thickness.

3.3.2 Advantages of ALD for Photonic Crystal Infiltration

ALD allows for the growth of high-quality and very conformal films even on substrates with complex surface geometries. It has been used to infiltrate pores of anodized alumina membranes [86] and deposit high-aspect ratio multilayer composite films [87] (Figure 3.2).

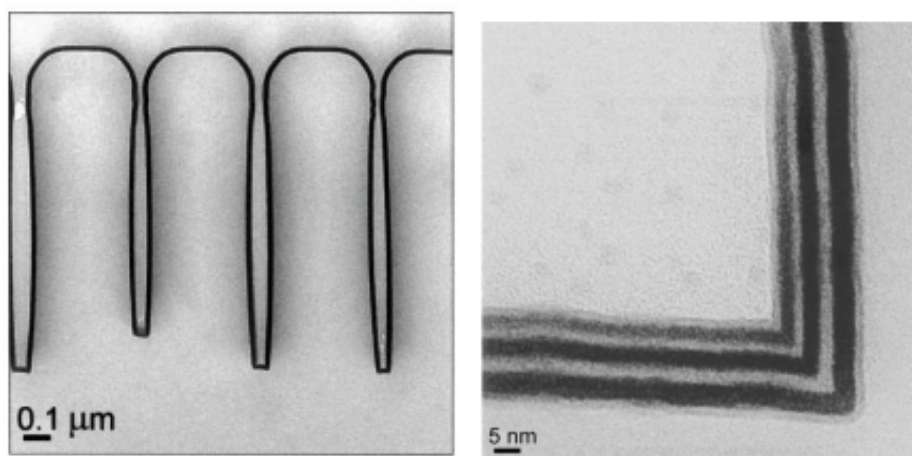


Figure 3.2: TEM images of $\text{Hf}_x\text{Al}_y\text{O}_2$ composite structure. Right image is detail of bottom corner. [87]

This makes it an ideal tool for the infiltration of opal PhC templates. Inverted opals of WN have been grown with ALD [61], and King et al. have fabricated ZnS photonic crystals with high filling fractions and good luminescence properties [62]. The conformal growth means that 100% infiltration of the internal pore structure of the opal templates is not possible. Rather, infiltration will come to a halt once the film growth closes off the narrowest diffusion channels into the structure, and further reaction cycles will deposit material on the outside of the structure. The smallest pore diameter in a close-packed sphere structure occurs between three spheres in the

close-packed (111) surface of the structure, as depicted in Figure 3.3. Therefore, the maximum layer thickness x which can be grown inside an opal is

$$x_{\max} = \left(\frac{1}{\sqrt{3}} - \frac{1}{2} \right) d \approx 0.0774d \quad (3.1),$$

i.e. infiltration will end once the coating thickness reaches 7.74% of the sphere diameter.

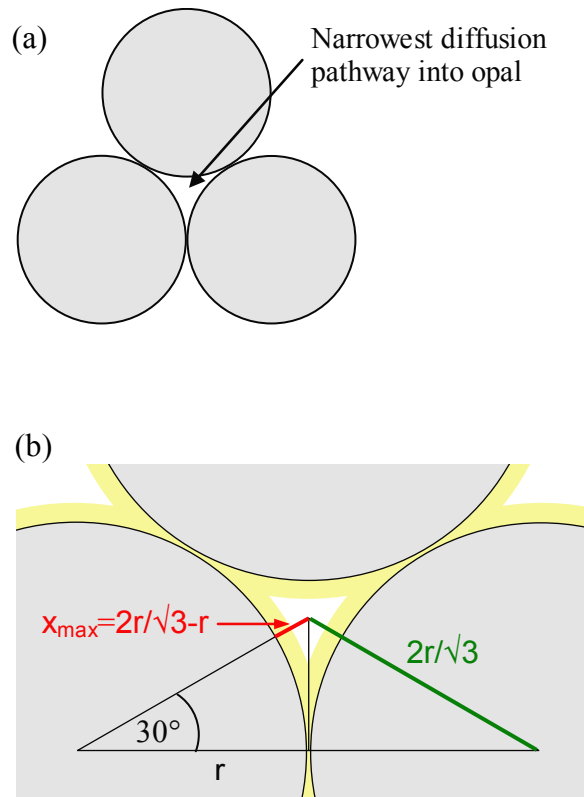


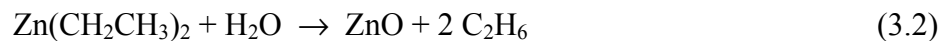
Figure 3.3: (a) The narrowest channel for precursor diffusion into the opal structure is defined by 3 close-packed spheres in the (111) surface. (b) Illustration of pore geometry determining the maximum film thickness.

The resulting structure is an FCC array of dielectric shells in an air matrix and voids remain in the tetrahedral and octahedral interstitial positions of the fcc lattice. As a consequence, only ~86% of the available pore volume can be infiltrated. (If the opal template is assumed to be an ideal close-packed structure of spheres with the minimum possible pore volume of 26%, this results in a maximum total filling fraction of 22.4% for the ALD-grown material.) However, it is important to realize that the remaining porosity is not randomly distributed, as is typically the case for liquid-phase or CVD infiltration, but forms an ordered sublattice in the FCC structure, and detailed modeling of the photonic band structure has shown that this type of incomplete filling can actually increase the width of PBGs and lead to additional “flattening” of higher-order bands [45, 88, 89]. For example, in a silicon inverse “shell” structure, the width of the PBG can be increased from 4.25% (for a fully infiltrated inverse opal) to 8.6% when the opal porosity is infiltrated conformally with only 90% dielectric material [45].

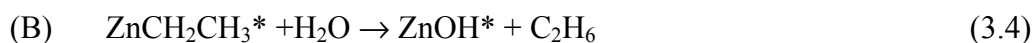
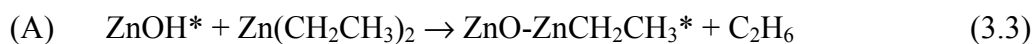
The ability of the ALD method to grow multilayer films has also been used to fabricate composite inverse opal structures, e.g by combining a high-dielectric material (TiO_2) with a luminescent materials (ZnS) [90].

3.3.3 ALD Growth Mechanism of ZnO

ZnO is a wide band gap semiconductor and transparent conductive oxide with many applications in solar cells, displays, excitonic lasers, and gas sensors, and the ALD synthesis of ZnO films has been demonstrated by several researchers [86, 91-94]. ALD growth of ZnO is based on the binary CVD reaction between DEtZn and water:



ALD growth is supposed to occur by splitting this reaction into the separate surface reactions:



where * denotes a surface species. Due to the reactivity of the organometallic precursor, this process can be operated at low temperatures. Figure 3.4 shows a typical gas pulse sequence used for ZnO ALD: Alternating exposures to the reactants in a ABAB... sequence leads to the layer-by-layer growth of ZnO as illustrated in Figure 3.5.

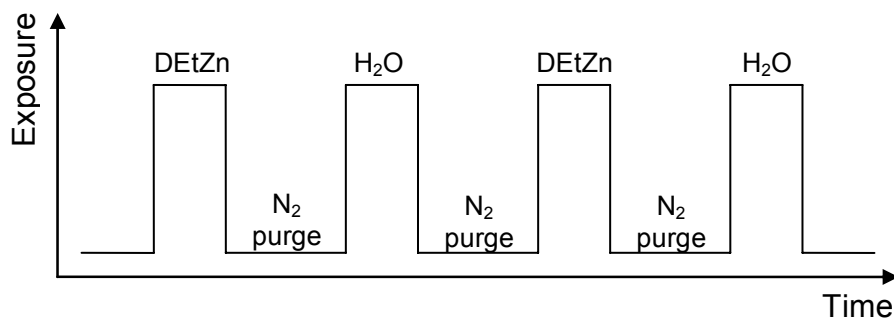


Figure 3.4: Typical pulse sequence for one ALD reaction cycle.

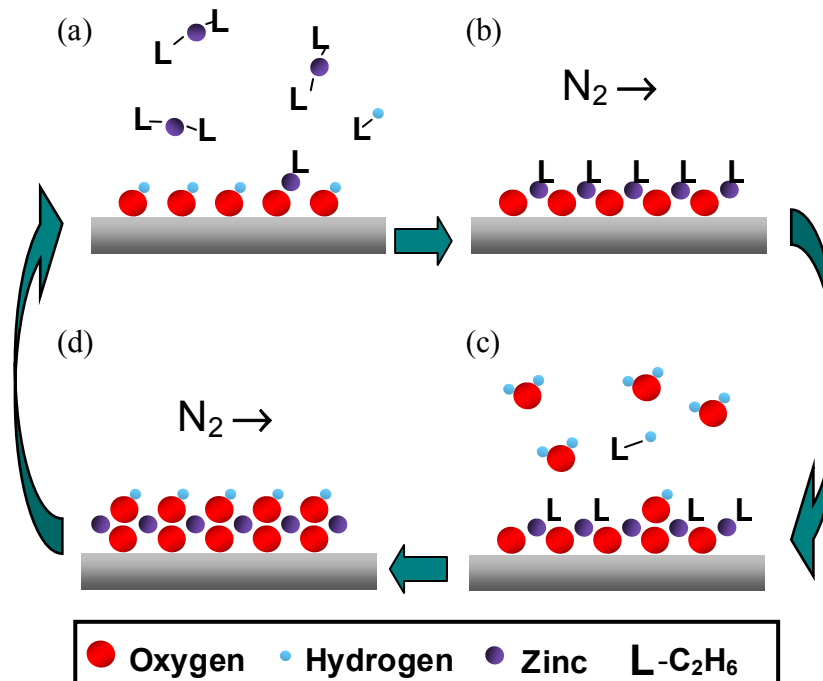
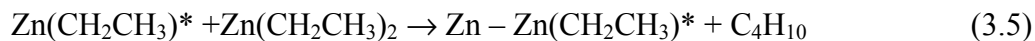
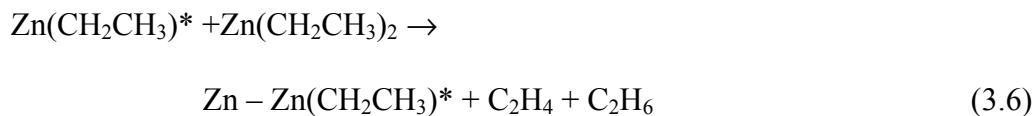


Figure 3.5: ALD growth of ZnO from $\text{Zn}(\text{C}_2\text{H}_5)_2$ and H_2O .

Growth rates between 1.5\AA and 2.2\AA per cycle have been measured [92, 94]. In reality, the surface chemistry is more complicated than suggested by the idealized reactions (A) and (B) above. For example, detailed studies of the surface chemistry during growth, using quartz crystal microbalance (QCM) monitoring [93] and in-situ Fourier-transform infrared (FT-IR) spectroscopy [94] at 450K suggest that the DEtZn reaction is not entirely self-limiting and can involve secondary reactions of the type:



or



which lead to the deposition of metallic Zn. These reactions are much slower than reactions (3.3) and (3.4), however, and can be minimized by limiting the exposure times. The decomposition of DEtZn is also less likely to occur at lower reaction temperatures.

3.4 Experimental Methods

3.4.1 Fabrication of Polystyrene Opal Templates

3.4.1.1 *The Vertical Self-Assembly Method*

Previous work of ALD fabrication of inverse opals was based on silica opals which were infiltrated at high film growth temperatures [61, 95]. The silica template can subsequently be removed by etching with HF acid. Because ZnO is easily etched by HF itself, however, this method was not viable for the synthesis of ZnO inverse opals. Instead, we developed a process based on the self-assembly of polystyrene (PS) spheres which were then infiltrated at low temperatures (below the glass transition temperature $T_g \sim 95^\circ\text{C}$ of PS).

For this research, monodispersed colloidal PS microspheres were purchased from Seradyne Inc. in sizes ranging from 160nm to 400nm. The exact particle sizes were measured by SEM,

and the size distributions of the samples were found to be between 2.5% and 4%. Both plain and carboxylate-modified PS spheres were used in this project, as discussed below.

For the opal synthesis the vertical convective self-assembly method first developed by Jiang et al. [40] was used, which is capable of growing high-quality opal films with large, well-oriented crystal domains. A substrate is placed into a vial containing a suspension of monodispersed colloidal spheres of controlled concentration, and the solvent is slowly evaporated. As the liquid evaporates the meniscus sweeps down along the substrate surface and the capillary force in the meniscus draws in spheres from the suspension which self-assemble into an FCC structure on the substrate surface. This process is schematically depicted in Figure 3.6. The exact growth mechanism in this method is complex and not yet fully understood, but detailed studies have shown that the self-assembly into an FCC structure with very few stacking faults does not just rely on thermodynamics but also depends on the microfluidic flow of solvent and the particle aggregation at the air-solvent interface [96-98]. For the time being, most studies of growth conditions and resulting opal quality are highly empirical [99] and growth conditions have to be adjusted and optimized for the particular laboratory conditions.

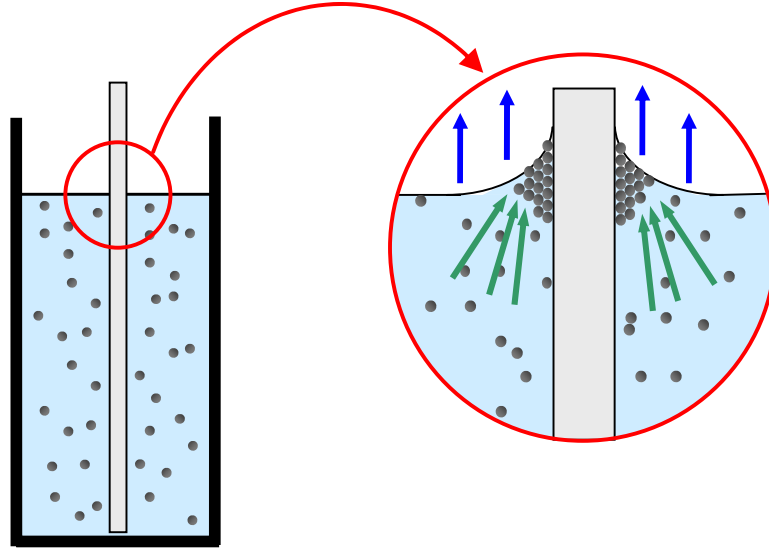


Figure 3.6: Vertical convective self-assembly method: A flat substrate is placed into the colloidal suspension and the solvent is evaporated, causing the particles to self-assemble in the meniscus.

The multilayer thickness is given approximately by the equation [40]:

$$k = \frac{\beta L \varphi}{0.605d(1 - \varphi)} \quad (3.7)$$

where k is the number of layers, L is the meniscus height, β is the ratio between the particle velocity in suspension and the fluid velocity and is taken to be 1, d is the particle diameters, and φ is the particle volume fraction of the suspension. Therefore the number of layers depends on the particle concentration of the suspension and can thus be varied in a controlled fashion.

For this research, polystyrene opals were deposited on glass or quartz substrates (standard microscope slides). The substrates were carefully cleaned with a critical cleaning detergent and

then placed into small vials containing well-dispersed suspensions of colloidal spheres in high-purity deionized water. The water was then slowly evaporated at 50°C over a period of roughly 60 hours in a drying oven. The suspensions typically had a particle volume concentration of 0.1 – 0.3%, depending on the particle diameters and intended film thickness, which yielded opals with a thickness between 20 and 100 layers. While the spheres initially assemble into almost single-crystalline colloidal crystals, during drying shrinkage and the relatively high surface tension of water leads to unavoidable formation of cracks running perpendicular to the substrate surface. While this limits the size of in-plane single domains to several tens by hundreds of microns, the crystal orientation is preserved across the cracks over a range of 1 - 2cm and the samples show uniform coloration .

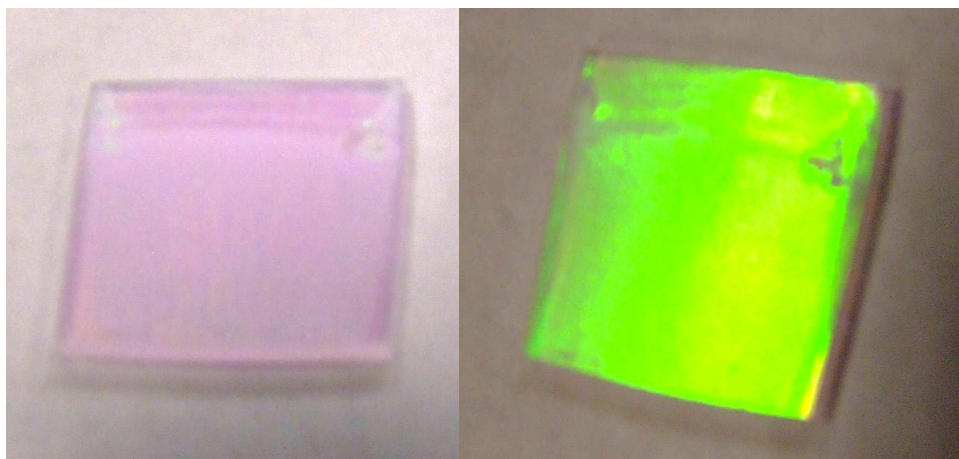


Figure 3.7: Photographs of PS opal sample ($d=256\text{nm}$) under two different illumination conditions, showing transmitted (left) and reflected (right) color. The sample size is $\sim 10 \times 12\text{mm}$.

3.4.1.2 Choice of Opal Template Material

As mentioned above, previous work of ALD fabrication of inverse opal PhCs had used silica spheres as a template material, which are incompatible with ZnO infiltration due to the required HF etch. Monodispersed PS colloidal spheres are readily available from commercial suppliers in the required size range (~150 to 400nm diameter), and the first attempts of ALD infiltration of plain PS templates showed promising results (Figure 3.8).

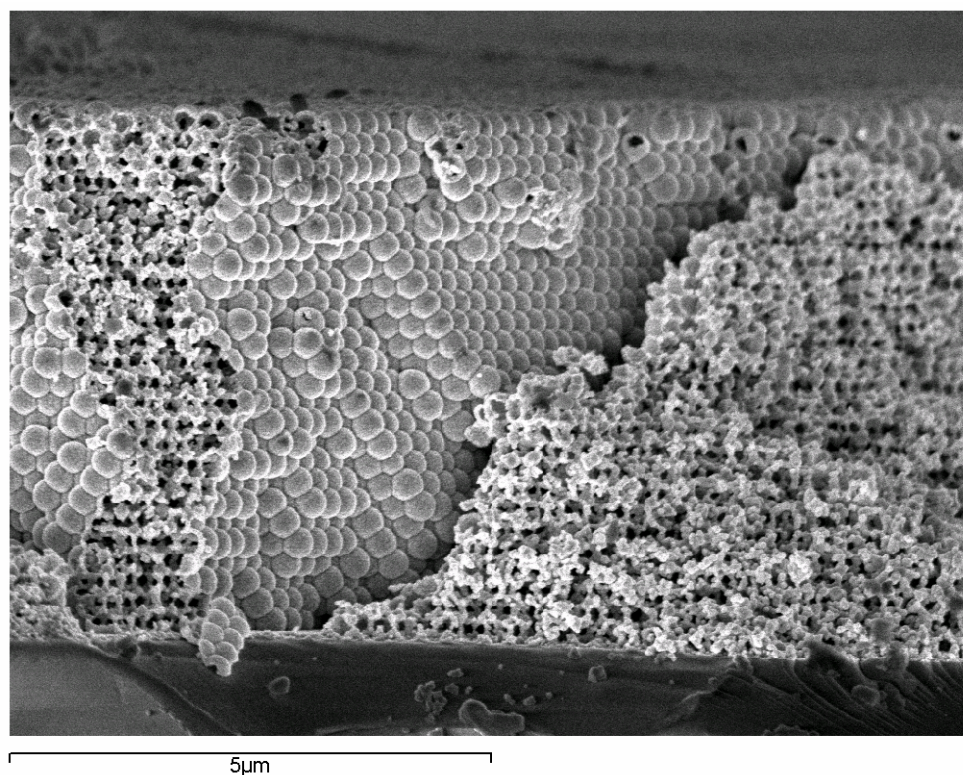


Figure 3.8: Cross-sectional scanning electron micrograph of ZnO inverse opal fabricated by infiltration of a template of plain polystyrene spheres. The image shows the corner of a crystal domain of the inverse opal, with a ZnO film grown conformally around each sphere and inside the structure.

However, these early attempts resulted in low-density films and structures with low filling fraction since plain polystyrene has a hydrophobic surface and there are few sites for the precursor molecules to bond. To improve film properties, we therefore used carboxylate-modified polystyrene (CM-PS) particles for opal assembly. PS colloidal spheres are synthesized by emulsion polymerization of styrene monomer in water. For CM-PS acrylic acid is copolymerized with the styrene, which results in a much more highly charged surface due to the carboxyl groups. These can act as active sites for covalent coupling of precursor molecules and therefore help to initiate the growth of a dense ZnO film during ALD. Since the acid content of PS is a weight-based quantity, CM-PS spheres are best characterized by the density of charged groups on the surface, sometimes referred to as “parking area” (given as $\text{\AA}^2/\text{charged group}$). The CM-PS spheres used here had a medium acid content resulting in parking area of $\sim 40 \text{\AA}^2$. Figure 3.9 shows a comparison of two inverse opals grown in a plain and CM PS templates.

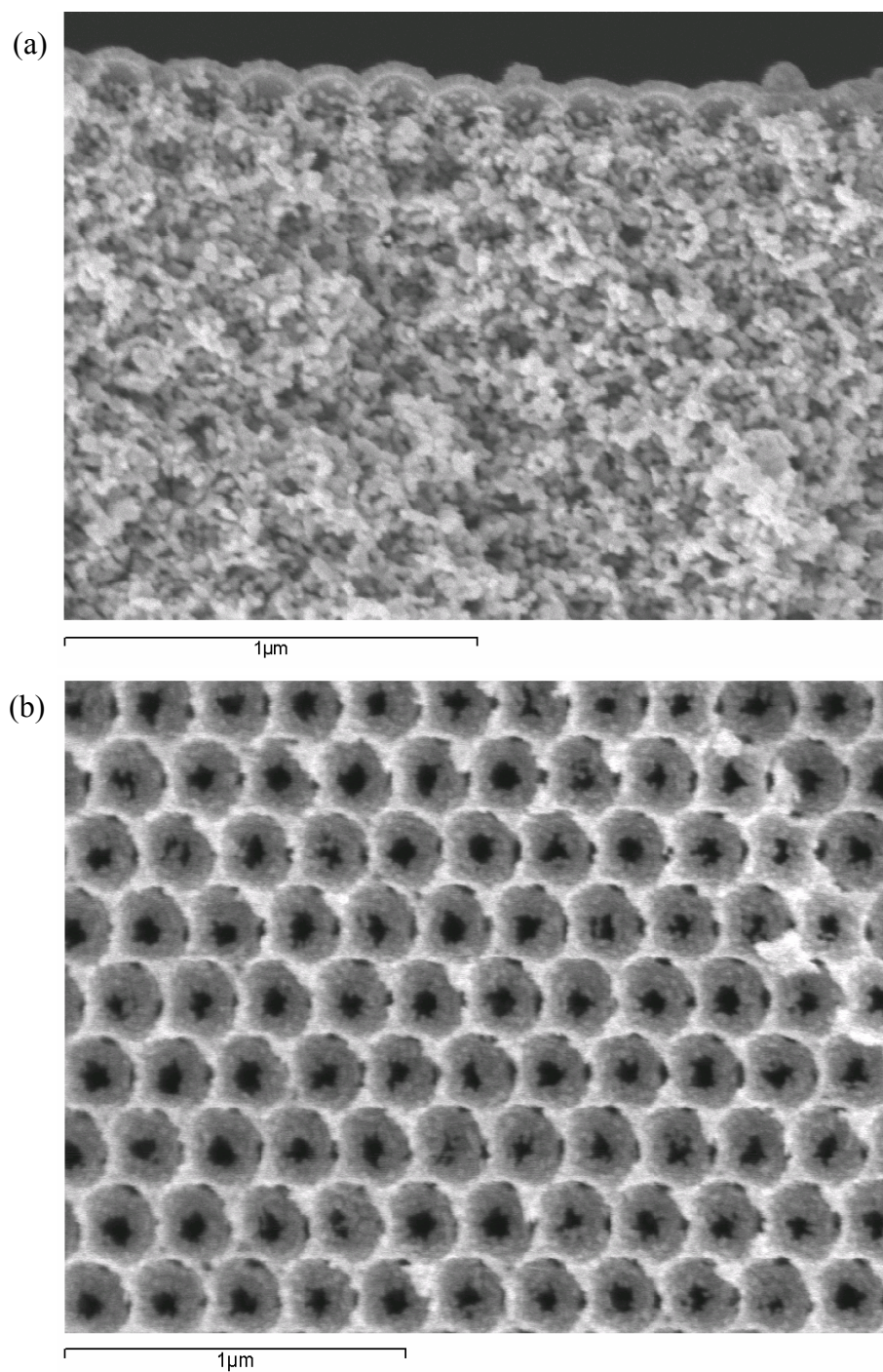


Figure 3.9: (a) ZnO inverse opal, fabricated using a plain PS template, $d=250\text{nm}$. (b) ZnO inverse opal based on CM-PS, $d=256\text{nm}$. Both structures were fired in air at 450°C for 3 hours. The plain PS results in low-density films and low filling fraction.

3.4.2 ALD Apparatus and Growth Conditions for Opal Infiltration

3.4.2.1 ALD Reactor

For studies of ZnO infiltration of opal templates, a custom-built ALD reactor described in [92] was used. The operating principles of such continuous-flow ALD systems are described in detail in Reference [100]. The equipment consists of an inert carrier gas (N_2) source, a hot-wall reaction chamber, a computer-controlled gas manifold, and a mechanical pump. Pressure was measured with a convectron gauge which was isolated from the rest of the chamber during runs to avoid film deposition on the gauge filament. The system had a base pressure of 10 mTorr and was run at pressures between 5 and 10 Torr. The chamber pressure was adjusted by partially closing the gate valve toward the mechanical pump.

Samples were mounted onto a Cu sample holder and placed in the chamber parallel to the gas flow to minimize turbulence. The chamber temperature was calibrated by mounting a thermocouple onto the same sample holder. To avoid melting or deformation of the PS templates the chamber temperature was kept at 85°C during runs. Precursor exposures, purges and the number of cycle were controlled by a personal computer via an automated gas manifold. The manifold consisted of a two carrier gas inlets, a chamber bypass line, pneumatic valves controlling the gas flow, and two liquid precursor sources. To avoid condensation of the precursors the manifold was heated to ~120°C. High-purity nitrogen was used to carry the precursors from the sources into the chamber. Figure 3.10 shows a schematic of the valve configuration and direction of gas flow during a water exposure: During the exposure, one high-vapor pressure precursor is leaked into the gas line and transported into the chamber by the carrier gas flow. At the same time the other precursor is purged from the system. The shaded

areas indicate the parts of the manifold where gas flow reverses direction during exposure to avoid mixing of the precursors in the chamber. Precursors were kept in glass flasks and could be heated to ensure a high enough vapor pressure.

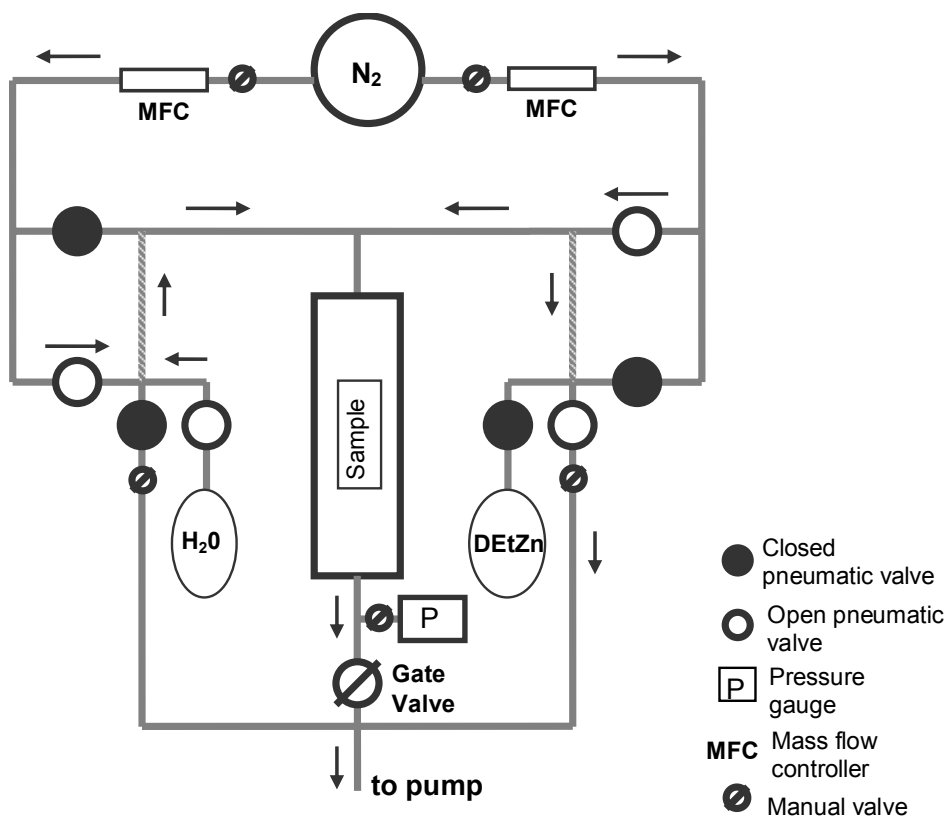


Figure 3.10: Schematic view of the ALD apparatus showing the direction of gas flow (indicated by arrows) during a water exposure.

3.4.2.2 Optimization of ALD Parameters

Experiments on ALD deposition of ZnO films on plastic substrates showed that relatively short exposure times of ~ 0.7 s were sufficient to saturate the surface reactions and reach steady growth rates [92] at a chamber pressure of 5 Torr. However, to achieve full infiltration of an opal structure the precursors have to be able to diffuse all the way into the narrow pore network. Our initial runs were based on parameters derived for thin film growth on plain substrates, and it was possible to infiltrate thin opal films (~ 10 layers). For thicker opal templates the infiltration resulted in a hollow structure with large internal voids (Figure 3.11). The ZnO film growth shows a definitive limit how far molecules could diffuse into the porosity during each pulse. Also, it is clear that the vertical cracks which form during the drying of the colloidal crystal serve as diffusion pathways down to the substrate, resulting in a shell structure.

To facilitate complete infiltration, the growth parameters were adjusted to allow full diffusion of the precursors into the pores of the opal structure. Simply increasing the precursor pulse time did improve the infiltration, but is not a practical solution because it results in a rapid depletion of the precursor reservoir. Therefore we also increased the chamber pressure from 5 to ~ 10 Torr to reduce the gas flow rate through the reactor and increase the dwell time of the precursor in the reaction chamber. This was combined with an increase in the DEtZn temperature to ensure that the vapor pressure is sufficiently high for proper dosing into the chamber. From the thickness of the ZnO film on the top layer of spheres we estimated a growth rate of ~ 0.14 nm/cycle for this process, similar to published data for this reactor [92]. To ensure full infiltration, the number of cycles per run was typically in excess of that theoretically needed (depending on the sphere diameter), which resulted in a “capping layer” of ZnO on top of the

samples typically ~50% thicker than the 0.0774*d* film thickness inside the crystal. (Comparing samples with and without this top layer, we did not observe any difference in optical behavior, though very thick layers have been observed to shift PBG reflection peaks [101].) The top layer was removed for SEM studies as described below.) Typical experimental conditions are summarized in Table 3.1.

Table 3.1: Typical operating parameters for ALD infiltration of polystyrene opals.

| | |
|----------------------------------|-----------|
| Pressure (purge) | 9-10 Torr |
| Peak pressure (exposure) Torr | 13 - 14 |
| Chamber temperature | 85°C |
| DEtZn: Precursor temperature | 38°C |
| Exposure time | 2 s |
| H2O: Precursor temperature | ambient |
| Exposure time | 5 s |
| Purge Time | 75 s |

3.4.3 Inversion of PS Template

After ALD infiltration, the structures were inverted by heating them in a furnace in air to burn off the polystyrene. A firing temperature of 400°C was sufficient to remove the PS after 3 hours. However, it was found that the samples exhibited lasing only after firing at a higher temperature. This is likely due to the sintering and grain growth of the initially amorphous ZnO,

as seen from X-ray diffraction data below. In order to ensure good optical quality, the structures were therefore inverted by firing at 550°C for 30min.

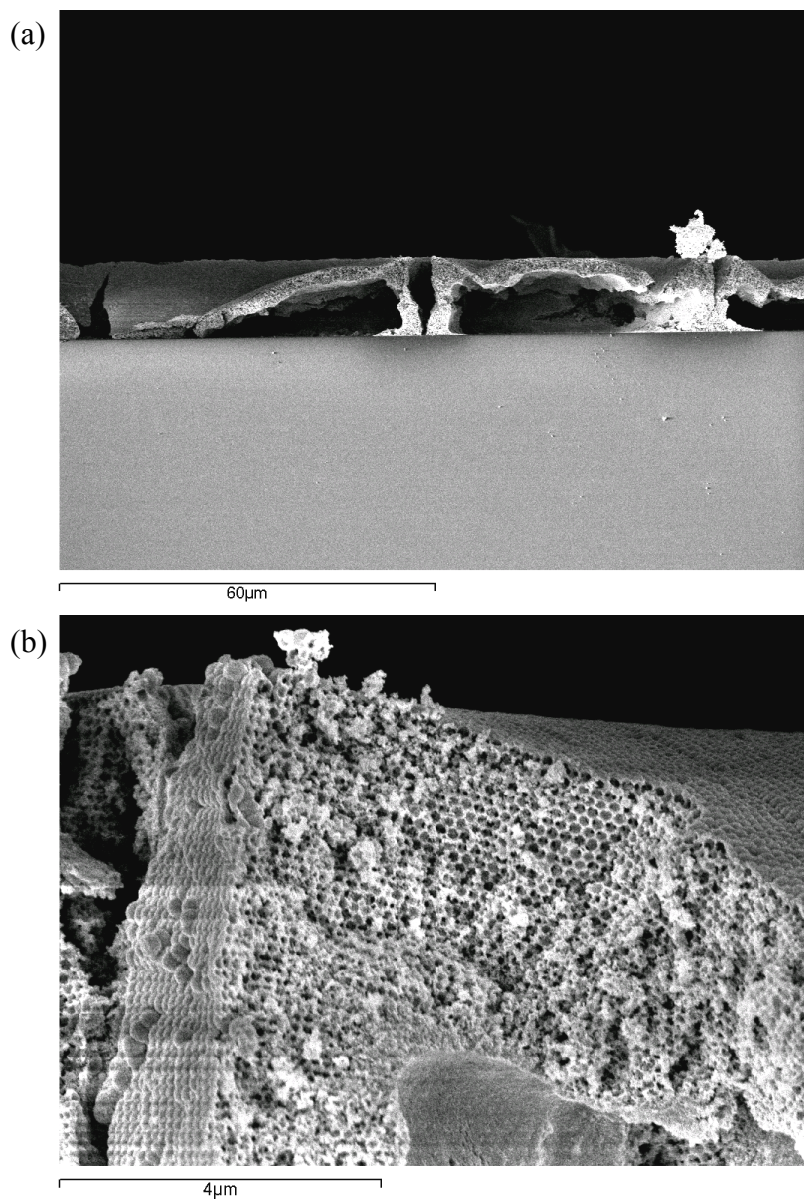


Figure 3.11: Cross-section of fired ZnO opal, $d=170\text{nm}$, at (a) low and (b) higher magnification. Insufficient pulse time led to incomplete infiltration.

3.4.4 Structural Characterization of ZnO Inverse Opals

Scanning electron microscopy (SEM) was used to characterize the ZnO infiltration, film roughness, and sample thicknesses. All SEM images were obtained using a Hitachi S-4500 FE-SEM microscope. When using small accelerating voltages (3-5kV) it was not necessary to coat the ZnO structures to prevent charging. To obtain cross-sectional images of the PhC structures, the samples had to be cleaved using a diamond scribe on the back of the substrate. This resulted in random fractures through the FCC structure, making it difficult to judge the degree of order in the PhC.

To image the inside of the PhC without introducing mechanical damage, the top layer of ZnO deposited by ALD was removed using reactive ion etching (RIE), using a Plasma Technology Plasmalab μ P system. RIE was performed in a CH_4/H_2 plasma at 300 W RF power and a pressure of 40 mTorr, followed by a cleaning step in oxygen plasma.

The (atomic) crystal structure of ZnO was evaluated by X-ray diffraction. θ - 2θ scans were taken using a Rigaku powder diffractometer. Due to the relatively low signal intensity from the inverse opals, scans were taken in the range of 30° to 40° , which covers the brightest reflection for ZnO, with 0.01° step size and 2s integration. The diffraction spectra were analyzed using the Jade 8 software package to evaluate the crystallite size, calculated from the FWHM of the diffraction peaks using the Scherrer equation.

3.4.5 Optical Characterization of ZnO PhCs

While structural characterization techniques give important information about infiltration and film growth, the determination of the photonic properties of the structures ultimately relies on optical characterization techniques. Transmission and reflection spectra of the PhCs were measured with a Cary 500 UV-vis-NIR spectrophotometer. In general, a white light source is passed through a monochromator to select a particular wavelength for observation. For transmission spectroscopy, the monochromatic source is split into two beams. One of these beams is passed through a reference sample, typically a blank substrate, while the other is passed through the sample. After passing through the samples, the two light beams are collected, and their intensities compared. The obtained value of the transmission (%T) corresponds to the ballistic transmission through the PhC along the [111] crystal direction.

Reflection spectra were obtained using the diffuse reflectance accessory (DRA) of the spectrophotometer. In this technique both the diffuse and the total (diffuse plus specular) reflection from the sample surface are measured using an integrating sphere in a two-beam setting. The specular component can then be calculated by subtracting the two measured spectra. The angle of incidence of the beam onto the sample surface is 3° , i.e. very close to the normal [111] direction.

3.5 Results of ALD Infiltration Studies

After the optimization of the process parameters the ALD was able to evenly infiltrate opal films even for large thicknesses and small sphere sizes. Figure 3.12 shows an example of a $d=256\text{nm}$ ZnO inverse opal with a thickness of more than 100 layers, which is more than sufficient for our optical experiments. (In thin PhCs finite size effects can become dominant. However, in strongly photonic PhCs the band gap is fully developed for thicknesses larger than ~ 15 layers. [102]) The samples used for optical studies typically had a thickness of ~ 50 layers.

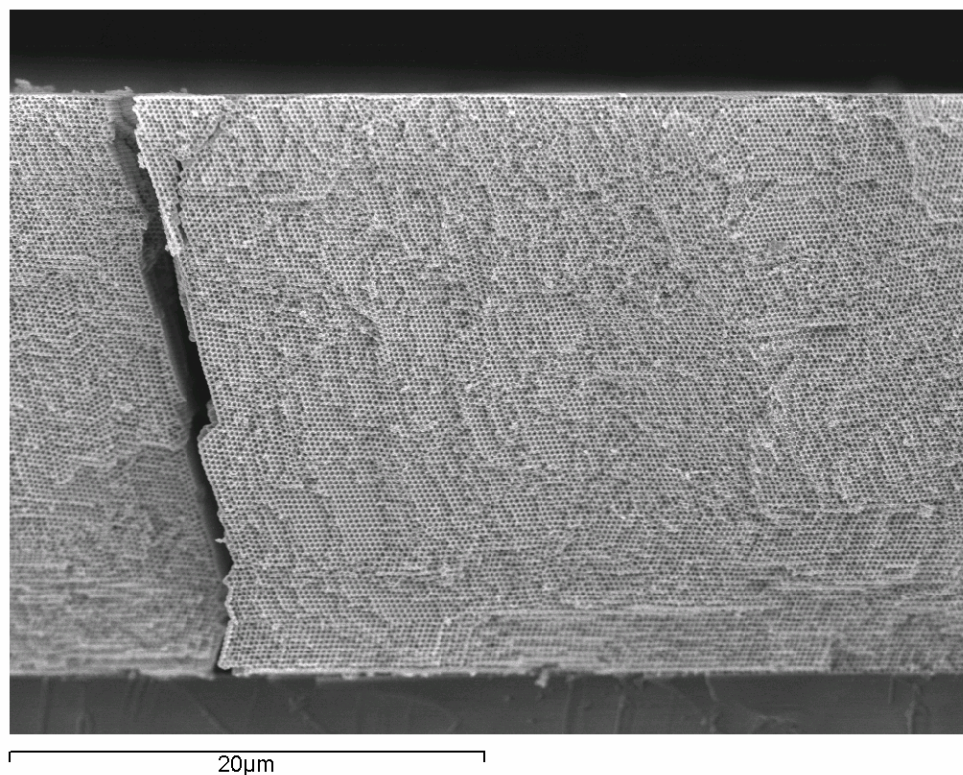


Figure 3.12: ZnO inverse opal with $d=256\text{nm}$ and a thickness >100 layers.

Shown in Figure 3.13 are SEM images of ZnO inverse opals with $d=256\text{nm}$ and 362nm , respectively, showing (111) surfaces exposed by RIE etching: The close-packed, triangular array of spheres in the (111) layer of the opal is inverted, leaving a ZnO scaffold with spherical voids. Each air sphere is connected to the layer below by three windows where the original PS spheres were touching.

The interstitial pores between the ZnO shells are still visible after firing (marked by square in Figure 3.13b). As discussed above, this porosity is predicted to increase the width of the band gap compared to an inverted opal structures without interstitial porosity [45]. Firing of the structure did not change the lattice constant significantly ($< 2\%$ shrinkage from SEM analysis), but does cause some sintering and grain growth of the ZnO. In fact, SEM and XRD analysis of the ZnO crystallite size shows that the as-grown ZnO film is smooth and amorphous (grain size $<10\text{nm}$), due to the low deposition temperature. During firing, the average grain size of a $d=256\text{nm}$ sample increased to only $\sim 15\text{nm}$ for 180min at 400°C , but to $\sim 40\text{nm}$ for 30min at 550°C .

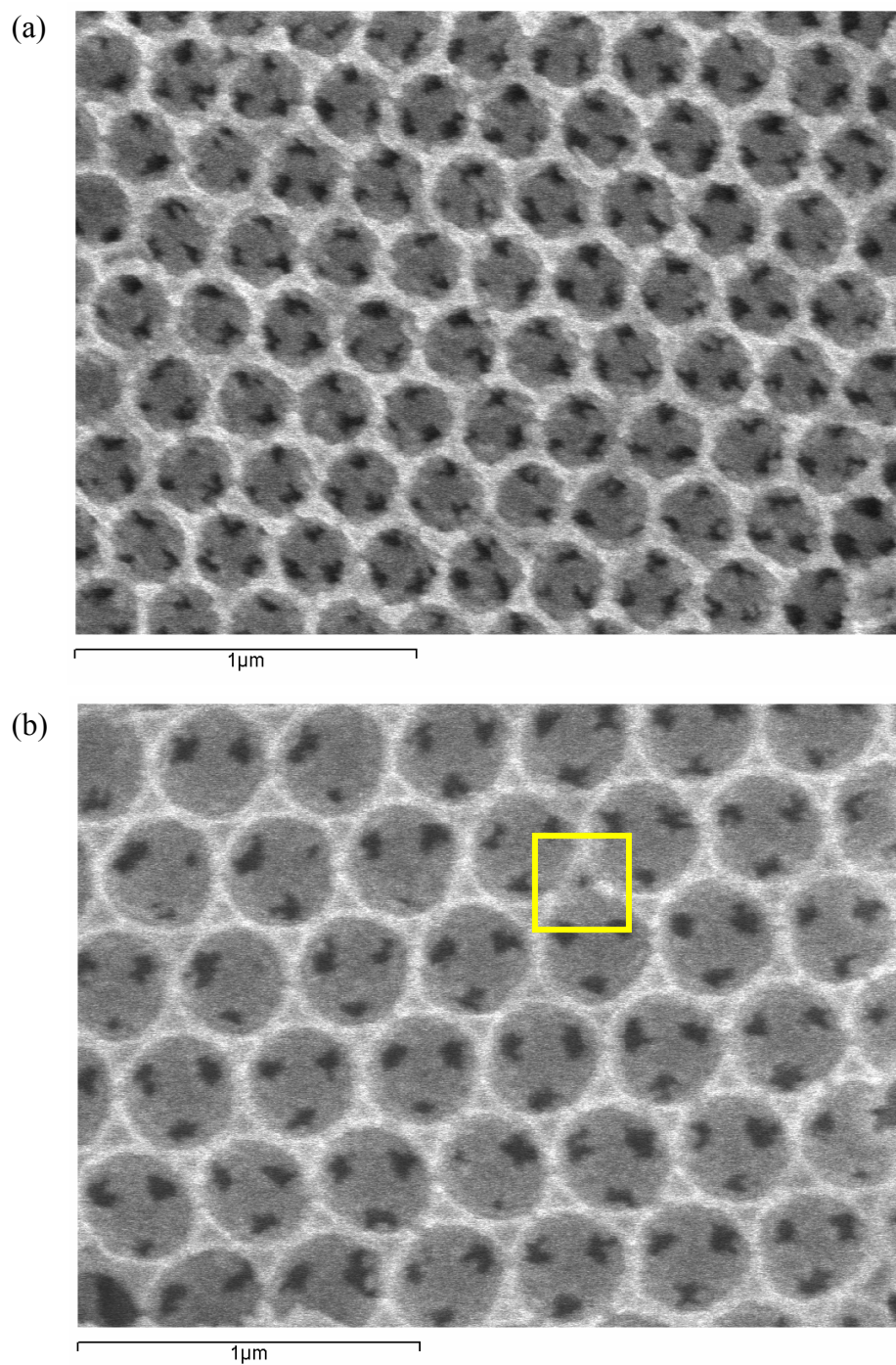


Figure 3.13: (111) planes of ZnO PhCs exposed by RIE, (a) $d=256\text{nm}$ (b) $d=362\text{nm}$. The yellow square marks exposed interstitial pore.

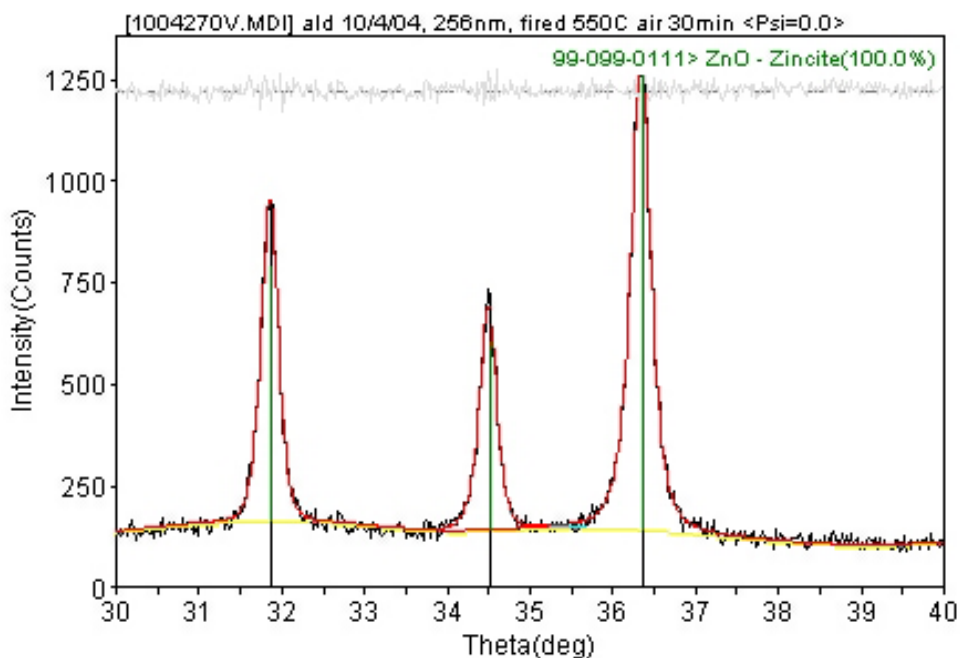


Figure 3.14: XRD scan for $d=256\text{nm}$ ZnO inv. opal fired at 550°C in air for 30min. The calculated background (yellow) and fitted peak profiles (red) are shown.

This grain growth introduces significant roughness on the ZnO shell surfaces and small-scale disorder in the structure. With decreasing lattice constants, disorder therefore becomes an increasingly important factor in the optical properties of these PhCs (see Chapter 4).

The ZnO films have uniform color over a centimeter-scale after firing, and optical transmission measurements taken at zero incident angle clearly show the existence of partial PBGs in the [111] direction (Figure 3.15). By varying the sphere size we can shift the band gap position to any wavelength in the visible light spectrum. For small spheres ($\leq 200\text{ nm}$) the short-wavelength band edge approaches the absorption edge of ZnO (at approximately 390 nm) and

the exact position of the PBG becomes difficult to determine by transmission. However, reflection spectra taken under normal incidence clearly reveal the existence of stop bands even very close to the absorption edge (insert of Figure 3.15).

Photoluminescence measurements show efficient emission of the ZnO inverse opals in the UV as well as a defect emission band at longer wavelength (Figure 3.16). For samples with band gaps overlapping the emission spectrum, we observed modification and suppression of emission due to the modified densities of photonic states, and a detailed investigation of the band structures and their influence on the PL and lasing properties of ZnO is the subject of the following chapters.

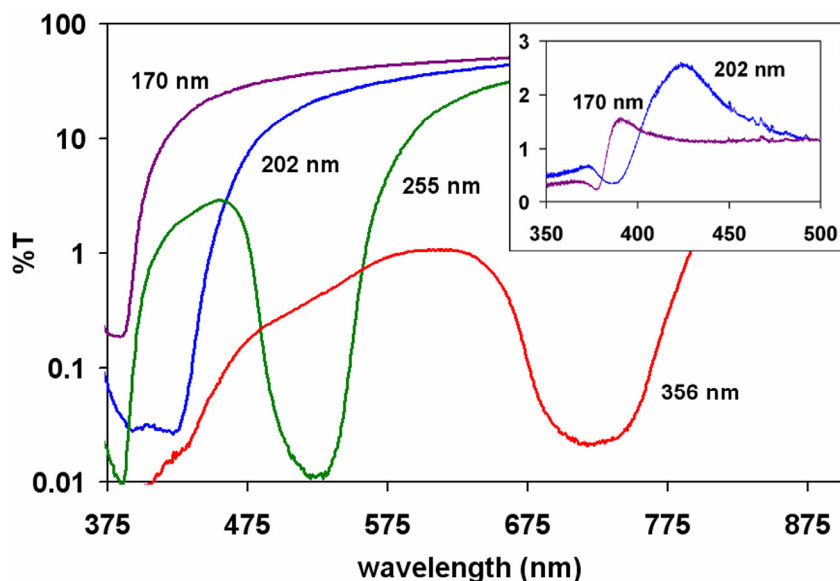


Figure 3.15: Transmission spectra of ZnO PhCs measured in the [111] direction. As the band gap shifts towards the absorption edge with decreasing sphere size, the band gap position becomes obscured. (The relatively low transmission of the 356 nm sample outside the band gap is due to its larger thickness.) Insert: Reflection peaks of the 170 nm and 202 nm structures at normal light incidence clearly show the existence of stop bands in the (111) direction near the absorption edge.

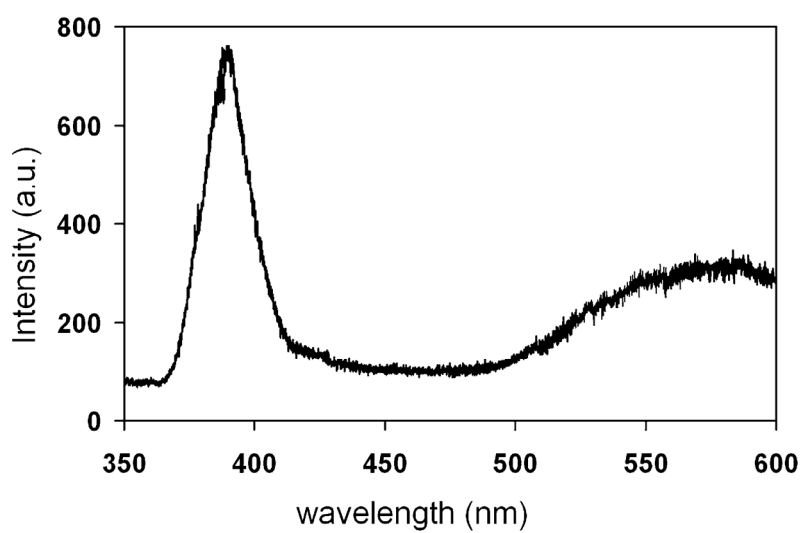


Figure 3.16: PL spectrum of ZnO inverse opal. This sample has no band gaps overlapping the emission spectrum.

4. UV Lasing with Reduced Threshold near the First Γ L-Pseudogap

4.1 Introduction

While inverse opal PhCs have been studied for years, the ZnO structures fabricated here are the first 3D PhCs reported which are inherently optically active, and therefore we were especially interested in their emission properties, especially their applications for PhC lasing. From a technological perspective, the development of compact ultraviolet UV light sources such as microlasers and highly efficient light-emitting diodes (LEDs) is very important for integrated optoelectronics, high-density optical storage, solid-state lighting, displays, sensors, and other photonic devices. Photonic crystals (PhCs) have great potential to control the functionality, improve performance, and facilitate miniaturization and integration of such devices. For example, using PhCs to make a low-threshold laser was one of the first applications envisioned after their conception [1, 8].

Amplification of light emitted inside the PhC can be enhanced in two ways: via modes with reduced group velocity (slow modes) that have frequencies located (usually) near a photonic band-edge [22, 103, 104], or by strongly localized defect states with eigenfrequency in the band gap [9]. Both approaches have been applied successfully to fabricate quasi two-

dimensional (2D) PhC lasers [105-108] operating in the near-infrared spectrum. Recent progress has been made in the development of 2D UV-emitting PhC devices based on GaN [109, 110] and ZnO [76]. These devices utilize the first-order PBG and, thus, require small feature size. Fabrication of such UV PhCs presents a considerable technological challenge.

Investigations of emission behavior in 3D PhCs have been limited to light in the visible spectrum from sources infiltrated into a passive dielectric structure. Gain enhancement has been observed from semiconductor quantum dots (QDs) in opal [111] and inverse opal PhCs [112], [113, 114]. Lasing has been observed in defect states in the primary gap of silica opals infiltrated with organic laser dyes [66, 115], and Cao et al. have demonstrated lasing in band edge modes of dye-infiltrated liquid crystal PhCs [116]. Infiltration of dyes or QDs reduces the refractive index contrast of the PhC and can lead to degradation of emitters due to interaction with the dielectric backbone material. In our samples ZnO acts as both the dielectric backbone and the gain medium for lasing. This allows us to study the emission properties without infiltrating quantum dots or dye molecules. The fraction of gain medium is also higher in our samples, and the different spatial distribution of emitters means that we are probing a different part of the LDOS in our experiments. However, we need to take into account the frequency-dependence of the refractive index and absorption in the PBG region in our active systems.

In this chapter we report experimental results on the UV lasing characteristics of the ZnO inverse opals near the first-order PPBG in the [111] direction. We observe a strong reduction in lasing threshold when the gap is tuned to overlap with the gain spectrum of ZnO. This suggests a combination of random lasing with partial PhC confinement.

4.2 Lasing in Disordered Photonic Crystals

The pursuit of light localization has led to two alternative approaches to realize mirrorless lasers: random lasers and photonic crystal (PhC) lasers. In a random laser, feedback is provided by strong scattering of light in a disordered medium. Random lasing has been observed in various disordered media [19]. However, the currently achievable thresholds are too high for practical applications because of incomplete confinement of light. One approach to improve the confinement is to maximize the scattering strength by using Mie resonances [117]. Another approach, first suggested by John [9], is to reduce the effective momentum of light by introducing periodicity into the system: Near a band edge of a PhC the Ioffe-Regel criterion for light localization is replaced by $k_c \cdot l \leq 1$, where the “crystal momentum” k_c is much smaller than the optical wavevector k . Theoretical studies of 2D systems have shown that very high quality modes can exist in disordered PhCs [118-120]. Due to the challenges in fabrication, real PhCs possess an unavoidable degree of disorder, and the optical properties of such partially ordered systems therefore are of great interest [121, 122].

High-quality ZnO inverse opals have been reported with the first PBG in the red and near-IR spectrum [79, 88]. However, the small sphere diameters (<200nm) necessary to tune the fundamental gap to the UV spectrum are difficult to grow with good monodispersity and to assemble into defect-free structures. In addition, we have seen in Chapter 3 that firing at elevated temperature causes sintering and grain growth of the nanocrystalline ZnO and thereby leads to small scale disorder in the structure, due to a roughening of the ZnO shell surfaces and

coarsening of the structure (Fig. 1b). (Samples fired at temperatures below 500°C did not exhibit lasing.) As a result, disorder becomes increasingly important with decreasing sphere size.

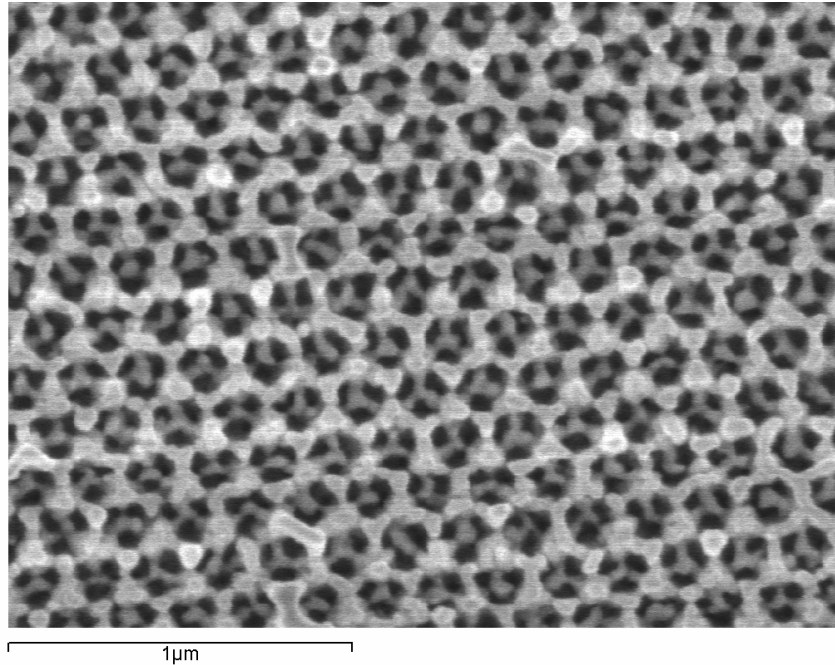


Figure 4.1: SEM image of exposed (111) surface of a ZnO inverse opal with $d=171\text{nm}$.

4.3 Experimental Procedures

4.3.1 Reflection, Transmission and the Photonic Band Structure

Transmission and reflection measurements were done as described in Chapter 3. The experimental transmission and reflection curves can be compared to photonic band structures to

determine parameters such as the filling fraction by numerical fitting. Band structures were calculated by the PWE method, using MIT's MPB software [12, 123]. To take into account the frequency-dispersion of the refractive index, the band structures were computed for a set of refractive indices n from 1.8 to 2.5 with 0.05 steps, and linear interpolation was used to obtain $\omega = \omega_{\mathbf{k},i}(n)$ where \mathbf{k} is the wave vector and i is band number. Knowledge of the ZnO refractive index $n(\omega)$ allows one to obtain $\omega = \omega_{\text{ZnO}}(n)$. By finding the intersection of these functions we determined $\omega_{\text{true}} = \omega_{\mathbf{k},i}(n_{\text{true}})$.

4.3.2 Emission Measurements

The optical set-up used to measure lasing and photoluminescence is shown in Figure 4.2. To measure the emission from the samples, the sample surfaces were first imaged by a white-light source and a 20X objective lens onto a CCD camera, and highly reflective areas free of cracks were selected for our experiments. The samples were then pumped by a continuous-wave He-Cd laser of $\lambda = 325\text{nm}$ in photoluminescence (PL) measurements, or at 10 Hz with 20ps pulses of wavelength $\lambda = 355\text{nm}$ from a mode-locked Nd:YAG laser in the lasing experiment. The beam had a spot diameter of approximately $20\mu\text{m}$ and was incident along the [111] crystal direction. The emission was collected by the objective lens (NA=0.4). All measurements were performed at room temperature.

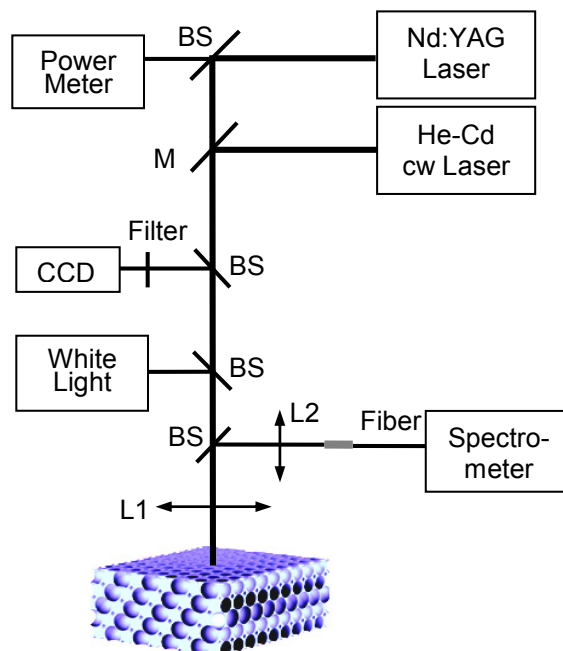


Figure 4.2: Schematic of the optical set-up used to measure lasing and photoluminescence from the ZnO inverse opal structures. The white light and pump beam are incident normal to the sample surface along the [111] direction, and the emission is collected in the same direction. BS stands for UV beam splitters, L1 is a 20X UV objective lens, M is a flip mirror to select the pump beams.

4.4 Results and Discussion

Figure 4.3 shows specular reflection spectra taken from four samples, with white light incident normal to the sample surface along the [111] crystal direction, and the calculated band structures of the PhCs. The largest sample ($d=256\text{nm}$) shows a reflection peak at $\lambda=525\text{nm}$, far from the ZnO absorption/emission edge, as well as the onset of higher-order reflection features between 390 and 400nm. (Our calculations confirm that these features are not due to a second PBG, which would be expected at higher frequencies, but are related to peaks in the reduced

density of states. Their origin and behavior are discussed in Chapter 6.) The narrow width and small amplitude of the reflection peak of the 171nm sample suggest that the gap is reduced by disorder and overlaps with the absorption edge of ZnO. This means that the observed reflection peak corresponds to the low-frequency part of the PBG and the high-frequency part of the gap is effectively destroyed due to absorption by ZnO. For the smallest sample ($d=160\text{nm}$) the first order PBG lies in the absorption region of ZnO and no PBG can be observed.

The results of photoluminescence measurements are shown in Figure 4.4. We observe broad spontaneous emission peaks from the ZnO PhCs. For comparison of spectral shape and peak positions, the emission spectra have been normalized to a peak value equal to 1. For the $d=171\text{nm}$ sample the PBG overlaps the emission band and the PL peak is clearly suppressed at the low-frequency edge and the maximum is blue-shifted. A similar modification of the spontaneous emission near the first PBG has been observed for light-sources infiltrated into PhC structures and can be explained by a redistribution of light emitted in directions prohibited by the PBG to other allowed directions [74].

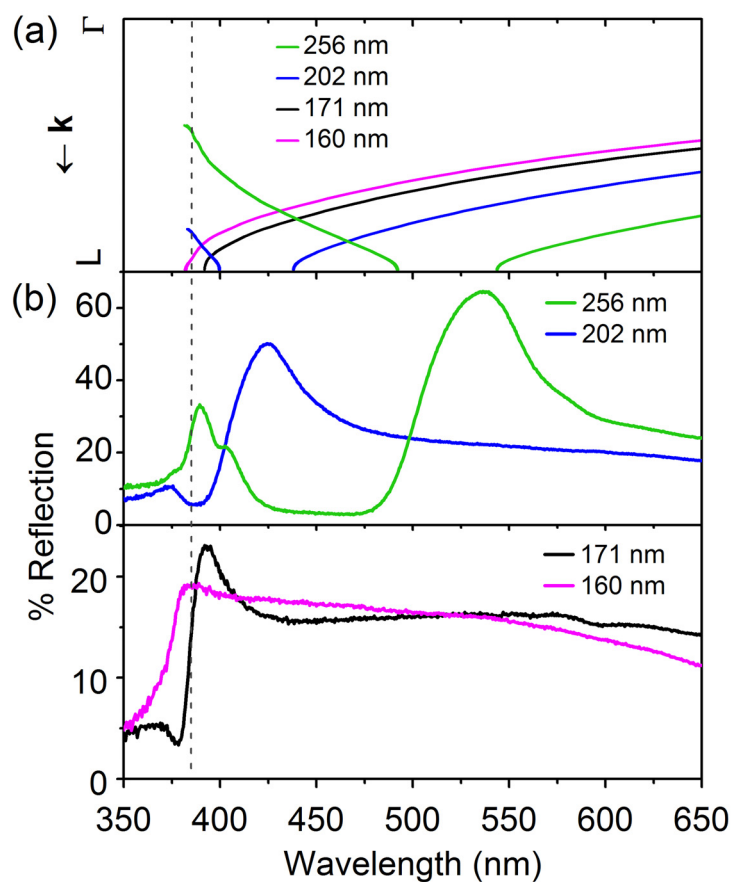


Figure 4.3: (a) Calculated photonic band structures of the ZnO inverse opals in the vicinity of the first ΓL pseudogap. The dashed line marks the approximate position of the ZnO absorption edge. With decreasing sphere size the fundamental PBG shifts closer to the absorption edge and the 160nm sample has no PBG due to absorption. (b) Specular reflection spectra of ZnO inverse opal PhCs with varying sphere diameters.

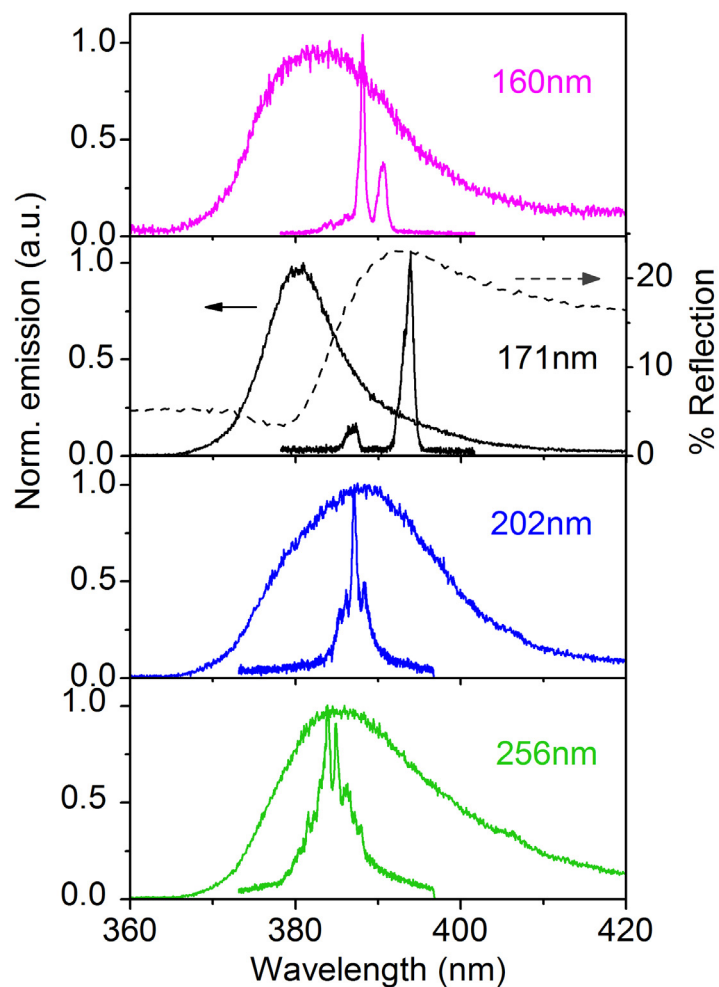


Figure 4.4: Photoluminescence and lasing spectra of the ZnO inverse opals with varying sphere diameters. The random lasing modes in the $d=160\text{nm}$, 202nm and 256nm samples overlap with the peak in PL spectrum. In the $d=171\text{nm}$ sample the PL is suppressed and blue-shifted by the PPBG (indicated by the reflection spectrum, dashed line). The main lasing modes are red-shifted into the PBG and do not overlap with the PL maximum.

With increasing pump intensity, scattering of light by disorder in the structure causes random lasing in samples with no PBG (d=160nm) or PBG away from the gain spectrum (d=256nm) (Figure 4.4). Similar random lasing behavior has been observed in ZnO powders [117, 124]. The random lasing modes overlap spectrally with the PL peaks and have output in many directions.

We have estimated the scattering mean free path of light l_s in our samples from transmission and reflection data:

$$\frac{T}{(1-R) \cdot T_{s \rightarrow g} \cdot T_{g \rightarrow a}} = \exp\left(-\frac{L}{l_s}\right) \quad (4.1)$$

The probe light is incident onto the sample/air interface, T and R are the measured values of ballistic transmission and total reflection (including specular and diffusive reflection), $T_{s \rightarrow g}$ and $T_{g \rightarrow a}$ are the transmission coefficients for the sample/glass and glass/air interfaces, and L is the sample thickness. A comparison for the values of l_s for different samples is only possible at wavelengths away from the ZnO absorption band and the PBGs. Thus we choose $\lambda=650\text{nm}$, and obtained values of l_s equal to $29.2\mu\text{m}$ for d=256nm, $21.5\mu\text{m}$ for d=202nm, 22.8nm for d=171nm, and 23.3nm for d=160nm. These results confirm that disorder slightly increases with decreasing lattice parameters, but also that the degree of disorder is similar for the three smaller sphere samples. Scattering will be significantly stronger at the ZnO emission wavelength, but should remain comparable in all samples.

Unlike the other samples, lasing peaks from the $d=171\text{nm}$ sample are spectrally located not at the position of strongest PL but are red-shifted into the PBG. As shown in Figure 4.5, the lasing threshold decreases dramatically when the PBG is tuned to the gain spectrum of ZnO. More specifically, the threshold is reduced by approximately a factor of 5 from $d=256\text{nm}$ to $d=171\text{nm}$ and a factor of 3 from $d=160\text{nm}$ to $d=171\text{nm}$.

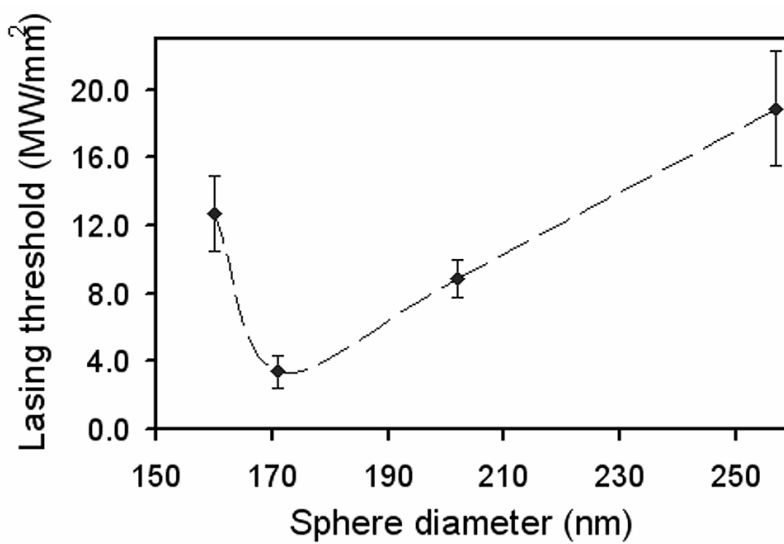


Figure 4.5: Lasing threshold versus sphere diameter for the ZnO inverse opals. The lasing threshold is strongly reduced when the PBG overlaps the emission spectrum of ZnO.

Because the difference in disorder between the samples is small and the optical quality is similar, this suggests that lasing is enhanced by the additional confinement of light provided by the PBG. However, despite the reduction of lasing threshold, the lasing output remains non-directional and similar to that of a random laser. Figure 4.6 compares the lasing spectra of the

$d=171\text{nm}$ and $d=202\text{nm}$ samples with increasing pump intensity, showing that despite the shift in wavelength lasing in the 171nm samples exhibits the same broad, multi-mode line shape as observed in random lasing. The inset of Figure 4.6 gives the integrated emission intensity versus pump power, showing a clear lasing threshold. The absence of directionality of laser emission excludes the possibility of lasing in the defect states within the $[111]$ PBG or band edge lasing in the high symmetry directions of PhC [66, 88, 116]. Random lasing modes with enhanced confinement in $[111]$ direction would be expected to emit more strongly in other directions outside the PBG. However, the partial gap in the 171nm sample is located near the absorption edge and covers only a narrow solid angle relative to directions outside the gap, so the angular redistribution of light is small. An alternative explanation in terms of directional lasing plus subsequent diffusion of laser emission appears unlikely since absorption of the pump light and lasing occur close to the sample surface. Based on these experimental findings, we believe that what we have observed is still random lasing, and that the spatial confinement of the random lasing modes is improved by the Bragg diffraction in the partial PBG. Further experimental and theoretical studies will be needed for a complete description of the complicated physical properties of such optically active, partially disordered photonic structures.

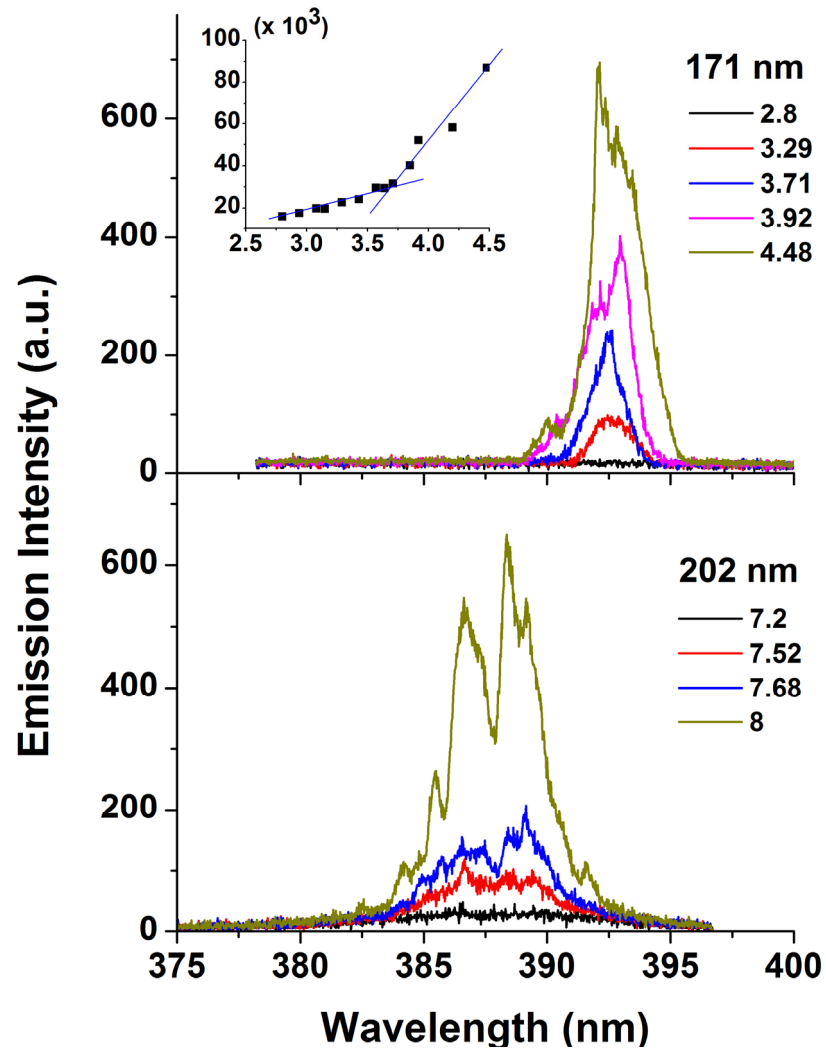


Figure 4.6: Lasing spectra for increasing pump intensities (in MW/mm^2) for $d=171\text{ nm}$ and $d=202\text{ nm}$ samples. (Inset: L-L curve for $d=171\text{ nm}$). Inset: L-L curve for the 171 nm spectra.

4.5 Summary

In conclusion, we have demonstrated UV lasing at room temperature from ZnO inverse opal PhCs. The disorder in the structures, primarily due to imperfections in the opal templates and roughness caused by grain growth during firing, induces optical scattering and leads to random lasing. When the first Γ -pseudogap of the PhCs is tuned to the ZnO gain spectrum, a pronounced reduction in lasing threshold is observed, indicating enhanced confinement of light by the incomplete PBG. We believe a fine tuning of the PBG position and a reduction in disorder by improving the sample fabrication will lead to photonic crystal lasing and a further reduction of lasing thresholds and improvement of the output directionality.

5. Lasing in High-Order Bands of 3D ZnO Photonic Crystals

5.1 Introduction

The results presented in Chapter 4 demonstrate that disorder becomes a critical factor when trying to achieve photonic crystal lasing near the primary PBG of ZnO PhCs due to the very small feature sizes necessary. One approach to this problem would be improving the fabrication process to reduce the amount of structural disorder. Given the limitations of the monodispersity of colloidal particles with $d < 200\text{nm}$, the inherent disorder of the self-assembly process, and the grain growth of ZnO during firing, this is no small technological challenge. Another strategy is to utilize the high-order photonic bands of the PhCs to confine light in the material. For a given emission wavelength we can then use structures with much larger feature sizes than those necessary for first-order Bragg diffraction. This is especially significant for the fabrication of UV devices.

Physically, the optical effects of the high-order bands are more complicated, as shorter waves experience simultaneous Bragg diffraction from multiple sets of lattice planes and coupling of many Bloch modes occurs [125]. As a result, the band gaps become less anisotropic and an omnidirectional PBG is expected for inverse opals with a refractive index contrast ~ 2.8 or

larger [44]. Even without a complete PBG, stimulated emission is strongly enhanced in weakly dispersive (“flat”) higher bands [22], because the group velocity is reduced over an extended region of k-space (group velocity anomaly). Sakoda has shown that the lasing threshold in flat bands of 2D PhCs can be order of magnitude smaller than at the primary band edge [2, 22]. High-order bands can also provide the necessary conditions to efficiently couple light in and out of PhC structures [126]. Experimentally, high-frequency reflection and transmission spectra of 3D opal [127, 128] and inverse opal structures [102, 129, 130] have been studied. However, many of the observed features are not yet fully understood: The analysis of these data is complicated because spectral features (such as peaks in reflection) can be caused by gaps (i.e. a depletion of the DOS), flat bands (i.e. a peak in the DOS associated with an increase in the effective refractive index of the material), anti-crossings of bands etc. At the same time, the accuracy of calculated band structures is limited in the high-frequency spectral range.

Limited information is available on the effect of the high-order band structure on the emission properties of 3D PhCs [131]. Bechger et al. have studied the fluorescence of laser dyes in 3D PhCs and observed modified emission due to higher-order Bragg diffraction in polystyrene opals, despite the fact that such polystyrene structures do not even have a directional high-order gap in the Γ -L direction. This underscores the potential of high-order diffraction effects to modify the emission from PhCs, especially for photonic structures with a strong refractive index contrast. Our results demonstrate that the high-order band structure of 3D PhCs can be used to efficiently confine light and enhance light amplification.

5.2 Experimental Procedures

The procedures for fabrication and optical characterization used in this part of the research are the same as described above. In addition, to obtain images of the lasing modes samples were cleaved and then pumped and imaged from the side as shown in Figure 5.1. The samples are rotated 90° and imaged and pumped from the side (cleaved edge). The samples are now pumped perpendicular to the [111] direction, and the gain region is spread throughout the sample thickness. By switching the fiber position between side and top detection (positions A and B in Figure 5.1) we verify that lasing still occurs in the [111] direction perpendicular to the substrate surface. Laser emission which is scattered by the surface roughness of the cleaved edge is used to obtain mode images, while the pump light is filtered out before reaching the CCD camera.

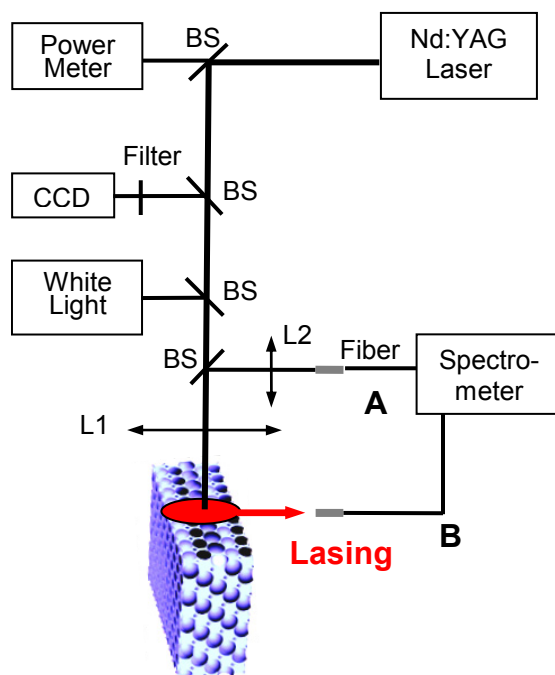


Figure 5.1: Schematic of the modified optical set-up used to obtain mode images.

5.3 Optical Properties in the High-Order Band Structure

5.3.1 Reflection Spectroscopy

To study the effect of the high-order band gaps we used spheres with diameters ranging from $d=330\text{nm}$ to 383nm . A typical image of one of the samples is shown in Figure 3.13b. Reflection spectra of light incident along the [111] direction (Figure 5.2) show the resulting first-order Bragg peaks at wavelengths from 655 nm to 765 nm (peak R1). We also observe two strong reflection peaks (R2 and R3) and several fine features at wavelengths approaching the ZnO absorption edge. Because the refractive index increases sharply for frequencies near resonance, high-order band gaps become more pronounced and the reflection peaks blue-shift more slowly with decreasing PhC lattice constant (i.e. sphere diameter) than the first-order Bragg peaks (Figure 5.3).

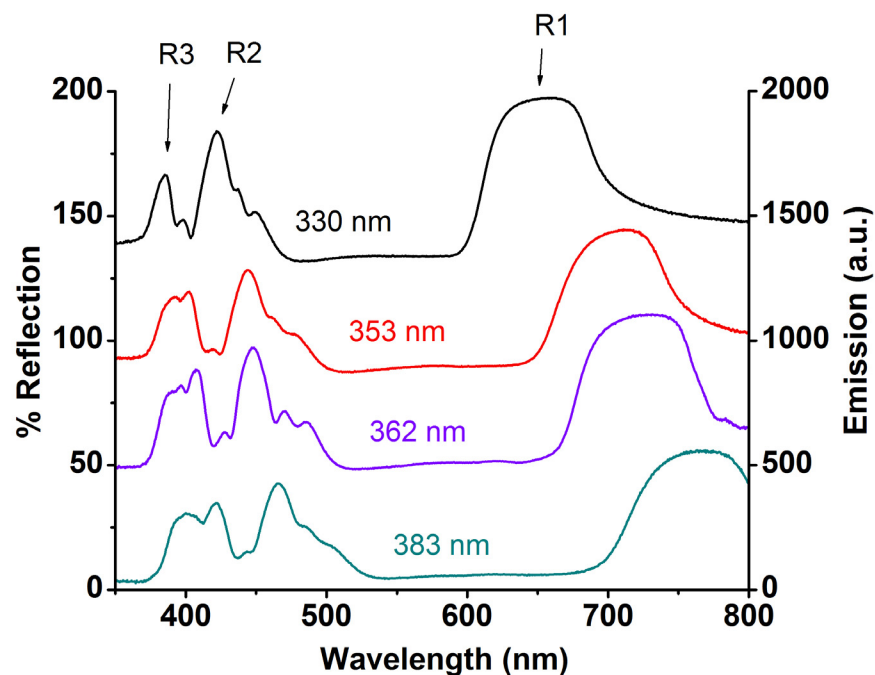


Figure 5.2: Reflection spectra of ZnO PhCs for four different sphere diameters. Light is incident along the [111] direction normal to the PhC surface. The first-order Bragg peak (peak R1) and two main reflection peaks at shorter wavelengths (R2 and R3) are detected.

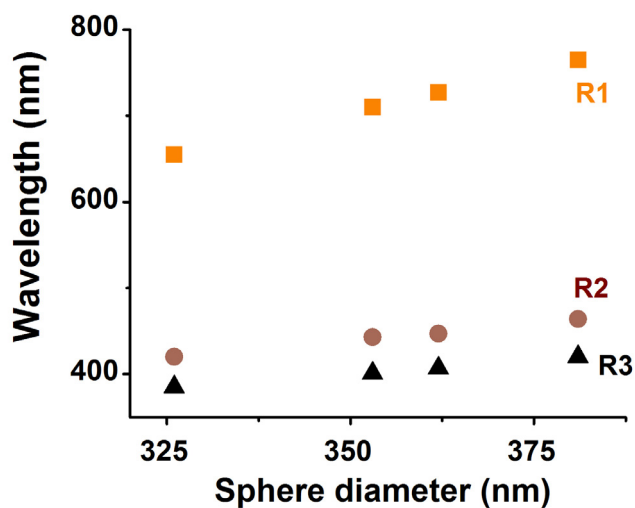


Figure 5.3: Position of the reflection peaks versus sphere diameter d . As the wavelength approaches the absorption edge of ZnO (at $\lambda \approx 380$ nm), the refractive index increases sharply and slows down the blue-shift of the peaks.

5.3.2 Results of Emission Measurements

At low pump level the emission spectra of all the samples feature a broad spontaneous emission peak with a maximum at $\lambda \approx 390$ nm. With increasing pump intensity a single lasing peak appears (marked L in Fig. 1), with λ at the short-wavelength edge of the third reflection peak. The lasing peak initially has a width of 0.6 to 1.0 nm, but becomes narrower with increasing pump intensity, reaching a full-width at half-maximum of 0.1 to 0.3 nm (Figure 5.5a). The peak positions blue-shift slightly with increasing pump power. The emission increases rapidly and shows a pronounced threshold behavior (L-L curve shown in Figure 5.5a inset for the $d=362$ nm sample).

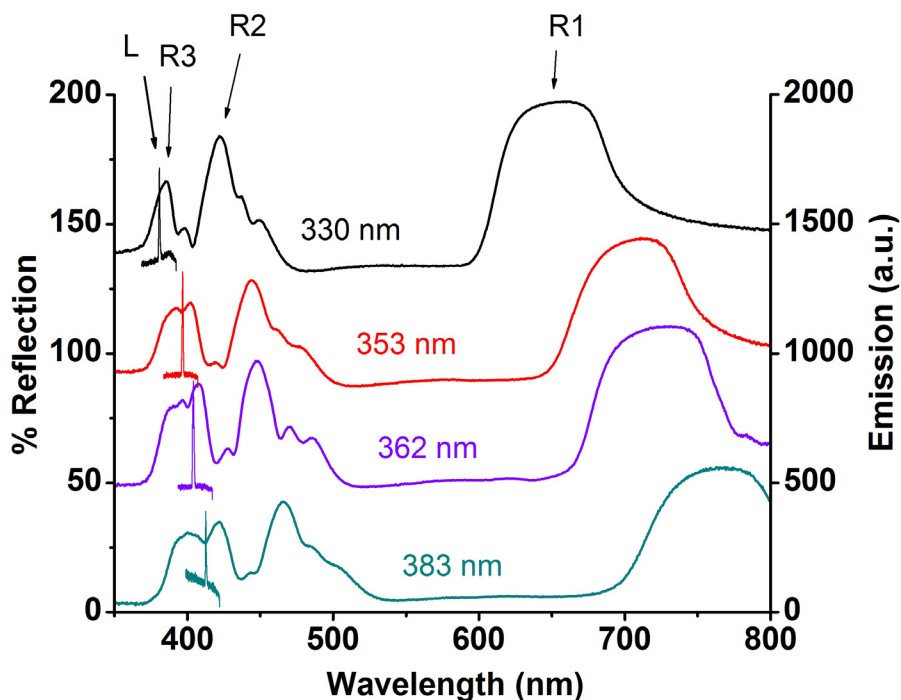


Figure 5.4: Lasing peaks (L) plotted along with reflection spectra (same as Figure 5.2). Lasing occurs at the high-frequency shoulder of the third main reflection peak (R3) in all samples.

Angular distribution of lasing emission is shown in Figure Figure 5.5b. 0° corresponds to the [111] direction normal to the sample surface. Lasing output is highly directional, with a divergence angle of approximately 6° . The directionality is preserved if the pump light is incident at an angle slightly off the surface normal. This indicates that lasing is strongly confined in the [111] direction. Changing the PhC lattice constant leads to a shift in lasing wavelength λ_{las} , from $\lambda_{\text{las}} \approx 383$ nm for $d=330$ nm to $\lambda_{\text{las}} \approx 415$ nm for $d=383$ nm (Figure 5.5c), closely matching the shift in the high-order band structure. The gain spectrum of ZnO is centered at ~ 390 nm. Accordingly, the threshold increases with growing distance of λ_{las} from the gain maximum, e.g. by a factor of 30 from $\lambda_{\text{las}} \approx 383$ nm ($d=330$ nm) to $\lambda_{\text{las}} \approx 415$ nm ($d=383$ nm). The fact that lasing occurs at frequencies so far from the gain maximum reveals that the confinement effect of the high-order band structure is remarkably strong in these PhCs. Well above threshold, secondary lasing peaks may appear within a wavelength range of approximately ± 3 nm from the main peak. The exact origin of these peaks is unclear at this time, but our measurements indicate that they are more isotropic and might be caused by defects or lasing in other crystal directions. However, the directional nature of the primary lasing mode, the reproducibility and stability of λ_{las} , and its dependence on the PhC lattice constant suggest that the primary lasing is related to the photonic band structure.

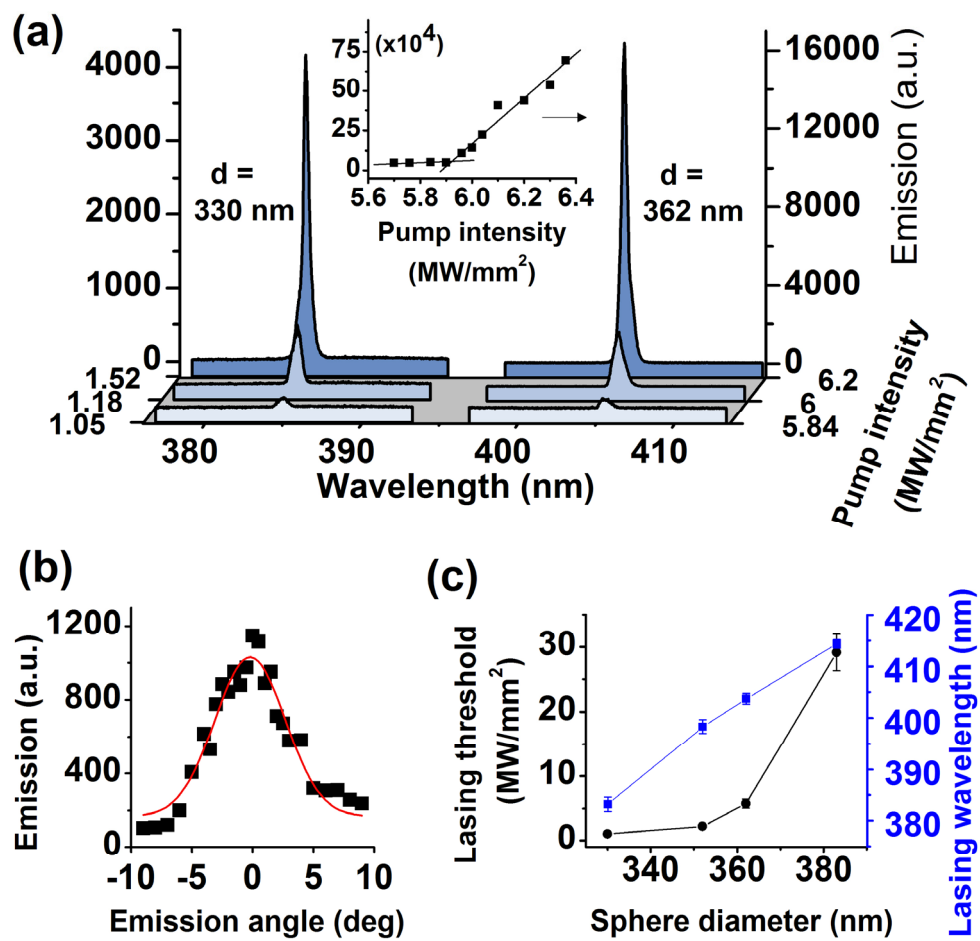


Figure 5.5: (a) Emission spectra of ZnO PhCs with $d = 330\text{ nm}$ and 362 nm for increasing pump intensity. Inset: L-L curve for the 362 nm sample (with a clear threshold at $\sim 5.9\text{ MW}/\text{mm}^2$). (b) Angular distribution of lasing emission. (Squares represent measured data, the line is a guide for the eye.) (c) Lasing threshold and wavelength versus sphere diameter.

5.3.3 Comparison to Band Structure Calculations

To understand our experimental results, we correlate them to the photonic band structure. Fig. 3a shows the reflection spectrum of the 362 nm PhC along with lasing and spontaneous emission spectra. The reflection peak at 407 nm coincides with a clear dip in the spontaneous emission spectrum, confirming the existence of a stop band. We have calculated [12] the band structure of the inverse opals with interstitial porosity taking into consideration the frequency dependence of the refractive index of ZnO [132]. The calculations were performed for wavelengths longer than 380 nm. We have not accounted for absorption of light, which becomes a dominant effect for shorter wavelengths. The only adjustable parameter used in the calculations was the sphere diameter d . Fig. 3b depicts the calculated band structure for wave vectors along the Γ -L $\langle 111 \rangle$ direction for $d=355$ nm. Three directional band gaps match up closely with the most prominent reflection maxima in the experimental data (Fig. 3a). This correspondence was used as the criterion for determining the fitting parameter d (which is within the margin of uncertainty of sphere diameter, lattice constant after firing, and small variations in filling fraction and topology). The theoretical results can also explain some of the weaker features in the reflection data in terms of band singularities in either Γ or L k -directions.

At the high-frequency edge of the third PBG there is an isolated degenerate band (band number nine) with extraordinarily low dispersion which coincides with the lasing wavelength for all our samples. Fig. 3c plots the calculated group velocity. The ninth band has little overlap with other bands and has a group velocity v_g less than $0.09c$. Light amplification in this band is strongly enhanced due to the extremely low v_g over the whole Γ -L range. This suggests that lasing occurs due to distributed feedback of slow propagating modes in this band. It is worth

noting that this flat band is a feature of the inverse opal structure with interstitial porosity and that the corresponding band in a fully filled inverse opal structure shows considerably more curvature. The increase of the refractive index in the vicinity of the electronic band edge leads to additional flattening of the band. Our calculations show that 25 – 32 % of the energy of a mode in this band is concentrated in the dielectric structure and thus can be efficiently amplified by the gain material.

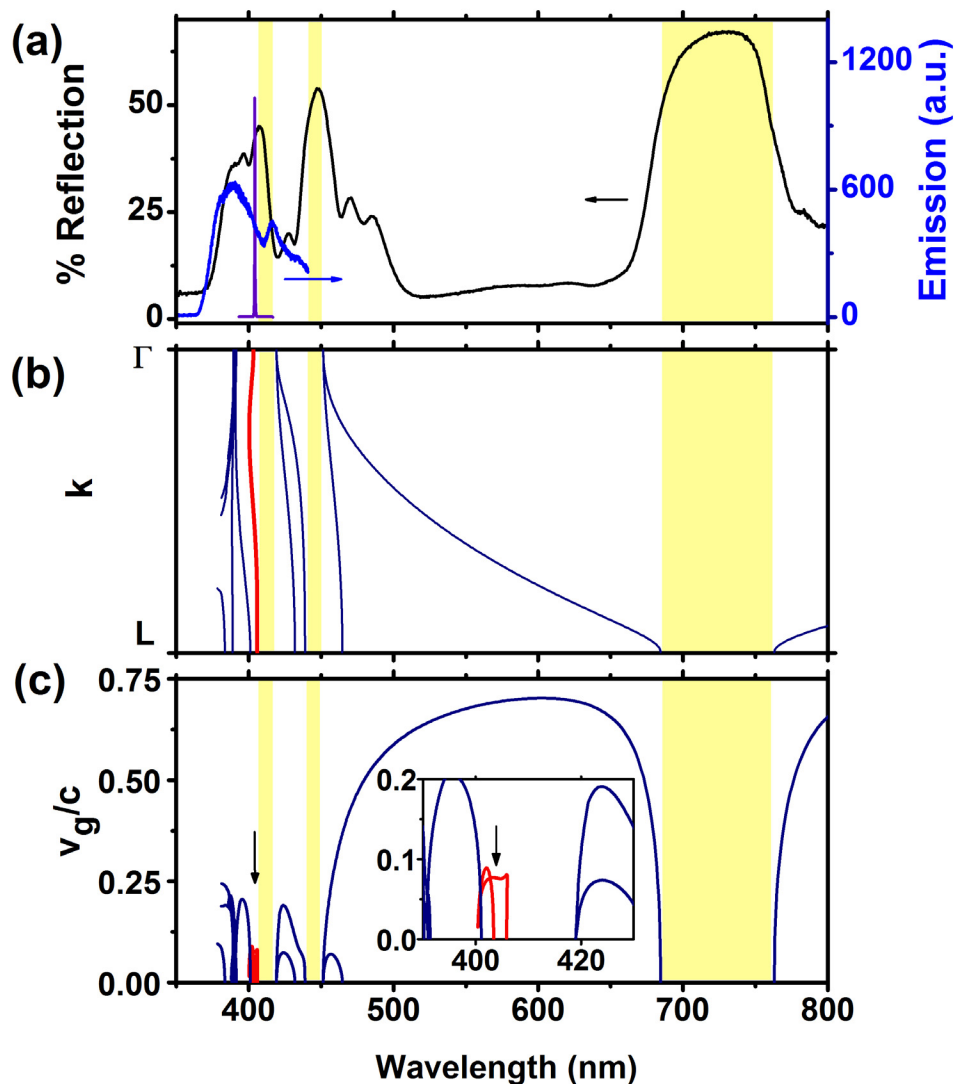


Figure 5.6: (a) Reflection (black), photoluminescence (blue) and lasing (violet) spectra of a PhC with $d=362$ nm. Lasing occurs at the high-frequency shoulder of the reflection peak at 407 nm.

The photoluminescence exhibits a minimum in this region, confirming the existence of a stop band. (b) Calculated band structure of ZnO inverse opals with $d=355$ nm in the Γ -L direction. The lasing peak coincides with the isolated flat band (red) at the high-frequency edge of the third gap. The shaded yellow areas indicate the calculated band gaps. (c) Calculated group velocities. Light in the weakly dispersive band (red) has a very low v_g over the whole Γ -L range.

5.3.4 Lasing Mode Imaging

To experimentally verify that the observed lasing is based on distributed feedback in spatially extended slow-light modes rather than localized defect modes, we attempted to image the lasing modes directly. Figure 5.7 shows a white-light image of the inverse opal cross-section as well as the image of the lasing mode obtained when pumping this position. The PL background was recorded separately (just below threshold) and subtracted from the image. Because the image of the mode is obtained by detecting scattered light, the results of this experiment are not fully conclusive because the strength of scattering does of course depend on the disorder in the sample as well. Nevertheless, the mode does appear extended throughout almost the whole thickness of the inverse opal film and not localized due to disorder. In fact, based on the 1D radius of gyration ξ (along the [111] direction) defined by

$$\xi^2 \equiv \frac{\int dL r^2 I(r)^2}{\int dL I(r)^2} - \left(\frac{\int dL r I(r)^2}{\int dL I(r)^2} \right)^2 \quad (5.1)$$

(where L is the PhC thickness, r is position variable, and I(r) is the measured intensity), we estimated the localization diameter of the mode as approximately half the film thickness.

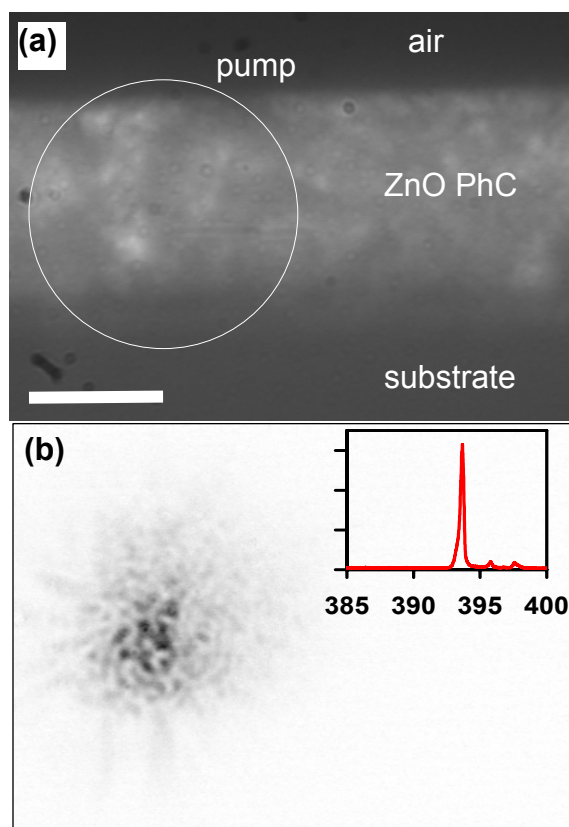


Figure 5.7: Mode Imaging. (a) White-light image of the ZnO inverse opal cross-section (cleaved edge). Scale bar represents $10\ \mu\text{m}$. The circle indicates the approximate size and position of the pump spot. (b) Lasing mode image (inverted contrast) and the corresponding lasing spectrum (inset, x-axis shows wavelength, y-axis shows emission intensity in a.u.).

5.4 Conclusion

In summary, we have demonstrated UV lasing in 3D ZnO PhCs at room temperature. Even without a full PBG high-order bands can efficiently confine light in the material and lead to robust and directional lasing. The flat band that we believe is responsible for lasing in our structures lies at the high-frequency edge of the third gap in the [111] direction (between the 8th and 9th band), where the complete PBG will develop for materials with higher refractive index. Therefore a further decrease in lasing threshold should be possible in systems with higher refractive index contrast or optimized topology [89]. Our results also imply that the high-order photonic band structure of inverse opals can be exploited for photonic applications such as highly-efficient LEDs or non-linear optical processes.

6. Angle- and Polarization-Dependent Reflection and Spontaneous Emission Properties

6.1 Introduction

The discovery of lasing in the high-energy band structure of ZnO PhCs demonstrated how even in the absence of a complete PBG the abnormal dispersion behavior of PhC can be used to control the interaction of light with a material. Questions remain, however, about the evolution of these bands and their effect on the emission properties of the optically active PhCs. While numerous reports have dealt with the emission properties of opal-based PhCs near the lowest-order gap [67, 74, 112, 114, 133-139], not much information is available on emission effects in the higher-order band structure [131], and even transmission and reflection properties are not fully understood in this spectral range [102, 127-130]. Spectral features observed in the optical measurements can be related to PBGs or the excitation of photonic modes and often cannot be unambiguously identified. This is mainly due to two factors: (i) The numerical methods become less reliable at high frequencies due to convergence problems, because the approximations made in these methods become less accurate, and because the high-order band structure is very

sensitive to the topology of the system. (ii) The interpretation of experimental data is often complicated by the interplay of diffraction, random scattering, effects of mode symmetry etc.

Motivated by the lasing results presented above we conducted an investigation of the angle- and polarization resolved properties of our samples to find out how the high-order gaps and flat bands behave and how they influence the spontaneous emission. The results reported here show significant spectral and angular resolution of emission due to the modification of the directional DOS at flat band edges. The reflection and emission features are related to calculated band structures. The observed differences between polarizations in both calculated and experimental data are explained in terms of multiple Bragg wave coupling.

6.2 Emission Modification in Photonic Crystals

Both directional and complete gaps in the band structure of PhCs are, in theory, accompanied by a spectral redistribution of the photonic DOS. Because the emission rate of an atom or molecule is determined by the density of electromagnetic modes at its position (Purcell effect), this will have an effect on the radiative rate of emitters [8, 68, 74]. However, such lifetime effects will only be observable if the spectral width of the emission is narrow enough to overlap completely with the PBG. Furthermore, because the radiative rate and the LDOS are angle-integrated properties, they will not be significantly affected by directional stop gaps and cannot explain angle-dependent changes in the emission spectra [139]. However, the highly anisotropic propagation behavior of photons inside PhCs can lead to frequency- and direction-dependent modification of radiation. The observed effects depend on the particular system and

include simple suppression of emission at the PBG position [137, 140-142], enhancement of emission at the band edges [131], diffusion and redistribution of light in disordered PhCs [143], and amplification of spontaneous emission [111, 112]. Bechger et al. have studied the fluorescence of laser dyes in 3D PhCs and observed modified emission due to higher-order Bragg diffraction in polystyrene opals, despite the fact that such polystyrene structures do not even have a directional stop band in the Γ -L direction. These findings underscore the potential of high-order diffraction effects to modify the spontaneous emission from PhCs, but also demonstrate the need for further experimental studies especially in systems with a higher refractive index contrast. The ZnO inverse opals used in this study are not only strongly photonic; they also allow us to probe a different part of the LDOS because the spatial distribution of emitters differs from the case of infiltrated light sources.

6.3 Experimental Procedures

6.3.1 ZnO PhCs Samples

The samples used in this study were ZnO inverse opals fabricated by ALD infiltration of PS opal templates with a sphere diameter of $d=400\text{nm}$ (lattice constant $a=562\text{nm}$), as described above. Figure 6.1 shows a specular reflection spectrum measured at normal incidence in the [111] direction.

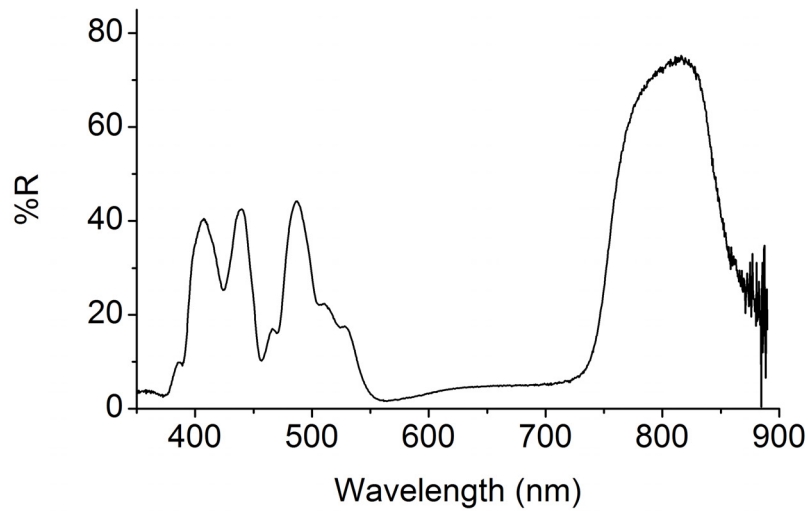


Figure 6.1: Specular reflection of $d=400\text{nm}$ ZnO inv. opal along $[111]$ direction.

The center wavelength of the first Bragg peak is $\lambda=804\text{nm}$, and three major higher order peaks can be seen at $\lambda=486\text{nm}$, 438nm , and 406nm . Three less intense features are located at $\lambda=528\text{nm}$, 511nm , and 466nm .

As a reference sample for photoluminescence, we also fabricated a non-photonic random sample. To achieve a comparable emission spectrum, we mixed $d=400\text{nm}$ spheres with a small amount of other sphere sizes and grew a thin film using the vertical deposition method described above. This randomly packed layer was subsequently infiltrated by ALD and inverted using the same procedures as for inverse opal fabrication. The lack of monodispersity (the coefficient of variation of diameters in the mixed suspension was approximately 10%) prevented the formation of ordered crystal domains and of a PBG, but ensured a similar microstructure and material properties.

6.3.2 Optical Measurements

The experimental set-ups for angle-dependent reflection and photoluminescence measurements are shown in Figure 6.2. The samples were mounted on a goniometer stage. Reflection scans were performed in a θ - 2θ geometry for angles $\theta=5^\circ - 60^\circ$. White light from a mercury lamp was collimated (using a pin hole and lens) and then focused onto the sample by a long-focus length (L1). The reflected light was focused by lens L2 into a fiber detector and photospectrometer. The polarization state of the reflection was determined by a linear polarizer in front of the detector for 0° (p-polarization) and 90° (s-polarization). Scans were taken every 5° with an angular resolution of the set-up of $\sim 5^\circ$.

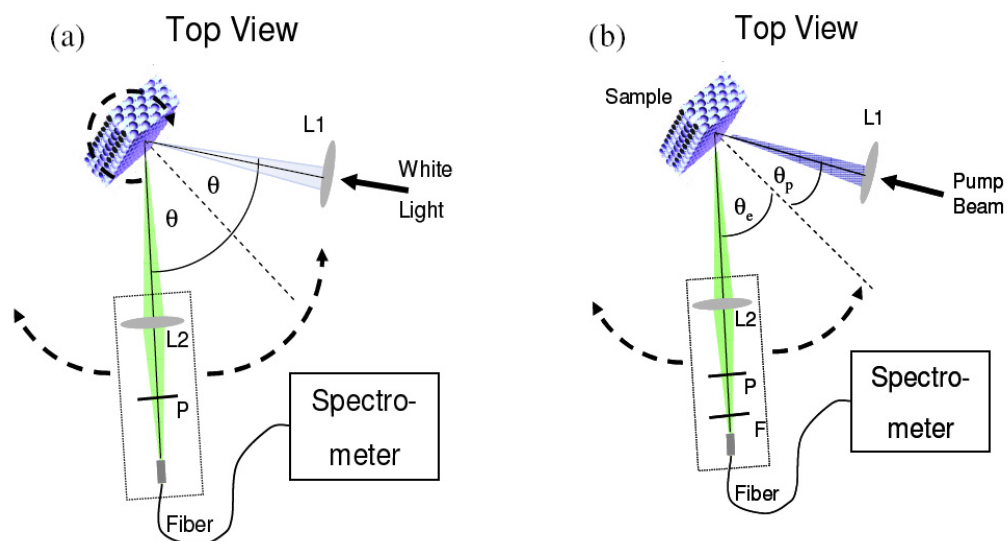


Figure 6.2: (a) Optical set-up for θ - 2θ reflection scans. (b) Set-up for PL measurements.

In order to observe the dispersion of band structure features over a wide spectral range, we concentrated on the broad ZnO defect emission peak in this study. The samples were pumped with $\lambda=325\text{nm}$ light from a cw He-Cd laser. The pump angle θ_p was kept constant (approximately -15°) and the detector arm was rotated from $\theta_e=0^\circ$ to 60° . Spectra were acquired every 10° with angular resolution of $\sim 5^\circ$. The pump light was filtered out before reaching the fiber detector. In order to avoid artifacts stemming from different detection efficiencies for changing angles and polarizations, reference spectra were taken from the random sample at each angle and polarization and used for the normalization. No difference between p- and s-polarized light was found in the reference spectra.

In both experiments, the samples were oriented so that incident and diffracted wavevectors (as well as the surface normal) were contained in the Γ - L - U - X plane of the FCC BZ (see Figure 6.3). Rotational alignment was simplified by the diffraction pattern visible on the sample surface for a beam transmitted through the sample.

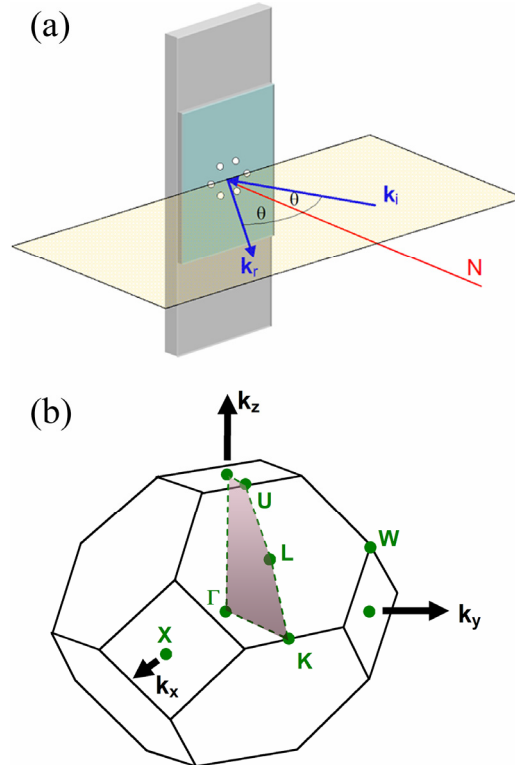


Figure 6.3: (a) Orientation of the samples during optical measurements. The growth direction is indicated by the black arrow. N (red) is the surface normal. The samples were aligned using the diffraction pattern on the surface. (b) The FCC BZ showing the Γ - L - U - X diffraction plane.

6.3.3 Band Structure Calculations

PWE calculations [12] incorporating the frequency-dependence of the refractive index were used (as described above) to calculate the band structure of the $d=400\text{nm}$ PhCs, shown in Figure 6.4 [144]. Based on the full band structure we then calculated cuts through the dispersion surface of the PhCs in the Γ - L - U - X plane. To analyze the angular reflection and emission results, the band structures were calculated along given propagation directions using kinetic matching conditions [15, 145]: The momentum of an incident photon can be described by

$$\mathbf{k}_i = \frac{\omega}{c} (\sin \theta \cos \phi, \sin \theta \sin \phi, \cos \theta) \quad (6.1)$$

where ϕ is the azimuthal angle of incidence. It should be noted that θ and ϕ are defined as the angles of incidence in air, which differ from the angles of propagation inside the PhCs. The reduced band structure for a given angle in air can then be calculated from the full band structure (Figure 6.4) by applying the conditions for momentum and energy conservation. For bands involving diffraction by lattice vectors \mathbf{G} not collinear with $[111]$ these can be written as

$$\mathbf{k}_{\parallel} + \mathbf{G}_{\parallel} = \frac{\omega}{c} (\sin \theta \cos \phi, \sin \theta \sin \phi, 0) \quad (6.2)$$

$$\epsilon_n(\mathbf{k}_{\parallel}, \mathbf{k}_z) = \hbar\omega \quad (6.3)$$

where \mathbf{k}_{\parallel} is the \mathbf{k} -component parallel to the (111) surface, \mathbf{G}_{\parallel} is the parallel component of any reciprocal lattice vector \mathbf{G} , is the \mathbf{k} -component parallel to ΓL , and $\epsilon_n(\mathbf{k}_{\parallel}, \mathbf{k}_z)$ is the n th energy band of a photon with wavevector \mathbf{k} . \mathbf{k}_{\parallel} is determined by the incidence angle θ , while \mathbf{k}_z and the reduced bands can be found by solving equations (6.2) and (6.3).

Finally we employed a scattering matrix (KKR) method to calculate band structures and directional reflection spectra for the inverse opals at different angles [14] and verify the coupling of different polarizations to the photonic bands. The polarizations of the first six bands are shown in Figure 6.4. Bands 1 (s) and 2 (p) as well as 3 (p) and 4 (s) are degenerate along ΓL but split near the U -point. The polarization of bands depends on the mode symmetry [11]: For

example, for p -polarization the \mathbf{E} field is contained in the diffraction plane, and the mirror reflection with respect to that plane therefore leaves the field vector unchanged. As a result, the symmetric modes along the LU direction can only be excited by a symmetric p -polarized incident fields. The primary gap is noticeably wider for s -polarization at the U -point [134]. It should also be pointed out that band 5 (p) is uncoupled along Γ - L , i.e. it cannot be excited by light incident from the outside due to symmetry restrictions [11]. Bands 5 and 6 (shifting towards lower frequencies along L - U) correspond to modes diffracted by the (200) planes [125, 146].

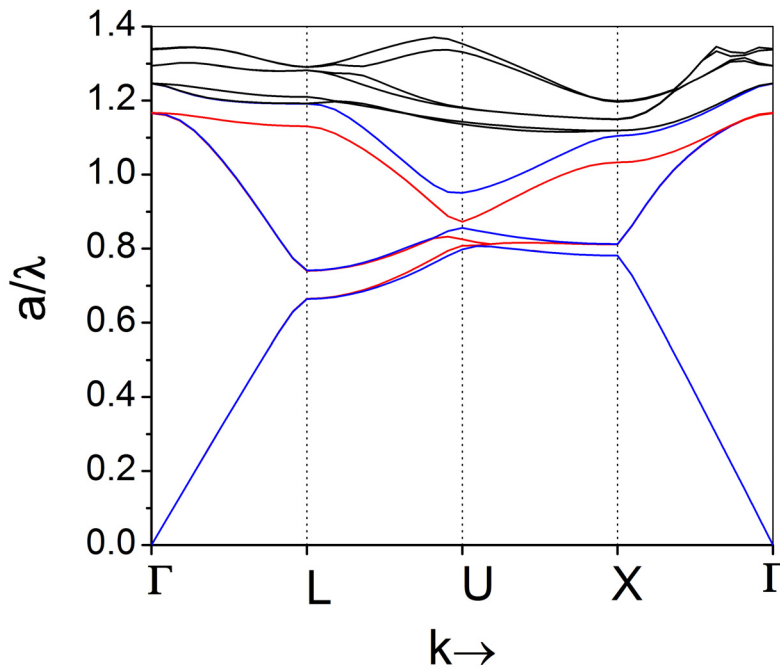


Figure 6.4: Band structure of a ZnO inverse opal with $d=400\text{nm}$, calculated for $n(\omega)$. S -polarized bands are shown in red, p -polarized bands in blue. Polarization states were obtained from coupling coefficients calculated by the layer KKR method.

6.4 Results

6.4.1 Reflection Data

Figure 6.5 shows the results of the reflection measurements from $\theta=5^\circ$ to 55° for both p - and s -polarized light. With increasing angle of incidence, the primary stop band peaks shift to shorter wavelengths, as expected from the band structure. At the same time, the higher-order peaks are less dispersive and slightly red-shift. There is a pronounced difference in the spectra for p - and s -polarized light: For s -polarization, the first high-energy peak ($\lambda=511\text{nm}$ at 0°) shifts towards the primary peak and two peaks exhibit an “avoided crossing” behavior at higher angles, whereas this peak is missing entirely in the p -polarized light.

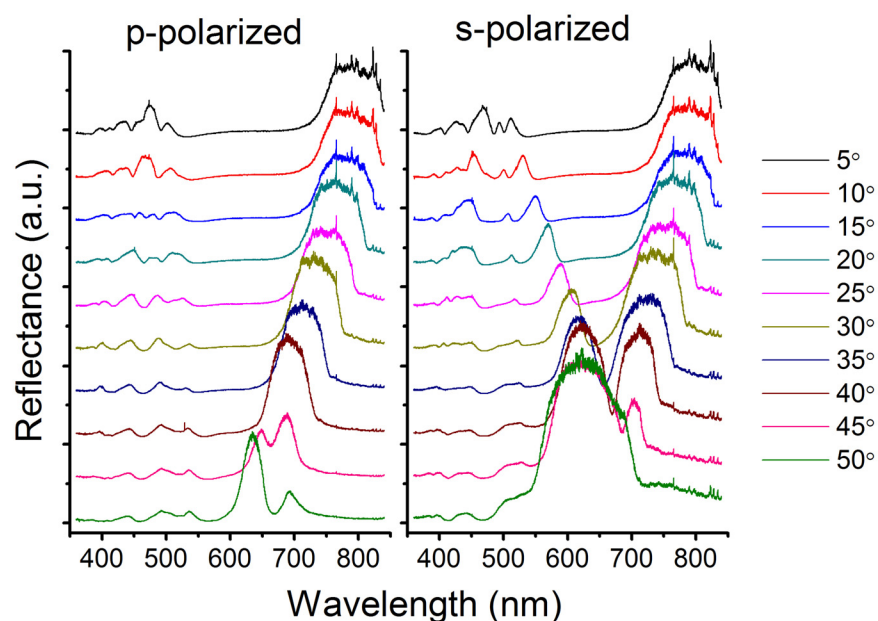


Figure 6.5: Reflection spectra from $\theta=5^\circ$ to 55° for p - and s -polarization.

These results agree well with data obtained from TiO₂ inverse opals at angles $\theta > 35^\circ$ [125]. Both the avoided crossing and polarization-dependence have been attributed to multiple diffraction, which leads to a coupling of Bragg waves diffracted by (111), (200), and (11-1) planes in the PhC.

6.4.2 Photoluminescence Measurements

Figure 6.6 shows the PL spectra of the random reference sample and the $d=400\text{nm}$ inverse opal for p- and s-polarization. For comparison, the spectra were normalized to overlap at the long-wavelength edge of the scan at $\lambda=880\text{nm}$ (well out of the PBG region). Suppression of emission is apparent in the spectral range of the primary PBG (shifting to shorter wavelengths), with a small enhancement of intensity at the low-frequency (dielectric) edge of the gap at higher angles. In addition, there is a strong enhancement peak for s-polarized light, which shifts from $\lambda\sim 580\text{nm}$ at 20° to $\sim 665\text{nm}$ at 40° .

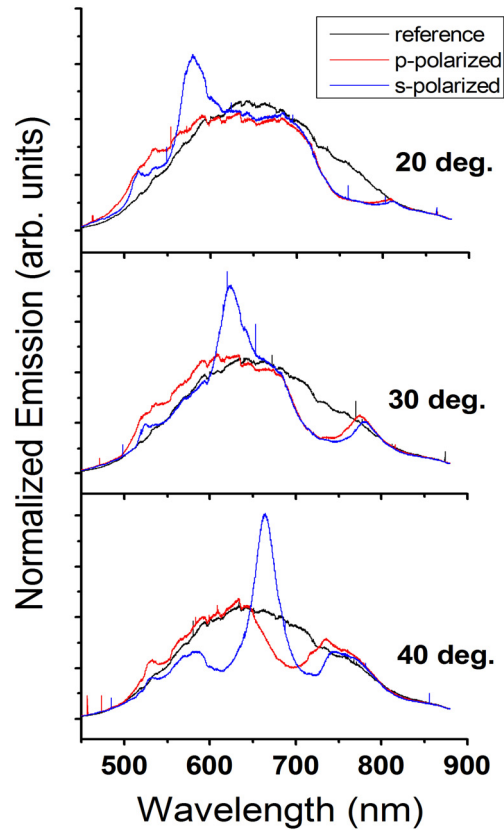


Figure 6.6: PL spectra for a random reference sample and a $d=400\text{nm}$ inv. opal. Spectra are normalized to overlap at $\lambda=880\text{nm}$.

6.5 Discussion

To get a clearer picture of the spectral and angular dispersion of the observed PL features, we calculated the ratio of emission from the PhC sample and the random sample (Figure 6.7). The spectra are identical for $\theta=0^\circ$, of course, with a dip in emission due to the first PBG and several sharp peaks indicating emission enhancement at wavelengths between 400nm and 500nm. With increasing angle, both polarizations exhibit weakly dispersive peaks (e.g. at

$\lambda=505\text{nm}$ for 10° in *s*-polarization), but the main difference between polarization is clearly the strong red-shifting peak in *s*-polarized emission.

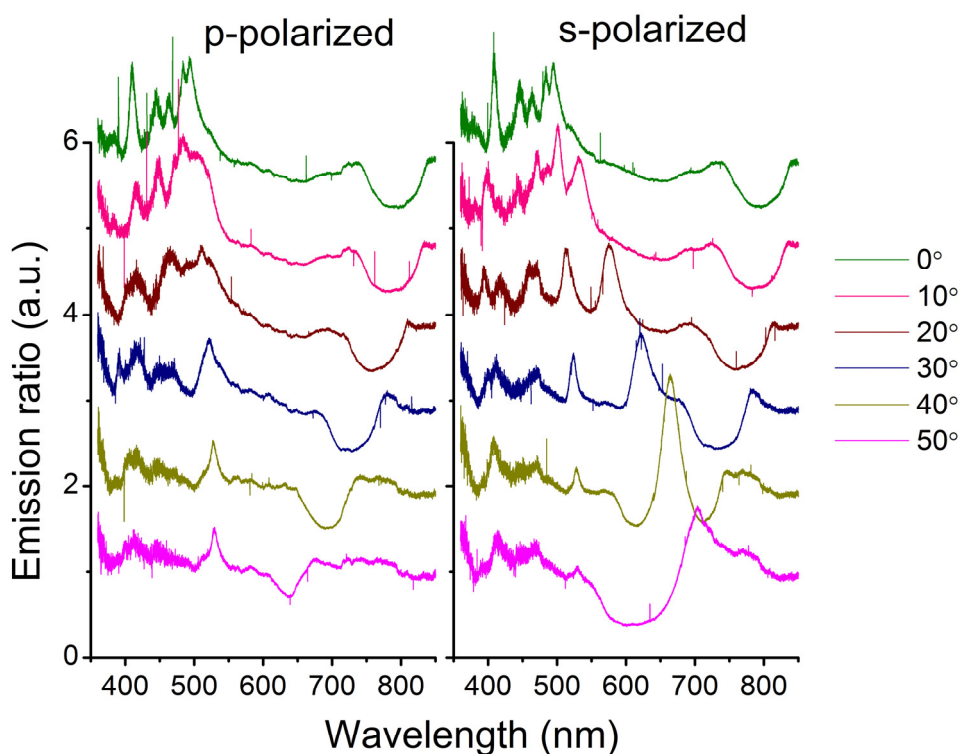


Figure 6.7: Emission ratio spectra, normalized by the respective reference spectra.

The emission ratio reaches a maximum value of 2.32 at 40° for this peak. To identify the physical mechanism responsible for the observed reflection and emission behavior, we need to correlate the experimental data with the calculated band structures. Figure 6.8 plots the reduced band structures calculated by the layer KKR method with the reflectance and emission ratio spectra, for angles $\theta=20^\circ$, 30° , and 40° and both *p*- (blue) and *s*-polarization (red).

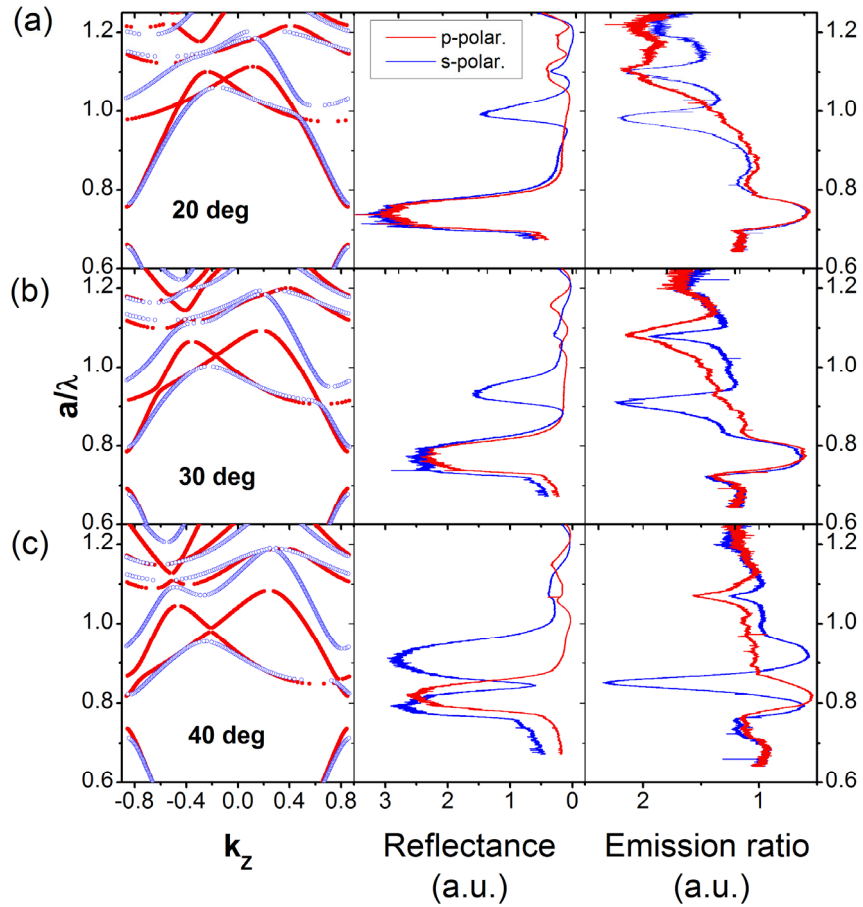


Figure 6.8: Reduced band structures, reflectance, and emission ratios for s - (blue) and p -polarization, for angles of (a) $\theta=20^\circ$, (b) $\theta=30^\circ$, and (c) $\theta=40^\circ$.

Comparing p - and s -polarized bands in the reduced band structures shows some significant differences: The s -bands 4 and 6 show a splitting in energy and avoided crossing, indicating strong coupling and band repulsion of the Bloch modes due to multiple Bragg diffraction, while the p -bands (3 and 5) exhibit only very small splitting and almost cross. This implies that the photonic band 5 does not couple with free-photon-like band 3. The peak in reflection in s -polarization roughly corresponds to the avoided crossing of the s -bands, suggesting that it is related to multiple diffraction involving the (200) planes. One possible explanation for this

different behavior can be found from the theory of multiple X-ray diffraction [147]: Coherent scattering of *p*-polarized EM waves is forbidden by polarization if $\theta=45^\circ$, since according to Maxwell's equation an accelerated charge does not emit in the direction of its acceleration. (In optics this is more commonly known as Brewster angle effect.) Multiple diffraction is polarization-forbidden if any of the involved Bragg angles are (close to) $\pi/4$, i.e. the secondary beam is at right angle with the incident or the primary beam. The existence of such critical angles has also been used to explain the interaction of polarized with weakly-scattering PhCs [148]. For diffraction in the *Γ -L-U-X* plane several such angles exist (for example, secondary (200) diffraction is prohibited for light incident along *Γ -K*, see Figure 6.9.)

As seen in Figure 6.8, the s-polarized peak in the emission ratio is located at the low-frequency edge of the reflection peak and follows the edge of flat diffraction band red-shifting with increasing angle. Pavarini et al. have recently shown how such diffraction bands can lead to van Hove singularities in the reduced DOS [145], which could explain the enhancement in emission ratio in terms of a redistribution of emission. Barth et al. have shown related effects of the angular DOS near the edge of the primary PBG [139]. This situation is schematically depicted in Figure 6.9, which presents sections through the dispersion surface of the ZnO inverse opals in the *Γ -L-U-X* plane at a reduced frequency of $a/\lambda=0.85$ ($\lambda=665\text{nm}$). Figure 6.9a shows the normal conditions of beam propagation at low angles. In this situation the reduced DOS does not differ much from an isotropic medium since the bands are almost parallel to the BZ surface. In contrast, at higher angles (40° in Figure 6.9b) the photonic bands are almost perpendicular to the BZ surface. For a given detection cone (shown in green as $\sim 5^\circ$) a large portion of the band

contributes to the detected emission intensity. This agrees well with the measured peak in the emission ratio (compare to Figure 6.7c).

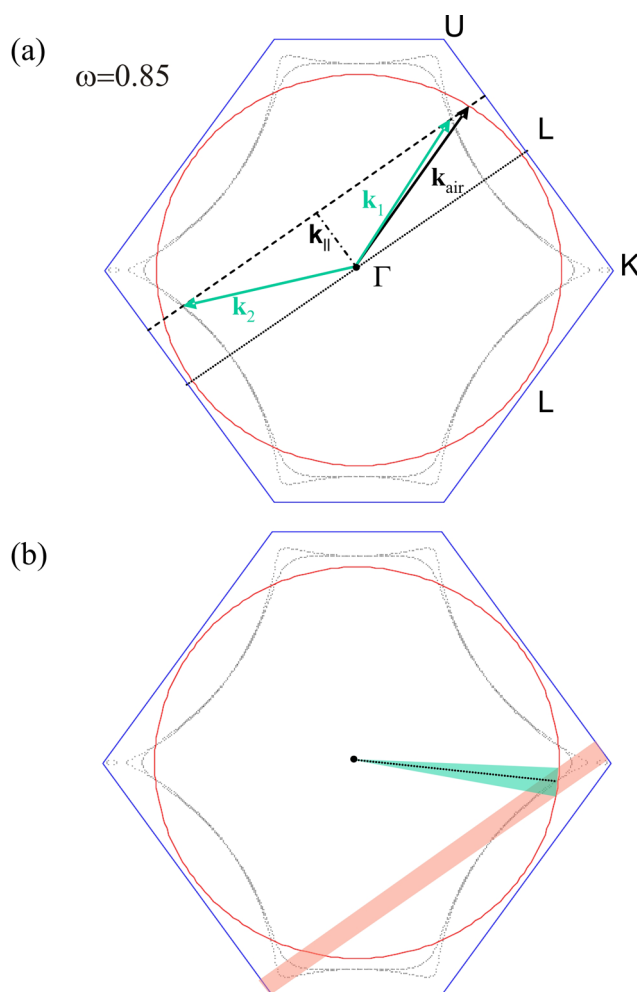


Figure 6.9: Section of the dispersion surface in the Γ -L-U-X plane at reduced frequency $a/\lambda=0.85$. The red circle gives the dispersion in air; the black dotted lines represent the bands inside the PhC. (a) Dispersion diagram for incident k vector at $\theta=20^\circ$. (b) At larger angle ($\theta=40^\circ$) bands are almost perpendicular to the BZ. The detection cone is shown in green; the range of k -vectors is shaded red.

The question remains why we do not observe an emission peak related to the edge of band 5. In fact, the behavior of the PhC seems to be dominated by the free-photon band, with little apparent influence of the flat diffraction band, although for spontaneous emission by light sources within the crystal all modes are assumed to be equally populated. While band 5 is uncoupled in the Γ - L direction, preliminary results of the KKR calculations have not shown a significant difference in the branching ratios (i.e. coupling efficiencies to the outside) between band 5 and 6 for directions off the surface normal. The theoretical work regarding this question is ongoing.

Figure 6.10 summarizes the experimental emission and reflection data as gray scale maps and shows the calculated directional reflectance for comparison, which is in good qualitative agreement.

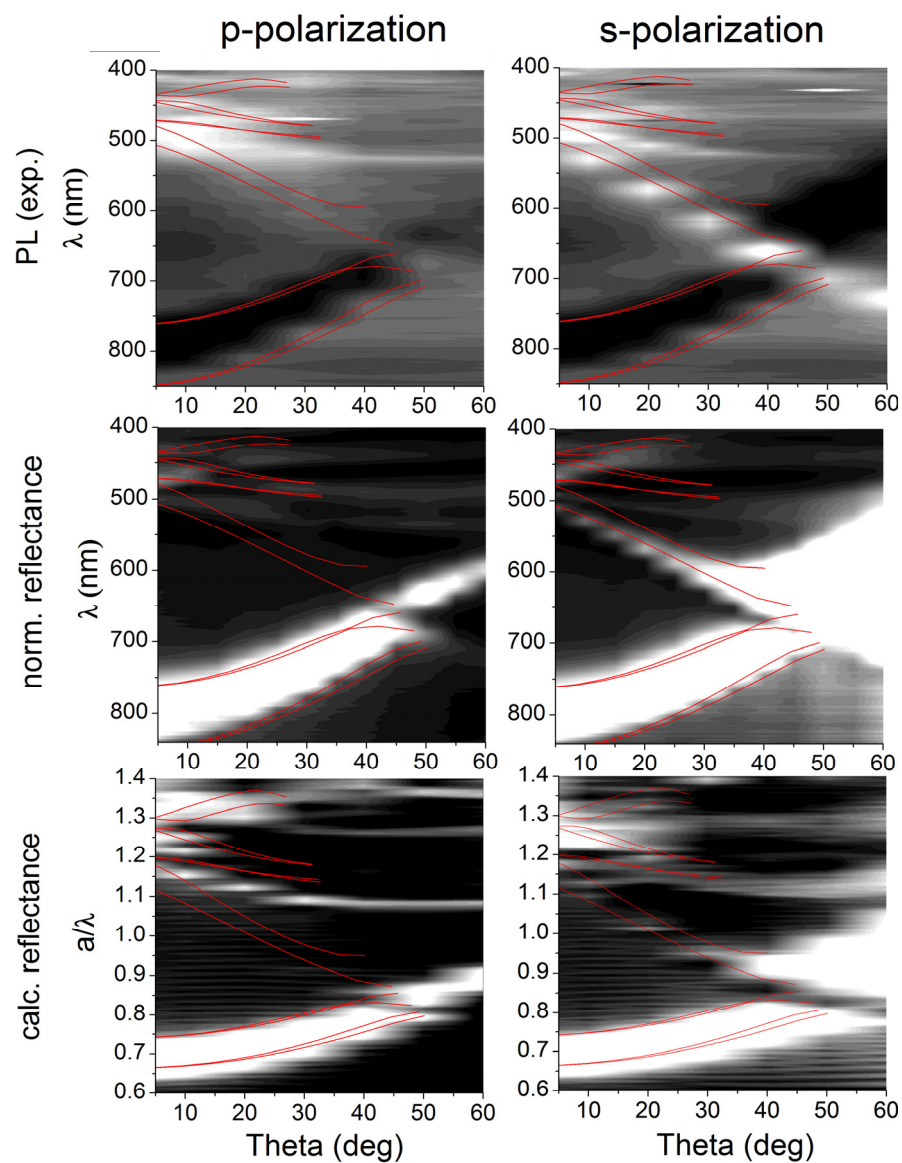


Figure 6.10: Comparison of (a) PL emission ratio, (b) measured, and (c) calculated reflectance versus angle θ , plotted as gray scale maps. The experimental reflection data are in good agreement with the results of the KKR calculations. The PWE band structures are overlaid in red.

6.6 Conclusions

We have measured angle- and polarization-resolved reflection and emission properties of ZnO inverse opals. The reflection spectra are in good agreement with published data and can be explained in terms of multiple Bragg diffraction and resulting coupling of modes. The polarization-dependence of the reflection features is discussed in terms of polarization-forbidden reflections at critical angles for p -polarization and agrees with the calculated reduced band structures. We also observe strongly modified spontaneous emission from the PhCs, with suppression due to the primary PBG and strong angular and spectral redistribution of emission in the higher-order band structure. A normalized emission ratio of over 2.3 has been observed for s -polarized light. This suggests that in high-quality 3D PhCs significant changes in the radiation pattern can be achieved, which offers possible applications for the tailoring of highly efficient light sources.

7. Conclusions and Future Studies

The work presented here demonstrates the promising properties of optically active 3D ZnO PhCs for the control of light and tailoring the photonic response of a material, with potential applications as microlasers and high-efficiency light sources. However, as with most PhC research, hurdles remain both in the fabrication and the theoretical understanding of these structures.

From a materials science perspective, several options for further improving the materials quality exist. Improved template fabrication, by using either a more controlled self-assembly procedure [98] or a more advanced process such as 3D holographic lithography [36], could help in reducing the disorder in the structures. Developing a method to remove the polymer template without firing (e.g. by plasma etching) would result in more flexibility in controlling the materials properties. Lastly, the ability of the ALD process to create multilayer composite structures could be used to tailor the refractive index profile, passivate the ZnO surface, introduce other materials such as quantum dots [149] or create metallodielectric structures.

On the physical side, several ongoing collaborations are concerned with nonlinear optical properties of the ZnO PhCs and continued investigation of the spontaneous emission properties discussed in Chapter 6. The ZnO structures offer a unique platform to study the complex physics of PhC in the presence of optical gain, disorder, and optical nonlinearities.

8. References

1. J. D. Joannopoulos, R. D. Meade, and J. N. Winn, *Photonic Crystals: Molding the Flow of Light* (Princeton University Press, Princeton, New Jersey, 1995).
2. K. Sakoda, *Optical properties of photonic crystals*, 2nd ed., Springer series in optical sciences ; v. 80 (Springer, Berlin ; New York, 2004), pp. xiii, 253.
3. P. Russell, "Photonic crystal fibers," *Science* **299**(5605), 358-362 (2003).
4. C. Lopez, "Materials aspects of photonic crystals," *Advanced Materials* **15**(20), 1679-1704 (2003).
5. E. Yablonovitch and T. J. Gmitter, "Photonic Band-Structure - the Face-Centered-Cubic Case," *Physical Review Letters* **63**(18), 1950-1953 (1989).
6. Y. N. Xia, B. Gates, and Z. Y. Li, "Self-assembly approaches to three-dimensional photonic crystals," *Advanced Materials* **13**(6), 409-413 (2001).
7. A. B. Djurisic and Y. H. Leung, "Optical properties of ZnO nanostructures," *Small* **2**(8-9), 944-961 (2006).
8. E. Yablonovitch, "Inhibited Spontaneous Emission in Solid-State Physics and Electronics," *Physical Review Letters* **58**(20), 2059-2062 (1987).
9. S. John, "Strong Localization of Photons in Certain Disordered Dielectric Superlattices," *Physical Review Letters* **58**(23), 2486-2489 (1987).
10. P. Vukusic and J. R. Sambles, "Photonic structures in biology," *Nature* **424**(6950), 852-855 (2003).
11. F. Lopez-Tejeira, T. Ochiai, K. Sakoda, and J. Sanchez-Dehesa, "Symmetry characterization of eigenstates in opal-based photonic crystals," *Physical Review B* **65**(19), - (2002).
12. S. G. Johnson and J. D. Joannopoulos, "Block-iterative frequency-domain methods for Maxwell's equations in a planewave basis," *Optics Express* **8**(3), 173-190 (2001).
13. A. Modinos, N. Stefanou, and V. Yannopoulos, "Applications of the layer-KKR method to photonic crystals," *Optics Express* **8**(3), 197-202 (2001).

14. N. Stefanou, V. Yannopoulos, and A. Modinos, "MULTEM 2: A new version of the program for transmission and band-structure calculations of photonic crystals," *Computer Physics Communications* **132**(1-2), 189-196 (2000).
15. T. Ochiai and J. Sanchez-Dehesa, "Superprism effect in opal-based photonic crystals," *Physical Review B* **64**(24)(2001).
16. A. F. Koenderink, "Emission and Transport of Light in Photonic Crystals," (University of Amsterdam, Amsterdam, The Netherlands, 2003).
17. P. W. Anderson, "Absence of Diffusion in Certain Random Lattices," *Physical Review* **109**(5), 1492-1505 (1958).
18. D. S. Wiersma, P. Bartolini, A. Lagendijk, and R. Righini, "Localization of light in a disordered medium," *Nature* **390**(6661), 671-673 (1997).
19. H. Cao, "Lasing in random media," *Waves in Random Media* **13**(3), R1-R39 (2003).
20. E. Kuramochi, M. Notomi, S. Mitsugi, A. Shinya, T. Tanabe, and T. Watanabe, "Ultrahigh-Q photonic crystal nanocavities realized by the local width modulation of a line defect," *Applied Physics Letters* **88**(4), - (2006).
21. M. Loncar, M. Hochberg, A. Scherer, and Y. M. Qiu, "High quality factors and room-temperature lasing in a modified single-defect photonic crystal cavity," *Optics Letters* **29**(7), 721-723 (2004).
22. K. Sakoda, K. Ohtaka, and T. Ueta, "Low-threshold laser oscillation due to group-velocity anomaly peculiar to two- and three-dimensional photonic crystals," *Optics Express* **4**(12), 481 - 489 (1999).
23. E. Yablonovitch, T. J. Gmitter, and K. M. Leung, "Photonic Band-Structure - the Face-Centered-Cubic Case Employing Nonspherical Atoms," *Physical Review Letters* **67**(17), 2295-2298 (1991).
24. A. Chelnokov, K. Wang, S. Rowson, P. Garoche, and J. M. Lourtioz, "Near-infrared Yablonovite-like photonic crystals by focused-ion-beam etching of macroporous silicon," *Applied Physics Letters* **77**(19), 2943-2945 (2000).
25. E. Ozbay, E. Michel, G. Tuttle, R. Biswas, M. Sigalas, and K. M. Ho, "Micromachined Millimeter-Wave Photonic Band-Gap Crystals," *Applied Physics Letters* **64**(16), 2059-2061 (1994).
26. S. Y. Lin, J. G. Fleming, D. L. Hetherington, B. K. Smith, R. Biswas, K. M. Ho, M. M. Sigalas, W. Zubrzycki, S. R. Kurtz, and J. Bur, "A three-dimensional photonic crystal operating at infrared wavelengths," *Nature* **394**(6690), 251-253 (1998).

27. K. Aoki, H. T. Miyazaki, H. Hirayama, K. Inoshita, T. Baba, N. Shinya, and Y. Aoyagi, "Three-dimensional photonic crystals for optical wavelengths assembled by micromanipulation," *Applied Physics Letters* **81**(17), 3122-3124 (2002).
28. M. Qi, E. Lidorikis, P. T. Rakich, S. G. Johnson, J. D. Joannopoulos, E. P. Ippen, and H. I. Smith, "A three-dimensional optical photonic crystal with designed point defects," *Nature* **429**(6991), 538-542 (2004).
29. G. M. Gratson, F. Garcia-Santamaria, V. Lousse, M. J. Xu, S. H. Fan, J. A. Lewis, and P. V. Braun, "Direct-write assembly of three-dimensional photonic crystals: Conversion of polymer scaffolds to silicon hollow-woodpile structures," *Advanced Materials* **18**(4), 461-+ (2006).
30. M. Deubel, G. Von Freymann, M. Wegener, S. Pereira, K. Busch, and C. M. Soukoulis, "Direct laser writing of three-dimensional photonic-crystal templates for telecommunications," *Nature Materials* **3**(7), 444-447 (2004).
31. S. Wong, M. Deubel, F. Perez-Willard, S. John, G. A. Ozin, M. Wegener, and G. von Freymann, "Direct laser writing of three-dimensional photonic crystals with complete a photonic bandgap in chalcogenide glasses," *Advanced Materials* **18**(3), 265-+ (2006).
32. Y. V. Miklyaev, D. C. Meisel, A. Blanco, G. von Freymann, K. Busch, W. Koch, C. Enkrich, M. Deubel, and M. Wegener, "Three-dimensional face-centered-cubic photonic crystal templates by laser holography: fabrication, optical characterization, and band-structure calculations," *Applied Physics Letters* **82**(8), 1284-1286 (2003).
33. D. C. Meisel, M. Wegener, and K. Busch, "Three-dimensional photonic crystals by holographic lithography using the umbrella configuration: Symmetries and complete photonic band gaps," *Physical Review B* **70**(16), - (2004).
34. M. Campbell, D. N. Sharp, M. T. Harrison, R. G. Denning, and A. J. Turberfield, "Fabrication of photonic crystals for the visible spectrum by holographic lithography," *Nature* **404**(6773), 53-56 (2000).
35. J. Scrimgeour, D. N. Sharp, C. F. Blanford, O. M. Roche, R. G. Denning, and A. J. Turberfield, "Three-dimensional optical lithography for photonic microstructures," *Advanced Materials* **18**(12), 1557-+ (2006).
36. J. S. King, E. Graugnard, O. M. Roche, D. N. Sharp, J. Scrimgeour, R. G. Denning, A. J. Turberfield, and C. J. Summers, "Infiltration and inversion of holographically defined polymer photonic crystal templates by atomic layer deposition," *Advanced Materials* **18**(12), 1561-+ (2006).
37. T. Y. M. Chan, O. Toader, and S. John, "Photonic band-gap formation by optical-phase-mask lithography," *Physical Review E* **73**(4)(2006).

38. N. Tetreault, G. von Freymann, M. Deubel, M. Hermatschweiler, F. Perez-Willard, S. John, M. Wegener, and G. A. Ozin, "New route to three-dimensional photonic bandgap materials: Silicon double inversion of polymer templates," *Advanced Materials* **18**(4), 457-+ (2006).
39. S. H. Park, D. Qin, and Y. Xia, "Crystallization of mesoscale particles over large areas," *Advanced Materials* **10**(13), 1028-+ (1998).
40. P. Jiang, J. F. Bertone, K. S. Hwang, and V. L. Colvin, "Single-crystal colloidal multilayers of controlled thickness," *Chemistry of Materials* **11**(8), 2132-2140 (1999).
41. Y. Yin, Z. Y. Li, and Y. Xia, "Template-directed growth of (100)-oriented colloidal crystals," *Langmuir* **19**(3), 622-631 (2003).
42. S. M. Yang, H. Miguez, and G. A. Ozin, "Opal circuits of light - Planarized microphotonic crystal chips," *Advanced Functional Materials* **12**(6-7), 425-431 (2002).
43. P. Ferrand, M. Egen, B. Griesebock, J. Ahopelto, M. Muller, R. Zentel, S. G. Romanov, and C. M. S. Torres, "Self-assembly of three-dimensional photonic crystals on structured silicon wafers," *Applied Physics Letters* **81**(15), 2689-2691 (2002).
44. H. S. Sozuer, J. W. Haus, and R. Inguva, "Photonic Bands - Convergence Problems with the Plane-Wave Method," *Physical Review B* **45**(24), 13962-13972 (1992).
45. K. Busch and S. John, "Photonic band gap formation in certain self-organizing systems," *Physical Review E* **58**(3), 3896-3908 (1998).
46. R. C. Schroden, M. Al-Daous, C. F. Blanford, and A. Stein, "Optical properties of inverse opal photonic crystals," *Chemistry of Materials* **14**(8), 3305-3315 (2002).
47. J. E. G. J. Wijnhoven, L. Bechger, and W. L. Vos, "Fabrication and characterization of large macroporous photonic crystals in titania," *Chemistry of Materials* **13**(12), 4486-4499 (2001).
48. J. E. G. J. Wijnhoven and W. L. Vos, "Preparation of photonic crystals made of air spheres in titania," *Science* **281**(5378), 802-804 (1998).
49. P. Braun and P. Wiltzius, "Electrochemical fabrication of 3D microperiodic porous materials," *Advanced Materials* **13**(7), 482-+ (2001).
50. T. Sumida, Y. Wada, T. Kitamura, and S. Yanagida, "Macroporous ZnO films electrochemically prepared by templating of opal films," *Chemistry Letters* (1), 38-39 (2001).

51. P. V. Braun, R. W. Zehner, C. A. White, M. K. Weldon, C. Kloc, S. S. Patel, and P. Wiltzius, "Epitaxial growth of high dielectric contrast three-dimensional photonic crystals," *Advanced Materials* **13**(10), 721-724 (2001).
52. S. G. Romanov, N. P. Johnson, A. V. Fokin, V. Y. Butko, H. M. Yates, M. E. Pemble, and C. M. S. Torres, "Enhancement of the photonic gap of opal-based three-dimensional gratings," *Applied Physics Letters* **70**(16), 2091-2093 (1997).
53. H. M. Yates, W. R. Flavell, M. E. Pemble, N. P. Johnson, S. G. Romanov, and C. M. SotomayorTorres, "Novel quantum confined structures via atmospheric pressure MOCVD growth in asbestos and opals," *Journal of Crystal Growth* **170**(1-4), 611-615 (1997).
54. S. G. Romanov, R. M. De la Rue, H. M. Yates, and M. E. Pemble, "Impact of GaP layer deposition upon photonic bandgap behaviour of opal," *Journal of Physics-Condensed Matter* **12**(3), 339-348 (2000).
55. A. A. Zakhidov, I. I. Khayrullin, R. H. Baughman, Z. Iqbal, K. Yoshino, Y. Kawagishi, and S. Tatsuha, "CVD synthesis of carbon-based metallic photonic crystals," *Nanostructured Materials* **12**(5-8), 1089-1095 (1999).
56. M. Muller, R. Zentel, T. Maka, S. G. Romanov, and C. M. S. Torres, "Photonic crystal films with high refractive index contrast," *Advanced Materials* **12**(20), 1499-1503 (2000).
57. H. M. Yates, M. E. Pemble, A. Blanco, H. Miguez, C. Lopez, and F. Meseguer, "Growth of tin oxide in opal," *Chemical Vapor Deposition* **6**(6), 283-+ (2000).
58. A. Blanco, E. Chomski, S. Grabtchak, M. Ibisate, S. John, S. W. Leonard, C. Lopez, F. Meseguer, H. Miguez, J. P. Mondia, G. A. Ozin, O. Toader, and H. M. van Driel, "Large-scale synthesis of a silicon photonic crystal with a complete three-dimensional bandgap near 1.5 micrometres," *Nature* **405**(6785), 437-440 (2000).
59. H. Miguez, E. Chomski, F. Garcia-Santamaria, M. Ibisate, S. John, C. Lopez, F. Meseguer, J. P. Mondia, G. A. Ozin, O. Toader, and H. M. van Driel, "Photonic bandgap engineering in germanium inverse opals by chemical vapor deposition," *Advanced Materials* **13**(21), 1634-+ (2001).
60. F. Garcia-Santamaria, M. Ibisate, I. Rodriguez, F. Meseguer, and C. Lopez, "Photonic band engineering in opals by growth of Si/Ge multilayer shells," *Advanced Materials* **15**(10), 788-+ (2003).
61. A. Rugge, J. S. Becker, R. G. Gordon, and S. H. Tolbert, "Tungsten nitride inverse opals by atomic layer deposition," *Nano Letters* **3**(9), 1293-1297 (2003).

62. J. S. King, C. W. Neff, C. J. Summers, W. Park, S. Blomquist, E. Forsythe, and D. Morton, "High-filling-fraction inverted ZnS opals fabricated by atomic layer deposition," *Applied Physics Letters* **83**(13), 2566-2568 (2003).
63. A. Rügge, J. S. Park, R. G. Gordon, and S. H. Tolbert, "Tantalum(V) nitride inverse opals as photonic structures for visible wavelengths," *Journal of Physical Chemistry B* **109**(9), 3764-3771 (2005).
64. J. S. King, E. Graugnard, and C. J. Summers, "TiO₂ inverse opals fabricated using low-temperature atomic layer deposition," *Advanced Materials* **17**(8), 1010-1013 (2005).
65. I. M. Povey, D. Whitehead, K. Thomas, M. E. Pemble, M. Bardosova, and J. Renard, "Photonic crystal thin films of GaAs prepared by atomic layer deposition," *Applied Physics Letters* **89**(10)(2006).
66. M. N. Shkunov, Z. V. Vardeny, M. C. DeLong, R. C. Polson, A. A. Zakhidov, and R. H. Baughman, "Tunable, gap-state lasing in switchable directions for opal photonic crystals," *Advanced Functional Materials* **12**(1), 21-26 (2002).
67. S. G. Romanov, D. N. Chigrin, V. G. Solovyev, T. Maka, N. Gaponik, A. Eychmüller, A. L. Rogach, and C. M. S. Torres, "Light emission in a directional photonic bandgap," *Physica Status Solidi a-Applied Research* **197**(3), 662-672 (2003).
68. P. Lodahl, A. F. van Driel, I. S. Nikolaev, A. Irman, K. Overgaag, D. L. Vanmaekelbergh, and W. L. Vos, "Controlling the dynamics of spontaneous emission from quantum dots by photonic crystals," *Nature* **430**(7000), 654-657 (2004).
69. P. V. Braun, R. W. Zehner, C. A. White, M. K. Weldon, C. Kloc, S. S. Patel, and P. Wiltzius, "Optical spectroscopy of high dielectric contrast 3D photonic crystals," *Europhysics Letters* **56**(2), 207-213 (2001).
70. S. L. Kuai, X. F. Hu, and V. V. Truong, "Synthesis of thin film titania photonic crystals through a dip-infiltrating sol-gel process," *Journal of Crystal Growth* **259**(4), 404-410 (2003).
71. F. Meseguer, A. Blanco, H. Miguez, F. Garcia-Santamaria, M. Ibasate, and C. Lopez, "Synthesis of inverse opals," *Colloids and Surfaces a-Physicochemical and Engineering Aspects* **202**(2-3), 281-290 (2002).
72. V. G. Golubev, J. L. Hutchison, V. A. Kosobukin, D. A. Kurdyukov, A. V. Medvedev, A. B. Pevtsov, J. Sloan, and L. M. Sorokin, "Three-dimensional ordered silicon-based nanostructures in opal matrix: preparation and photonic properties," *Journal of Non-Crystalline Solids* **299**, 1062-1069 (2002).

73. S. G. Romanov, D. N. Chigrin, C. M. S. Torres, N. Gaponik, A. Eychmuller, and A. L. Rogach, "Emission stimulation in a directional band gap of a CdTe-loaded opal photonic crystal," *Physical Review E* **69**(4), - (2004).
74. A. F. Koenderink, L. Bechger, A. Lagendijk, and W. L. Vos, "An experimental study of strongly modified emission in inverse opal photonic crystals," *Physica Status Solidi a-Applied Research* **197**(3), 648-661 (2003).
75. E. W. Seelig, B. Tang, A. Yamilov, H. Cao, and R. P. H. Chang, "Self-assembled 3D photonic crystals from ZnO colloidal spheres," *Materials Chemistry and Physics* **80**(1), 257-263 (2003).
76. X. Wu, A. Yamilov, X. Liu, S. Li, V. P. Dravid, R. P. H. Chang, and H. Cao, "Ultraviolet photonic crystal laser," *Applied Physics Letters* **85**(17), 3657-3659 (2004).
77. S. M. Abrarov, S. U. Yuldashev, T. W. Kim, S. B. Lee, Y. H. Kwon, and T. W. Kang, "Effect of photonic band-gap on photoluminescence of ZnO deposited inside the green synthetic opal," *Optics Communications* **250**(1-3), 111-119 (2005).
78. A. Emelchenko, A. N. Gruzintsev, V. V. Masalov, E. N. Samarov, V. Bazhenov, and E. E. Yakimov, "ZnO-infiltrated opal: influence of the stop-zone on the UV spontaneous emission," *Journal of Optics a-Pure and Applied Optics* **7**(2), S213-S218 (2005).
79. B. H. Juarez, P. D. Garcia, D. Golmayo, A. Blanco, and C. Lopez, "ZnO inverse opals by chemical vapor deposition," *Advanced Materials* **17**(22), 2761-+ (2005).
80. T. Suntola, "Atomic Layer Epitaxy," *Thin Solid Films* **216**(1), 84-89 (1992).
81. C. H. L. Goodman and M. V. Pessa, "Atomic Layer Epitaxy," *Journal of Applied Physics* **60**(3), R65-R81 (1986).
82. S. M. George, A. W. Ott, and J. W. Klaus, "Surface chemistry for atomic layer growth," *Journal of Physical Chemistry* **100**(31), 13121-13131 (1996).
83. H. Kim, "Atomic layer deposition of metal and nitride thin films: Current research efforts and applications for semiconductor device processing," *Journal of Vacuum Science & Technology B* **21**(6), 2231-2261 (2003).
84. T. Suntola and J. Hyvarinen, "Atomic Layer Epitaxy," *Annual Review of Materials Science* **15**, 177-195 (1985).
85. R. L. Puurunen, "Growth per cycle in atomic layer deposition: Real application examples of a theoretical model," *Chemical Vapor Deposition* **9**(6), 327-332 (2003).

86. J. W. Elam, D. Routkevitch, P. P. Mardilovich, and S. M. George, "Conformal coating on ultrahigh-aspect-ratio nanopores of anodic alumina by atomic layer deposition," *Chemistry of Materials* **15**(18), 3507-3517 (2003).
87. O. Sneh, R. B. Clark-Phelps, A. R. Londergan, J. Winkler, and T. E. Seidel, "Thin film atomic layer deposition equipment for semiconductor processing," *Thin Solid Films* **402**(1-2), 248-261 (2002).
88. M. Scharrer, A. Yamilov, X. Wu, H. Cao, and R. P. H. Chang, "UV Lasing in High-Order Bands of Three-Dimensional ZnO Photonic Crystals," *Applied Physics Letters* **88**(20), 201103 (2006).
89. D. Gaillot, T. Yamashita, and C. J. Summers, "Photonic band gaps in highly conformal inverse-opal based photonic crystals," *Physical Review B: Condensed Matter and Materials Physics* **72**(20), 205109 (2005).
90. J. S. King, D. Heineman, E. Graugnard, and C. J. Summers, "Atomic layer deposition in porous structures: 3D photonic crystals," *Applied Surface Science* **244**(1-4), 511-516 (2005).
91. V. Lujala, J. Skarp, M. Tammenmaa, and T. Suntola, "Atomic Layer Epitaxy Growth of Doped Zinc-Oxide Thin-Films from Organometals," *Applied Surface Science* **82-3**, 34-40 (1994).
92. A. W. Ott and R. P. H. Chang, "Atomic layer-controlled growth of transparent conducting ZnO on plastic substrates," *Materials Chemistry and Physics* **58**(2), 132-138 (1999).
93. E. B. Yousfi, J. Fouache, and D. Lincot, "Study of atomic layer epitaxy of zinc oxide by in-situ quartz crystal microgravimetry," *Applied Surface Science* **153**(4), 223-234 (2000).
94. J. D. Ferguson, A. W. Weimer, and S. M. George, "Surface chemistry and infrared absorbance changes during ZnO atomic layer deposition on ZrO₂ and BaTiO₃ particles," *Journal of Vacuum Science & Technology A: Vacuum, Surfaces, and Films* **23**(1), 118-125 (2005).
95. J. S. King, C. W. Neff, S. Blomquist, E. Forsythe, D. Morton, and C. J. Summers, "ZnS-based photonic crystal phosphors fabricated using atomic layer deposition," *Physica Status Solidi B-Basic Research* **241**(3), 763-766 (2004).
96. L. L. Meng, H. Wei, A. Nagel, B. J. Wiley, L. E. Scriven, and D. J. Norris, "The role of thickness transitions in convective assembly," *Nano Letters* **6**(10), 2249-2253 (2006).
97. D. J. Norris, E. G. Arlinghaus, L. L. Meng, R. Heiny, and L. E. Scriven, "Opaline photonic crystals: How does self-assembly work?," *Advanced Materials* **16**(16), 1393-1399 (2004).

98. R. G. Shimmin, A. J. DiMauro, and P. V. Braun, "Slow vertical deposition of colloidal crystals: A Langmuir-Blodgett process?," *Langmuir* **22**(15), 6507-6513 (2006).
99. S. L. Kuai, X. F. Hu, A. Hache, and V. V. Truong, "High-quality colloidal photonic crystals obtained by optimizing growth parameters in a vertical deposition technique," *Journal of Crystal Growth* **267**(1-2), 317-324 (2004).
100. J. W. Elam, M. D. Groner, and S. M. George, "Viscous flow reactor with quartz crystal microbalance for thin film growth by atomic layer deposition," *Review of Scientific Instruments* **73**(8), 2981-2987 (2002).
101. J. S. King, "Fabrication of Opal-Based Photonic Crystals Using Atomic Layer Deposition," (Georgia Institute of Technology, Atlanta, GA, 2004).
102. P. D. Garcia and C. Lopez, "Optical study of Gamma L high energy photonic pseudogaps in ZnO inverted opals," *Journal of Applied Physics* **99**(4)(2006).
103. S. Nojima, "Enhancement of Optical Gain in Two-Dimensional Photonic Crystals with Active Lattice Points," *Jpn. J. Appl. Phys.* **37**(5B), L565 - L567 (1998).
104. L. Florescu, K. Busch, and S. John, "Semiclassical theory of lasing in photonic crystals," *Journal of the Optical Society of America B: Optical Physics* **19**(9), 2215-2223 (2002).
105. O. Painter, R. K. Lee, A. Scherer, A. Yariv, J. D. O'Brien, P. D. Dapkus, and I. Kim, "Two-dimensional photonic band-gap defect mode laser," *Science* **284**(5421), 1819-1821 (1999).
106. S. Noda, M. Yokoyama, M. Imada, A. Chutinan, and M. Mochizuki, "Polarization mode control of two-dimensional photonic crystal laser by unit cell structure design," *Science* **293**(5532), 1123-1125 (2001).
107. H.-G. Park, S.-H. Kim, S.-H. Kwon, Y.-G. Ju, J.-K. Yang, J.-H. Baek, S.-B. Kim, and Y.-H. Lee, "Electrically Driven Single-Cell Photonic Crystal Laser," *Science* **305**(5689), 1444-1447 (2004).
108. R. Colombelli, K. Srinivasan, M. Troccoli, O. Painter, C. F. Gmachl, D. M. Tennant, A. M. Sergent, D. L. Sivco, A. Y. Cho, and F. Capasso, "Quantum cascade surface-emitting photonic crystal laser," *Science* **302**(5649), 1374-1377 (2003).
109. T. N. Oder, J. Shakya, J. Y. Lin, and H. X. Jiang, "III-nitride photonic crystals," *Applied Physics Letters* **83**(6), 1231-1233 (2003).
110. A. David, C. Meier, R. Sharma, F. S. Diana, S. P. DenBaars, E. Hu, S. Nakamura, C. Weisbuch, and H. Benisty, "Photonic bands in two-dimensionally patterned multimode GaN waveguides for light extraction," *Applied Physics Letters* **87**(10), 101107 (2005).

111. G. R. Maskaly, M. A. Petruska, J. Nanda, I. V. Bezel, R. D. Schaller, H. Htoon, J. M. Pietryga, and V. I. Klimov, "Amplified Spontaneous Emission in Semiconductor-Nanocrystal/Synthetic-Opal Composites: Optical-Gain Enhancement via a Photonic Crystal Pseudogap," *Advanced Materials* **18**(3), 343-347 (2006).
112. Y. A. Vlasov, K. Luterova, I. Pelant, B. Honerlage, and V. N. Astratov, "Enhancement of optical gain of semiconductors embedded in three-dimensional photonic crystals," *Applied Physics Letters* **71**(12), 1616-1618 (1997).
113. S. G. Romanov, M. A. Kaliteevski, C. M. Sotomayor Torres, J. Manzanares Martinez, D. Cassagne, J. P. Albert, A. V. Kavokin, F. Laussy, V. V. Nikolaev, S. Brand, R. A. Abram, N. Gaponik, A. Eychmueller, and A. L. Rogach, "Stimulated emission due to light localization in the bandgap of disordered opals," *physica status solidi (c)* **1**(6), 1522 - 1530 (2004).
114. S. G. Romanov, D. N. Chigrin, C. M. S. Torres, N. Gaponik, A. Eychmuller, and A. L. Rogach, "Emission stimulation in a directional band gap of a CdTe-loaded opal photonic crystal," *Physical Review E* **69**(4), 046606 (2004).
115. K. Yoshino, S. Tatsuhara, Y. Kawagishi, M. Ozaki, A. A. Zakhidov, and Z. V. Vardeny, "Amplified spontaneous emission and lasing in conducting polymers and fluorescent dyes in opals as photonic crystals," *Applied Physics Letters* **74**(18), 2590-2592 (1999).
116. W. Y. Cao, A. Munoz, P. Palffy-Muhoray, and B. Taheri, "Lasing in a three-dimensional photonic crystal of the liquid crystal blue phase II," *Nature Materials* **1**(2), 111-113 (2002).
117. X. H. H. Wu, A. Yamilov, H. Noh, H. Cao, E. W. Seelig, and R. P. H. Chang, "Random lasing in closely packed resonant scatterers," *Journal of the Optical Society of America B-Optical Physics* **21**(1), 159-167 (2004).
118. A. Yamilov and H. Cao, "Highest-quality modes in disordered photonic crystals," *Physical Review A* **69**(3), R031803 (2004).
119. A. Yamilov, X. Wu, X. Liu, R. P. H. Chang, and H. Cao, "Self-optimization of optical confinement in an ultraviolet photonic crystal slab laser," *Physical Review Letters* **96**(8), 083905 (2006).
120. A. Rodriguez, M. Ibanescu, J. D. Joannopoulos, and S. G. Johnson, "Disorder-immune confinement of light in photonic-crystal cavities," *Optics Letters* **30**(23), 3192-3194 (2005).
121. Y. A. Vlasov, M. A. Kaliteevski, and V. V. Nikolaev, "Different regimes of light localization in a disordered photonic crystal," *Physical Review B* **60**(3), 1555-1562 (1999).

122. A. F. Koenderink, A. Lagendijk, and W. L. Vos, "Optical extinction due to intrinsic structural variations of photonic crystals," *Physical Review B* **72**(15), 153102 (2005).
123. All band structure calculations presented in Chapter 4 and 5 were performed by Dr. Alexey Yamilov. Calculations for the research in Chapter 6 were performed by Heeso Noh.
124. H. Cao, Y. G. Zhao, S. T. Ho, E. W. Seelig, Q. H. Wang, and R. P. H. Chang, "Random laser action in semiconductor powder," *Physical Review Letters* **82**(11), 2278-2281 (1999).
125. H. M. van Driel and W. L. Vos, "Multiple Bragg wave coupling in photonic band-gap crystals," *Physical Review B* **62**(15), 9872-9875 (2000).
126. A. Figotin and I. Vitebskiy, "Slow light in photonic crystals," <http://arxiv.org/abs/physics/0504112> (2005).
127. J. F. Galisteo-Lopez and C. Lopez, "High-energy optical response of artificial opals," *Physical Review B* **70**(3), 035108 (2004).
128. F. Garcia-Santamaria, J. F. Galisteo-Lopez, P. V. Braun, and C. Lopez, "Optical diffraction and high-energy features in three-dimensional photonic crystals," *Physical Review B* **71**(19), - (2005).
129. W. L. Vos and H. M. van Driel, "Higher order Bragg diffraction by strongly photonic fcc crystals: onset of a photonic bandgap," *Physics Letters A* **272**(1-2), 101-106 (2000).
130. B. H. Juarez, M. Ibisate, J. M. Palacios, and C. Lopez, "High-energy photonic bandgap in Sb₂S₃ inverse opals by sulfidation processing," *Advanced Materials* **15**(4), 319-323 (2003).
131. L. Bechger, P. Lodahl, and W. L. Vos, "Directional fluorescence spectra of laser dye in opal and inverse opal photonic crystals," *Journal of Physical Chemistry B* **109**(20), 9980-9988 (2005).
132. K. Postava, H. Sueki, M. Aoyama, T. Yamaguchi, C. Ino, Y. Igasaki, and M. Horie, "Spectroscopic ellipsometry of epitaxial ZnO layer on sapphire substrate," *Journal of Applied Physics* **87**(11), 7820-7824 (2000).
133. A. Blanco, H. Miguez, F. Meseguer, C. Lopez, F. Lopez-Tejeira, and J. Sanchez-Dehesa, "Photonic band gap properties of CdS-in-opal systems," *Applied Physics Letters* **78**(21), 3181-3183 (2001).
134. J. F. Galisteo-Lopez, F. Lopez-Tejeira, S. Rubio, C. Lopez, and J. Sanchez-Dehesa, "Experimental evidence of polarization dependence in the optical response of opal-based photonic crystals," *Applied Physics Letters* **82**(23), 4068-4070 (2003).

135. S. G. Romanov, T. Maka, C. M. S. Torres, M. Muller, and R. Zentel, "Emission properties of dye-polymer-opal photonic crystals," *Journal of Lightwave Technology* **17**(11), 2121-2127 (1999).
136. S. G. Romanov, T. Maka, C. M. S. Torres, M. Muller, and R. Zentel, "Emission in a SnS₂ inverted opaline photonic crystal," *Applied Physics Letters* **79**(6), 731-733 (2001).
137. H. P. Schriemer, H. M. van Driel, A. F. Koenderink, and W. L. Vos, "Modified spontaneous emission spectra of laser dye in inverse opal photonic crystals," *Physical Review A* **63**(1), 011801(011801)-011801(011804) (2001).
138. K. Yoshino, S. B. Lee, S. Tatsuhara, Y. Kawagishi, M. Ozaki, and A. A. Zakhidov, "Observation of inhibited spontaneous emission and stimulated emission of rhodamine 6G in polymer replica of synthetic opal," *Applied Physics Letters* **73**(24), 3506-3508 (1998).
139. M. Barth, A. Gruber, and F. Cichos, "Spectral and angular redistribution of photoluminescence near a photonic stop band," *Physical Review B* **72**(8), - (2005).
140. A. Blanco, C. Lopez, R. Mayoral, H. Miguez, F. Meseguer, A. Mifsud, and J. Herrero, "CdS photoluminescence inhibition by a photonic structure," *Applied Physics Letters* **73**(13), 1781-1783 (1998).
141. S. G. Romanov, T. Maka, C. M. S. Torres, M. Muller, and R. Zentel, "Suppression of spontaneous emission in incomplete opaline photonic crystal," *Journal of Applied Physics* **91**(11), 9426-9428 (2002).
142. R. C. Schroden, M. Al-Daous, and A. Stein, "Self-modification of spontaneous emission by inverse opal silica photonic crystals," *Chemistry of Materials* **13**(9), 2945-2950 (2001).
143. A. F. Koenderink and W. L. Vos, "Optical properties of real photonic crystals: anomalous diffuse transmission," *Journal of the Optical Society of America B-Optical Physics* **22**(5), 1075-1084 (2005).
144. All calculations in this chapter were performed by Heeso Noh.
145. E. Pavarini, L. C. Andreani, C. Soci, M. Galli, F. Marabelli, and D. Comoretto, "Band structure and optical properties of opal photonic crystals," *Physical Review B* **72**(4), - (2005).
146. S. G. Romanov, T. Maka, C. M. S. Torres, M. Muller, R. Zentel, D. Cassagne, J. Manzanares-Martinez, and C. Jouanin, "Diffraction of light from thin-film polymethylmethacrylate opaline photonic crystals," *Physical Review E* **63**(5), art. no.-056603 (2001).

147. S. L. Morelhao and L. H. Avanci, "Strength tuning of multiple waves in crystals," *Acta Crystallographica Section A* **57**, 192-196 (2001).
148. A. V. Baryshev, A. B. Khanikaev, H. Uchida, M. Inoue, and M. F. Limonov, "Interaction of polarized light with three-dimensional opal-based photonic crystals," *Physical Review B* **73**(3)(2006).
149. P. D. Garcia, A. Blanco, A. Shavel, N. Gaponik, A. Eychmuller, B. Rodriguez-Gonzalez, L. M. Liz-Marzan, and C. Lopez, "Quantum dot thin layers templated on ZnO inverse opals," *Advanced Materials* **18**(20), 2768-+ (2006).

Vita

Michael Scharrer was born in 1974 in Lauf a. d. Peg., Germany, and did his undergraduate studies in materials science at the Friedrich-Alexander-University Erlangen-Nuremberg. He received his Master of Science in Materials Science and Engineering from Alfred University, New York, in 2000, where he studied with Prof. Alan Meier. From 1999 until 2002 he worked as a research engineer at the Thomas Edison Technical Center, Cooper Power Systems, in Franksville, Wisconsin. In 2002 he came to Northwestern University, working under the guidance of Prof. R. P. H. Chang on fabrication and characterization of optically active ZnO photonic crystals. In early 2007 Michael will return to Germany as a postdoctoral scientist for Prof. Philip Russell at the Max Planck Research Group for Photonics and New Materials, Institute for Optics, Information, and Photonics, University of Erlangen-Nuremberg.

Publications

Michael Scharrer, Heeso No, Larry Aagesen, Hui Cao, and Robert P. H. Chang, "Angle- and polarization-resolved reflection and photoluminescence spectroscopy of ZnO photonic crystals," manuscript in preparation (2007).

Michael Scharrer, Alexey Yamilov, Xiaohua Wu, Hui Cao, and Robert P. H. Chang, "Ultraviolet Lasing with Reduced Threshold near the First Γ L-Pseudogap of ZnO Inverse Opals," submitted to Applied Physics Letters, December 2006.

Michael Scharrer, Alexey Yamilov, Xiaohua Wu, Hui Cao, and Robert P. H. Chang, "Ultraviolet lasing in high-order bands of three-dimensional ZnO photonic crystals," Applied Physics Letters **88**, 201103 (2006).

Michael Scharrer, Xiaohua Wu, Alexey Yamilov, Hui Cao, and Robert P. H. Chang, "Fabrication of inverted opal ZnO photonic crystals by atomic layer deposition," Applied Physics Letters **86**, 151113 (2005).